Supercontinuum Generation by Ghost Pulse

Dissertation

zur Erlangung des Grades eines

Doktors der Naturwissenschaften (Dr. rer. nat.)

am Fachbereich Physik

der Freien Universität Berlin

vorgelegt von

Xingwen Zhang

Berlin 2021

Erstgutachter/in: Prof. Dr. Karsten Heyne

Zweitgutachter/in: Prof. Dr. Holger Dau

Tag der Disputation: January 26, 2021

Kurzfassung

Diese Dissertation beschreibt eine neuartige Methode zur Erzeugung von negativ gechirptem Superkontinuum (SC) und beschreibt detailliert das Design, die Herstellung und die umfassende Charakterisierung der erzeugten SC. Nach der SPM-Theorie sollte ein inverser Gaußscher Puls in der Lage sein, negativ gechirpte SC zu erzeugen. In dieser Arbeit wird ein solcher inverser Gaußscher Impuls als "Ghost pulse" bezeichnet. Jedoch ist es praktisch unmöglich, einen inversen Gaußschen Puls zu erzeugen, da die Pulsintensität nicht negativ sein kann. Um eine negativ gechirpte SC zu erzeugen, besteht die erste schwierige Herausforderung daher darin, den gewünschten Ghost pulse zu erhalten. In dieser Studie wurden ein 4f-Linien-Impulsformungssystem und ein Summenfrequenzerzeugung-Setup (SFG) aufgebaut und angewendet, um einen stabilen Ghost pulse zu erzeugen. Aufgrund der Begrenzung durch die Fourier-Transformation entspricht eine schmale spektrale Bandbreite einer langen Pulsdauer. Dadurch kann das 4f-Linien-Pulsformungssystem einen Puls $E_{4f}(t)$ ($\tau_p \approx 2\,ps$) mit langer Dauer erzeugen, indem es die spektrale Bandbreite des Eingangspulses verengt. Anschließend wurde ein nichtlinearer Summenfrequenzerzeugungsprozess (SFG) zwischen diesem langen Impuls $E_{4f}(t)$ und einem Fundamentalimpuls $E(t)$ ($\tau_p \approx 200\,fs$) durchgeführt. Die Zentralenergie des Pulses $E_{4f}(t)$ war aufgrund des SFG-Prozesses verringert und so wurde ein Ghost pulse $E_{ghost}(t)$ erzeugt. Die Formung dieses Ghost pulse wurde durch ein kommerzielles Autokorrelator-Gerät und eine selbst gebaute frequenzaufgelöste optische Nachweismethode (FROG) verifiziert. Mit diesem Ghost pulse konnten in YAG- und Saphirkristallen negativ gechirptes SC erzeugt werden. Aus Kontrastgründen wurde auch ein Kontrollexperiment mit einem Fundamentalpuls ($\tau_p \approx 200\,fs$) zur Erzeugung von SC durchgeführt.

Die erzeugten SCs wurden experimentell mit Hilfe einer Vielzahl verschiedener Techniken wie Autokorrelator, FROG und nicht-kollinearer optischer parametrischer Verstärker (NOPA) charakterisiert. Die Validierung der experimentellen Ergebnisse durch diese verschiedenen Strategien erlaubt es uns, die Eigenschaften der erzeugten SC systematisch zu überprüfen. Die Ergebnisse der NOPA und des Autokorrelators zeigen, dass die durch den Ghost pulse erzeugte SC negativ gechirpt wird. Die FROG-Ergebnisse demonstrieren direkt, dass der SC alleine durch den Ghost pulse erzeugt wird und negativ gechirpt ist, während der durch Fundamentalimpulse erzeugte SC positiv gechirpt ist.

Abstract

This dissertation provides a novel method to generate negatively chirped supercontinuum (SC) and details the design, fabrication and complete characterization of the generated SC. According to the SPM theory, an inverse Gaussian pulse should be able to generate negatively chirped SC. In this thesis this kind of inverse Gaussian pulse is termed as "ghost pulse". However, in practice it is impossible to produce an inverse Gaussian pulse because the pulse intensity can not be negative. Therefore, in order to generate negatively chirped SC, the first difficult challenge is how to obtain the desired ghost pulse. In this work, a 4f-line pulse shaping system and a sum-frequency generation (SFG) setup were built and performed to produce a stable ghost pulse. Due to the Fourier transform limit, narrow spectral bandwidth corresponds to long pulse duration. Thereby, the 4f-line pulse shaping system can produce a long duration pulse $E_{4f}(t)$ ($\tau_p \approx 2\ ps$) by narrowing the spectral bandwidth of the input pulse. Afterwards, a sum-frequency generation (SFG) nonlinear process was performed between this long pulse $E_{4f}(t)$ and a fundamental pulse $E(t)$ ($\tau_p \approx 200\ fs$). The center energy of the pulse $E_{4f}(t)$ was depleted due to the SFG process and thus a ghost pulse $E_{ghost}(t)$ was obtained. The formation of this ghost pulse was verified by a commercial autocorrelator device and a home-built FROG (frequency-resolved optical gating) setup. Pumping by this ghost pulse and using YAG and sapphire crystals as the working media, we have succeeded in generating negatively chirped SC. For the sake of contrast, a control experiment using the fundamental pulse ($\tau_p \approx 200\ fs$) to generate SC was also carried out.

The generated SCs were experimentally characterized with the help of different techniques including autocorrelator, FROG and NOPA (non-collinear optical parametric amplifier). The validation of the experimental results by these different strategies allows us to check the properties of the generated SC systematically. The NOPA and autocorrelator results reveal that the SC generated by ghost pulse is negatively chirped in a round-about way. The FROG results directly prove that the SC is purely generated by ghost pulse and is clear negatively chirped, while the SC generated by fundamental pulse is positively chirped.

# Contents

Chapter 1
Introduction

Since the advent of laser, physicists are always exploring different methods to optimize laser performance for achieving different goals, such as new wavelength bands, maximum average output power, minimum output pulse length [1-4], etc. In recent years, we have seen exciting development in the generation of ultrashort laser sources and their important applications in a variety of research fields [5-7]. Now it is convenient to find many kinds of commercial laser devices which can output picosecond (ps, 10^{-12} s) pulses. Several companies can also extend the duration time of pulse into the femtosecond (fs, 10^{-15} s) time region. Some literatures have reported that they can produce pulses consisting of just several optical cycles [8-10]. Many novel instruments with extremely high temporal resolution have been invented based on ultrashort laser pulses. These exciting progresses of ultrafast pulses permit us to study and discover key processes unresolved in the past.

The great point about ultrafast laser pulses is that they have very high intensity because all the energy is compressed into an ultrashort time. The tremendous development of the ultrafast laser based on nonlinear optics is an important branch of modern optics [11]. The nonlinear optics mainly studies high intensity effects, e.g., second harmonic generation (SHG) process [12, 13] which allows to obtain output light at double frequency and half wavelength, or like optical parametric amplification (OPA) [14-16] which amplifies a signal input by a higher frequency pump input and generates an idler wave, etc.

Supercontinuum (SC) generation [17-19] is one of the most important and amazing nonlinear optical processes, a phenomenon that intense laser can dramatically broaden the input spectrum bandwidth in a transparent medium. The first study on the SC generation dates back to 1968, when Alfano and Shapiro observed the picosecond "white" continuum in the bulk of borosilicate glass [20, 21]. With the high intensity laser pulses on the order of GW/cm^2 in the sample, the spectrum of laser pulses transmitted through the sample stretched from 400 to 700 nm. Fig. 1.1 presents the wavelength range of the anti-Stokes side covering from 4000 to 5300 Å which was published by Alfano and Shapiro in 1970 [20].

Soon afterwards, Alfano and Shapiro published SC generation accompanied by the formation of thin laser radiation filaments in sodium chloride, quartz, calcite, and various types of glass [22-26]. In the years of 1970s, experimental studies in SC generation demonstrated that the SC generation can be achieved in various materials with different states and

structures, including solid-state materials [27], organic and inorganic liquids [28-30], and gas media [31, 32]. In the meantime, some studies on waveguide SC generation in silica optical fibers were also reported [33, 34]. Moreover, SC generation has been quickly used as a novel broadband light sources to equip experimental instruments for spectroscopy and time-resolved measurements [33, 35].
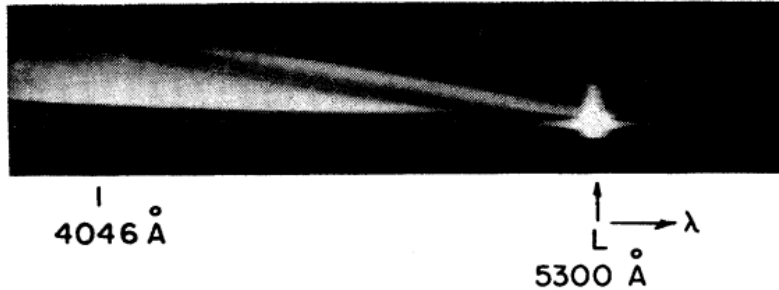

Figure 1.1: Alfano and Shapiro reported SC generation in 1970, and this figure shows the entire emission range of the anti-Stokes side from 4000 to 5300 Å [20].

In 1983, Fork and co-authors reported the first femtosecond SC generation which presented spectral broadening from deep UV to near IR when they focused ultrashort pulses of duration ~80 fs at 627 nm into an ethylene glycol jet [36]. Starting with the late 1980s, SC generation has also been employed for obtaining ultrashort laser pulses and the creation of multifrequency multiplex light sources [37]. Until today, SC generation is still an essential step in the research field of pulse compression technique and has important applications for time-resolved absorption spectroscopy to study the ultrafast processes which occur in solid state physics, biology and chemistry [38]. Furthermore, SC generation has widely potential values in some other application fields, such as optical microscopy [39, 40], attosecond science [41], frequency comb technology [42-45], etc.

SC generation is a complex physical process that intricate couplings of spatial-temporal effects are involved. SC generation in transparent bulk media can be explained in the framework of light filamentation [46-49]. In the spatial domain, several linear and nonlinear effects (diffraction, self-focusing, group velocity dispersion, self-phase modulation (SPM), and multiphoton ionization or absorption) interplay together forming a light channel which is termed as "filament". The filament propagates over much longer distances than the typical diffraction length. In time domain, the pulse experiences dramatic transformations: pulse front steepening, pulse compression or splitting, and generation of optical shocks. The coupling between these spatial and temporal effects produce a broadband coherent SC emission.
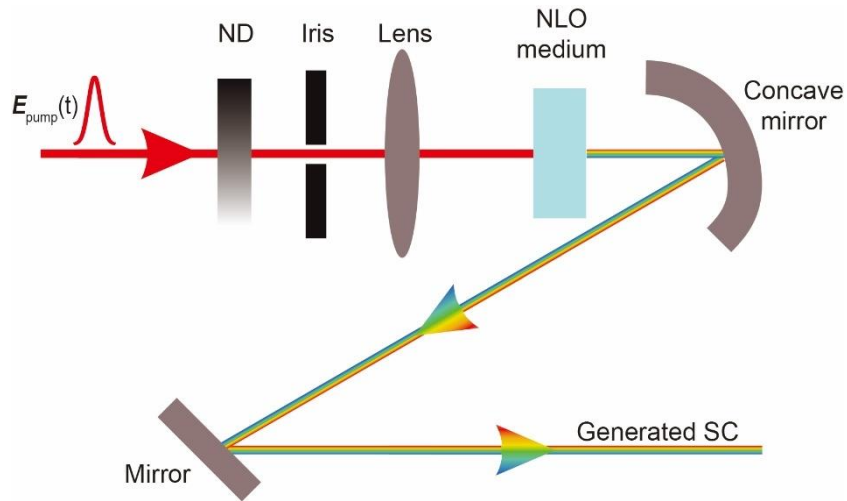
Figure 1.2: Scheme of experimental setup for SC generation. A short pulse $E_{pump}(t)$ is focused inside a proper NLO crystal to generate SC and the newly produced SC is collimated by a concave mirror. ND - neutral density filter; NLO - nonlinear optical; SC - supercontinuum.
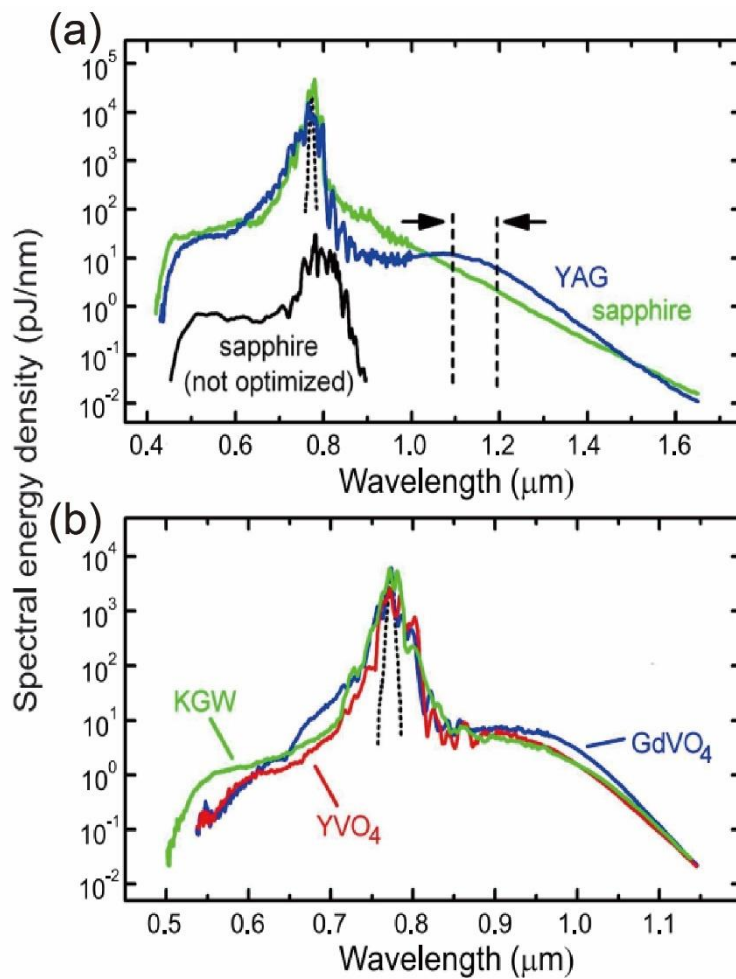

Figure 1.3: (a) Spectra of SC generated in 3 mm sapphire or 4 mm YAG crystals under different pumping conditions [50], (b) Spectra of SC generated in different crystals [51].

Although the physical mechanism of SC generation is complicate, the real setup for SC generation is simple. As shown in Fig. 1.2, the setup involves just a short pulse, a neutral density filter, an iris, a focusing lens, a suitable nonlinear material and a collimating concave mirror (or a collimating lens).

The generated SC spectra and stability are determined by many parameters, such as the wavelength and energy of the pumping pulse, the host nonlinear medium, focusing conditions, etc. In general, the SC spectra is defined by the wavelength of the pumping laser and the properties of the host media, such as transparency range, energy bandgap and nonlinear index of refraction. The SC stability is influenced by the beam size and intensity distribution of the pumping pulse, focusing conditions and medium thickness. Proper choice of these parameters is a key issue to guarantee the stable generation of our desired SC source. Fig. 1.3 presents an example that SC spectra are influenced by pumping conditions and media type.

As shown in Fig. 1.4, components at different frequencies of the generated SC are diffracted into cones under different divergence angles, forming a clear concentric rainbow-like pattern.
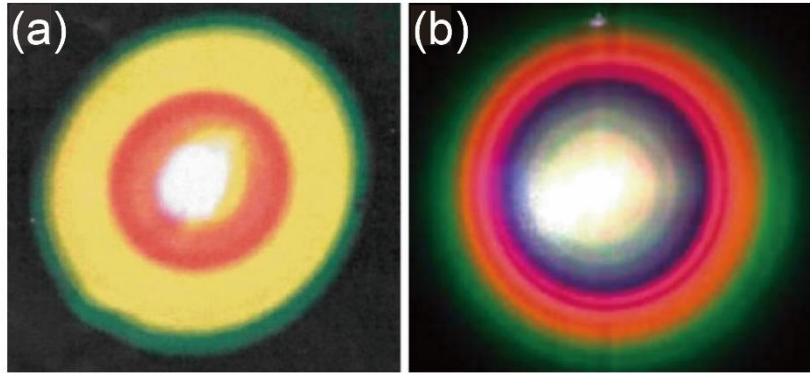
Figure 1.4: (a) Conical emission from a laser filament generated in air [52], and (b) in a ZK7 glass [53].

As mentioned above, SC generation stems from a complicate interplay process of several different optical effects. The most important effect of them is the SPM which is the dominant process to induce spectral broadening. According to the SPM theory, the pumping pulse with Gaussian shape generates a frequency modulation that blue-shifted frequency components at the pulse tail while the red-shifted frequency components at the pulse front. In thus, the generated SC features a positive chirp. In this dissertation, we will introduce a novel method to generate a negatively chirped SC. The related physical theory, design methods, and the experimental setups and results will be detailed described in the following chapters:

Chapter 2 Fundamental physics. The chapter will focus on the fundamental physics and necessary techniques relevant to SC generation. The concepts and mathematical background of ultrashort laser pulses, nonlinear

optics and optical parametric amplifier will be described. Several widely used techniques of pulse measurement such as autocorrelator, cross-correlator and FROGs will be introduced. The relevant physics of SC generation will be also presented.

Chapter 3 Negatively chirped supercontinuum generation by ghost pulse. This chapter will present the experimental setup and results of SC generation by ghost pulse. The experimental setup mainly consists of a 4f-line system, SFG setup, SC generation, and SC characterization setups (NOPA/FROG). The 4f-line is used to produce a long duration pulse. A subsequent SFG process is performed between this long pulse and a short fundamental pulse to form a desired ghost pulse. Afterwards, SC generation process is driven by the ghost pulse. The generated SC is characterized by home-built NOPA or FROG setups.

Chapter 4 Two-stage non-collinear optical parametric amplifier. This chapter will introduce the building of a two-stage NOPA setup and the compression of the NOPA output by an AOPDF (Acousto-Optic Programmable Dispersive Filter) device. The availability of this NOPA supports for gap-free tuning covering from 650 to 1000 nm. By optimizing pulse compression with different dispersion orders, we obtained a ~16 fs ultrashort pulse.

Chapter 2

Fundamental physics

Before delving into the details of the generation of negatively chirped supercontinuum (SC), it is beneficial to systematically make an overview on the relevant fundamental physics. Section 2.1 in this chapter will focus on the concepts and mathematical background of ultrafast laser pulses, which is the theoretical basis of the following content in this dissertation. Section 2.2 will briefly introduce the basic aspects of the nonlinear optics, which is necessary for understanding the SC generation theory and different pulse characterization techniques in this work. Nonlinear optics include kinds of different high-intensity effects and here we will mainly focus on the second harmonic generation (SHG) and sum frequency generation (SFG) which are the most widely used nonlinear effects. The third section 2.3 will be dedicated to the methods of ultrashort pulse characterization. This part includes a general description of the techniques of autocorrelator, cross-correlator and FROG. These techniques will be applied to characterize the generated SC in this work and more details will be described in the later chapters. The fourth section 2.4 will present a brief description of optical parametric amplifier which will also be used to characterize the generated SC. The fifth section 2.5 of this chapter will introduce the physics of SC generation which stems from a complicate interplay process of different optical effects such as Kerr effect, self-focusing, plasma defocusing, self-phase modulation, etc. SC generation by ghost pulse is the main topic of this dissertation. In the end of the chapter, the contents of this chapter will be briefly summarized.

2.1 Ultrashort laser pulse

An ultrashort laser pulse is an electromagnetic wave with duration time of the order of a picosecond (ps, 10^{-12} s) or femtosecond (fs, 10^{-15} s). It can be fully defined by the space and time dependent electric field. The propagation of ultrashort pulse and its interaction with matter are described by Maxwell's equations. In this section, some necessary physical definitions and mathematical formulas used throughout this dissertation will be discussed.
For the sake of simplicity, let us consider first the electric field is linearly polarized. Because our main concern is the temporal features of the pulse, here we can neglect its spatial dependence. The pulse electric field can be written as [54]:

$$E(t) = \frac{1}{2}\sqrt{I(t)}e^{\{i[\omega_0 t - \phi(t)]\}} + c.c. \qquad (2.1)$$

where t is time, ω_0 - the carrier angular frequency, $I(t)$ - the time-dependent intensity of the pulse, $\phi(t)$ - the phase of the pulse and "$c.c.$" - the complex conjugate. However, it is not easy to access $E(t)$ directly for ultrashort pulses. The pulse field in frequency domain is often more practical.

The Fourier transform of $E(t)$ is the pulse field in the frequency domain $\tilde{E}(\omega)$:

$$\tilde{E}(\omega) = \int_{-\infty}^{\infty} E(t)e^{-i\omega t}dt \qquad (2.2)$$

where the tilde (~) over a function indicates that it is the Fourier transform. The inverse Fourier transform of $\tilde{E}(\omega)$ is the pulse field in the time domain $E(t)$:

$$E(t) = \frac{1}{2\pi}\int_{-\infty}^{\infty} \tilde{E}(\omega)e^{i\omega t}d\omega \qquad (2.3)$$

2.1.1 Pulse duration and pulse repetition rate

Pulse duration can be understood as the pulse length in time domain. It describes the FWHM (full width at half-maximum) of the pulse power versus time. As shown in Fig. 2.1 (a), the interval time between the 50% points of its peak amplitude generally defines the pulse duration [54].
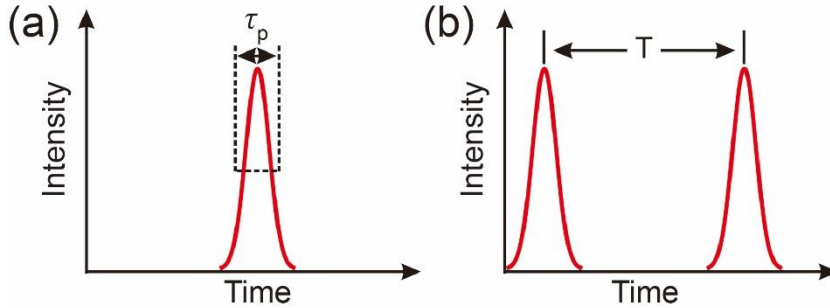
Figure 2.1: Scheme of (a) pulse duration τ_p and (b) repetition rate $\frac{1}{T}$. Pulse duration is generally defined as the pulse FWHM of the pulse power versus time. Pulse repetition rate presents the pulse number per second.

Pulse repetition rate describes the counts of pulses per second [54]. As shown in Fig. 2.1 (b), the number 1/T is the repetition rate. Different pulse generation techniques provide different repetition rates. In general, Q switching of solid-state lasers allow repetition rates from 1 Hz and 100 kHz, while mode-locked solid-state lasers provide pulse repetition rates between 50 MHz to a few gigahertz.

2.1.2 Relationship between pulse duration and spectral bandwidth

It is difficult to assert the precise pulse shape and thus here we select standard waveforms. The temporal dependence of the most cited Gaussian pulse is (with zero phase) [55, 56]:

$$E(t) = E_0 e^{-\left(\frac{t}{\tau_{HW1/e}}\right)^2} = E_0 e^{-2ln2(\frac{t}{\tau_p})^2},$$

where E_0 is amplitude, $\tau_{HW1/e}$ is the field half-width-half-maximum, and τ_p is the intensity full-width-half-maximum.

The intensity is:

$$I(t) = |E(t)|^2 = |E_0|^2 e^{-4ln2(\frac{t}{\tau_p})^2}. \quad (2.4)$$

Perform the Fourier transform on the Gaussian electric field $E(t)$:

$$E(\omega) = \mathcal{F}^{-1}[E(t)] = \int_{-\infty}^{\infty} E_0 e^{-2ln2(\frac{t}{\tau_p})^2} e^{-i\omega t} \, dt. \quad (2.5)$$

By utilizing the identity:

$$\int_{-\infty}^{\infty} e^{-ax^2} e^{-2bx} \, dx = \sqrt{\frac{\pi}{a}} e^{\frac{b^2}{a}}, \text{(a>0)},$$

the Eq. (2.5) can be expressed as:

$$E(\omega) = E_0 \sqrt{\frac{\pi}{2ln2}} \tau_p e^{-\frac{\omega^2 \tau_p^2}{8ln2}}.$$

The intensity is:

$$I(\omega) = |E(\omega)|^2 = |E_0|^2 \frac{\pi}{2ln2} \tau_p^2 e^{-\frac{\omega^2 \tau_p^2}{4ln2}}. \quad (2.6)$$

From Eqs. (2.4) and (2.6), we can derive the time bandwidth product (TBP):

$$TBP \geq \Delta f_p \tau_p = \frac{\Delta\omega_p}{2\pi} \tau_p = \frac{4ln2}{2\pi} \geq 0.441, \quad (2.7)$$

where Δf_p is the frequency FWHM of the Gaussian pulse and $\Delta\omega_p$ is the FWHM bandwidth of intensity $I(\omega)$.

According to the uncertainty principle, a Gaussian pulse with minimum TBP value 0.441 is known as Fourier transform limited pulse. The TBP depends on the pulse shape. Below table 2.1 lists the TBP values for four standard pulse shapes which are suitable for laser beams.

Table 2.1: TBP values for different standard pulse shapes [57].

Pulse shape	Intensity $I(t)$	TBP
Gaussian	$e^{-\frac{x^2}{2}}$	0.441
Hyperbolic Secant	$sech^2 x$	0.315
Lorentzian	$\dfrac{1}{1+x^2}$	0.142
Square	1 for $\lvert x \rvert \leq 1$, 0 elsewhere	0.443
Cardinal sine	$\dfrac{sin^2 x}{x^2}$	0.336
Exponential	$e^{-\frac{x}{2}}$	0.140

2.1.3 Dispersion of optical pulses

In optics, when light propagates in dispersion medium, the velocity depends on its frequency. In normal dispersion region, red-side frequencies run faster than blue-side frequencies. Therefore, after propagating a certain distance through media, the red and blue frequencies will be found in the leading part and trailing part, respectively (Fig. 2.2). It leads to the increasing of pulse duration time and decreasing of peak intensity. This is called group velocity dispersion (GVD) [58].
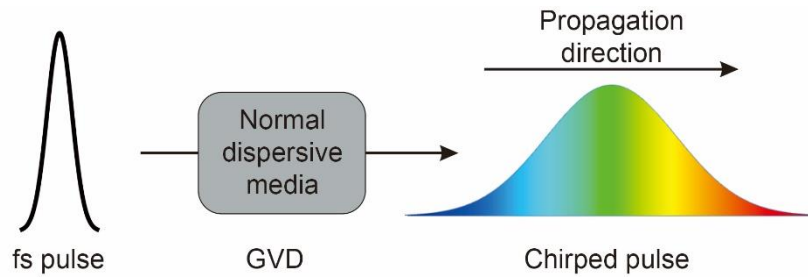
Figure 2.2: Scheme of group velocity dispersion. A short pulse passes through positive GVD media and is thus chirped to be long.

The GVD is usually defined as:

$$\text{GVD}(\omega_0) \equiv \frac{\partial}{\partial \omega}\left(\frac{1}{v_g(\omega)}\right)_{\omega=\omega_0} \equiv \left(\frac{\partial^2 k}{\partial \omega^2}\right)_{\omega=\omega_0} \equiv \frac{2}{c}\left(\frac{\partial n}{\partial \omega}\right)_{\omega=\omega_0} + \frac{\omega_0}{c}\left(\frac{\partial^2 n}{\partial \omega^2}\right)_{\omega=\omega_0}$$

(2.8)

where ω is angular frequency, ω_0 - the center angular frequency, $v_g(\omega)$ - the group velocity of ω frequency, k - the wave vector and n is the refractive index. The $v_g(\omega)$ is defined as $v_g(\omega) \equiv \partial \omega / \partial k$.

2.2 Nonlinear optics

When light with low intensity, typical non-laser sources, passes through a medium, the properties of this medium keep independent of the illumination. When laser source is used, the incident light with extremely high intensity can modify the properties of medium and thus light waves are able to interact with each other to exchange energy and momentum. On this occasion, many interesting high-intensity effects were discovered. Nonlinear optics is a modern optical branch which studies precisely these high-intensity effects [11, 59].

2.2.1 Nonlinear polarization

The wave equation is the fundamental equation of optics [54]:

$$\frac{\partial^2 E}{\partial z^2} - \frac{1}{c_0^2}\frac{\partial^2 E}{\partial t^2} = \mu_0 \frac{\partial^2 P}{\partial t^2}, \qquad (2.9)$$

where E is the real electric field, c_0 - the speed of light in vacuum, μ_0 - the magnetic permeability of free space, and P - the real induced polarization.
The induced polarization P contains linear and nonlinear optical effects. If the strength of electric field E is low, the induced polarization P is proportional to the electric field E [11, 59]:

$$P = \varepsilon_0 \chi^{(1)} E, \quad (2.10)$$

where ε_0 is the electric permittivity of free space, and $\chi^{(1)}$ is the linear susceptibility of the medium. The parameter $\chi^{(1)}$ describes the linear optics. Fig. 2.3 is a scheme of linear optics.
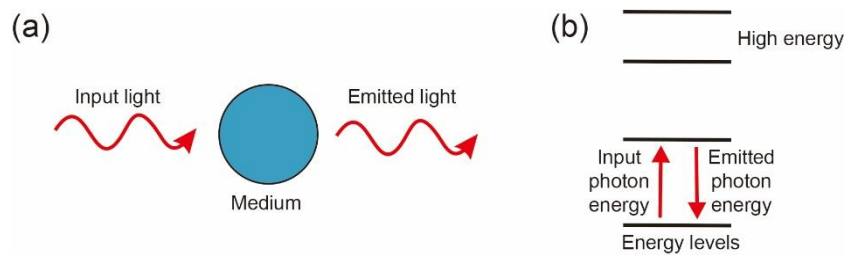
Figure 2.3: Linear optics. (a) A medium is excited by a light wave and emits a wave at the same frequency. (b) A scheme of linear optics that a medium is excited by the input photon to an excited energy level and then emits the photon at the same frequency.

If the strength of electric field E is high enough, the induced polarization P in the medium does not respond linear anymore. The higher order terms contribute to the polarization [11, 59]:

$$P = P^{(1)} + P^{(2)} + P^{(3)} + \cdots = \varepsilon_0 \chi^{(1)} E + \varepsilon_0 \chi^{(2)} E^2 + \varepsilon_0 \chi^{(3)} E^3 + \cdots, \quad (2.11)$$
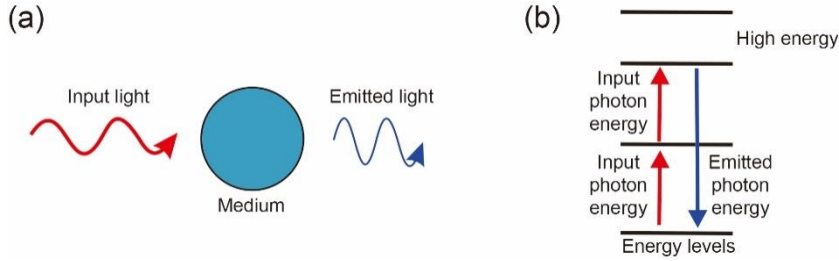
where $\chi^{(n)}$ denotes the n-th order component of electric susceptibility of the medium.

We can express the i-th component for the vector P explicitly as:

$$P_i = \varepsilon_0 \chi_{ij}^{(1)} E_j + \varepsilon_0 \chi_{ijk}^{(2)} E_j E_k + \varepsilon_0 \chi_{ijkl}^{(3)} E_j E_k E_l + \cdots, \quad (2.12)$$

where i = 1, 2, 3.

This is the foundation of nonlinear optics. Fig. 2.4 is a simple scheme of nonlinear optics.

Figure 2.4: Nonlinear optics. (a) A medium is excited by a light wave and emits a wave at new frequency. (b) A scheme of nonlinear optics that a medium is excited by the input photons to an excited energy level and then emits the photon at new frequency.

2.2.2 Second harmonic generation

In 1961, Franken et al. first observed a 347.15 nm output when they passed light from a ruby laser (λ = 694.3 nm) through a quartz crystal [60]. The output frequency is exactly doubled. This is the first time we observed second harmonic generation (SHG) phenomenon. Now SHG process has been unarguably one of the most widely used method to get up-conversion frequency light.

Mathematically, SHG effect can be derived from the second-order susceptibility $\chi^{(2)}$. Considering only the second-order term in Eq. (2.12), the resulting nonlinear polarization is expressed as:

$$P_{NL} = \varepsilon_0 \chi_{ijk}^{(2)} E_j E_k \quad (2.13)$$

Recall the electric field in Eq. (2.1):

$$E(t) = \frac{1}{2}\sqrt{I(t)}e^{i[\omega_0 t - \phi(t)]} + c.c.$$

Here we assume that the $I(t)$ and $\phi(t)$ vary slowly compared to $e^{i\omega t}$. The electric field can be rewritten as:

$$E_j(t) = E_k(t) = \mathcal{E}e^{i\omega t} + c.c. \quad (2.14)$$

where $\mathcal{E}$ is the field amplitude.

Substituting the $E_j(t)$ and $E_k(t)$ into Eq. (2.13), we can get:

$$P_{NL} = \varepsilon_0 \chi_{ijk}^{(2)} (\mathcal{E}^2 e^{i2\omega t} + \mathcal{E}^{*2} e^{-i2\omega t} + 2\mathcal{E}\mathcal{E}^*) \qquad (2.15)$$

From this equation we can find that the nonlinear polarization P_{NL} contains a component which radiates at double frequency of the input pulse. A zero-frequency term is also included in the above P_{NL} expression, so light contains a DC field. This effect is known as optical rectification which is usually very weak. In the remaining, we will ignore this optical rectification effect and just discuss the SHG effect.

For occurring nonlinear optical effects, three requirements must be met: high intensity light, conservation of momentum and conservation of energy. Fig. 2.5 is a scheme of the SHG concept. Two photons interact and are converted to a single photo at double frequency.
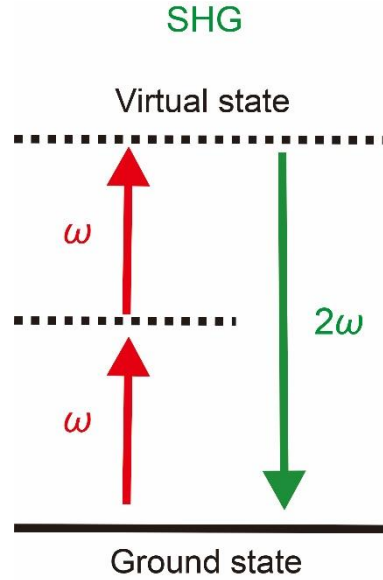
Figure 2.5: Scheme of SHG process that two photons at frequency ω are converted to a new photon at double frequency 2ω.

2.2.3 Sum frequency generation

In the SHG process mentioned above, only one input light at frequency ω is required and output light at double frequency 2ω is obtained. Sum frequency generation (SFG) is a more generally situation of SHG process [11, 61, 62]. In the SFG process, two light beams at frequency ω_1 and ω_2 are input and a new output beam at frequency ω_3 is generated.

Considering Eq. (2.14), the two input beams can be described as:

$$E_j(t) = \mathcal{E}_j e^{i\omega_1 t} + c.c.$$
$$E_k(t) = \mathcal{E}_k e^{i\omega_2 t} + c.c. \qquad (2.16)$$

The corresponding nonlinear polarization is given by:

$$P_{NL} = \varepsilon_0\chi_{ijk}^{(2)}E_jE_k = \varepsilon_0\chi_{ijk}^{(2)}(\mathcal{E}_j\mathcal{E}_k e^{i(\omega_1+\omega_2)t} + \mathcal{E}_j^*\mathcal{E}_k^* e^{-i(\omega_1+\omega_2)t} +$$

$$\mathcal{E}_j^*\mathcal{E}_k e^{i(\omega_2-\omega_1)t} + \mathcal{E}_j\mathcal{E}_k^* e^{i(\omega_1-\omega_2)t}) \qquad (2.17)$$

As shown in this expression that the nonlinear polarization P_{NL} contains components at new frequency $\omega_3 = \omega_1 + \omega_2$. This is SFG process.

SFG process also needs to meet the requirements of conservation of momentum and conservation of energy:

$$\hbar\vec{k}_3 = \hbar\vec{k}_1 + \hbar\vec{k}_2 \qquad (2.18)$$
$$\hbar\omega_3 = \hbar\omega_1 + \hbar\omega_2$$

Fig. 2.6 is a scheme of the SFG concept. Two photons at frequencies ω_1 and ω_2 are absorbed and then emit a single photo at frequency ω_3.
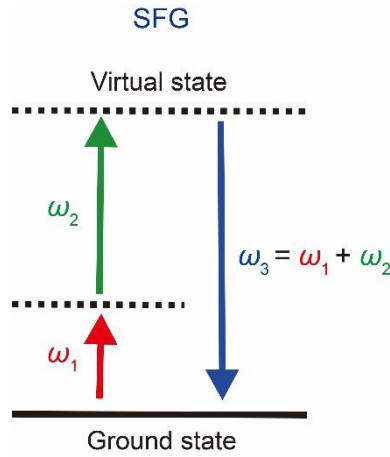
Figure 2.6: Scheme of SFG process that two photons at frequencies ω_1 and ω_2 are absorbed and a new photon at sum frequency $\omega = \omega_1 + \omega_2$ emits.

2.3 Pulse measurement techniques

In the past decades, the development of laser sources and the investigation of ultrashort pulses have made tremendous progress [63-68]. Now very short pulses with duration time only several femtoseconds (fs, 10^{-15} s) are obtained. How to characterize the pulse is as important as its generation due to the following several reasons. Firstly, if the precise information of the experimental pulse can be measured, its distortion can be known and we can try to make even shorter pulses. Secondly, many practical applications require the temporal resolution and thus we must characterize the short pulse. Thirdly, for verifying theoretical models of pulse creation, we should know the information of pulse. Moreover, many experiments study the pulse changes before and after laboratory optical system, and for this case we need to know the precise information of the pulse.

Since the response time of electronic devices is generally of the order of nanoseconds or picoseconds, it does not support the direct measurement of an ultrashort pulse in time domain. In order to measure the temporal

characteristics as short as few femtoseconds, we need an either shorter or the same duration as the pulse itself. The only solution to directly measure a femtosecond pulse in time domain, is to measure the pulse by itself. Up to now, scientists have developed a vast variety of characterization techniques for the measurement of ultrashort pulses [69, 70]. In this section, we will introduce several popular techniques such as autocorrelator [71, 72], cross-correlator [73] and FROG [74-81] (e.g., SHG FROG, XFROG, etc.).

2.3.1 Autocorrelator and cross-correlator

As discussed above, the pulse, like any light wave, can be defined by its electric field as a function of time $E(t)$. Just consider the real part of $E(t)$ and assume the pulse is linear polarized. The time-dependent component of the pulse can be expressed as:

$$E(t) = \frac{1}{2}\sqrt{I(t)}e^{i[\omega_0 t - \phi(t)]} \quad (2.19)$$

where $I(t)$ is the time-dependent intensity, ω_0 the carrier frequency and $\varphi(t)$ the time-dependent phase of the pulse.

The pulse instantaneous frequency is expressed as:

$$\omega(t) = \omega_0 - \frac{d\varphi}{dt} \quad (2.20)$$

The Fourier transform of $E(t)$ is:

$$\tilde{E}(\omega) = \sqrt{\tilde{I}(\omega - \omega_0)}e^{\tilde{\varphi}(\omega - \omega_0)}, \quad (2.21)$$

where $\tilde{E}(\omega)$ is the Fourier transform of $E(t)$, $\tilde{I}(\omega - \omega_0)$ is the intensity of spectrum and $\tilde{\varphi}(\omega - \omega_0)$ is the spectral phase.

According to Eqs. (2.19) and (2.21), we must measure the intensity and phase in time domain (or frequency domain) so that we can know the precise information of $E(t)$ (or $\tilde{E}(\omega)$).

For the measurement of pulses in frequency domain, it is convenient to use spectrometer. However, spectrometers can not measure the phase information. For the measurement of pulses in time domain, the pulse is very fast and much shorter than the time resolution of measurement devices. The most widely used method to measure ultrashort pulse is the autocorrelator proposed by Maier et al. (1966) [82]. As shown in Fig. 2.7, the test pulse passes through a Michelson interferometer which divides the pulse into two replicas with a relative time delay. These two replicas are focused into a $\chi^{(2)}$ NLO crystal with an angle. We adjust the setup so that they can temporally and spatially overlap inside the NLO crystal. The second harmonic signal generated inside the NLO crystal comes from three sources: the SHG signal from $E(t)$, the SHG signal from $E(t - \tau)$ and the SFG signal from both $E(t)$ and $E(t - \tau)$. According to the momentum conservation rule, these three second harmonic signals propagate in different directions. We can use a

spatial filter to block the two SHG signals and thus only the SFG signal can be collected by photodiode device.

The intensity of the generated SFG signal is registered as a function of the delay time. The recorded electrical signal is proportional to the integrated intensity of $E(t)$ and $E(t-\tau)$:

$$S(\tau) \propto \int |E(t)E(t-\tau)|^2 \, dt \propto \int I(t)I(t-\tau) \, dt. \quad (2.22)$$
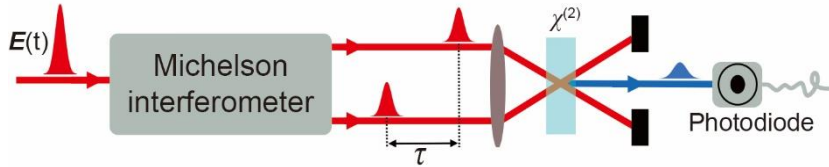
Figure 2.7: Scheme of an autocorrelator. Two replicas of the pulse are focused in an NLO crystal with an angle and a delay between them, the generated second harmonic signal is recorded by a photodiode.
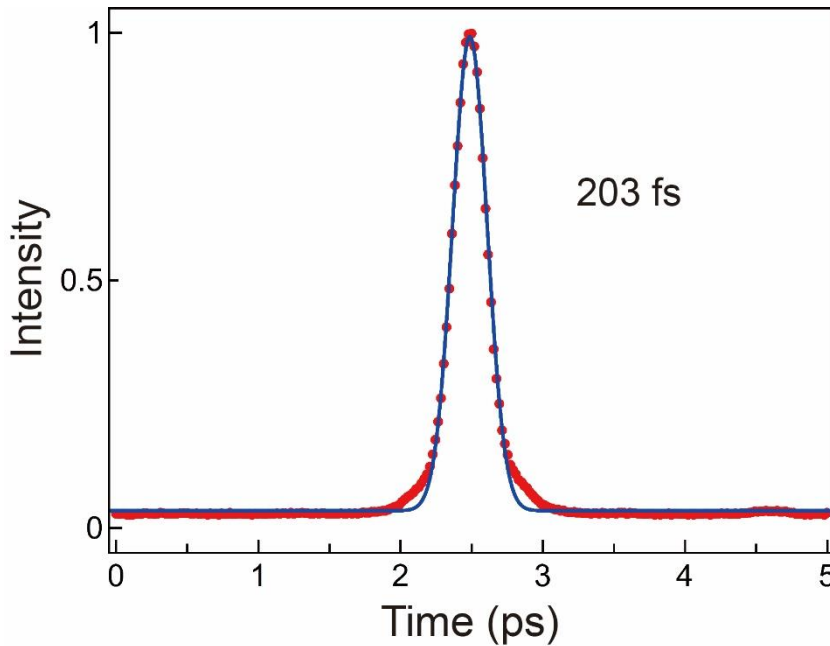
Figure 2.8: The autocorrelation function of an infrared pulse ($\lambda = 1028 \pm 4$ nm). The red dots denote the measured autocorrelation function data. The solid blue line presents the Gaussian fitting curve which shows the pulse duration is about 203 fs.

If the two replicas do not temporally overlap in the crystal, the photodiode device can not measure any electrical signal. Therefore, the autocorrelator is a "background-free" setup. Using it we can get the autocorrelation function of the test pulse and know the duration time of the test pulse. Fig. 2.8 is an example of autocorrelation function of an infrared pulse ($\lambda = 1028 \pm 4$ nm) which shows the duration time is about 203 fs. However, autocorrelation

function can not provide enough information on the pulse itself. For example, two different pulses with different profile in time domain maybe gives the same autocorrelation function and the autocorrelation function is always symmetric in time. Moreover, the information below envelope can not be measured by autocorrelator. In addition, we can not know the test pulse is chirped or Fourier transform limited.

The autocorrelator device works well for simple pulses. However, it can not measure complex pulses. For this case, we can use cross-correlation method [73]. As shown in Fig. 2.9, the cross-correlation setup is nearly same as the correlator. The only difference between them is that one replica is replaced by a known reference short pulse $E_{ref}(t)$.

The recorded electrical signal is proportional to the integrated intensity of $E_{ref}(t)$ and $E(t-\tau)$:

$$S(\tau) \propto \int \left| E_{ref}(t)E(t-\tau) \right|^2 dt \propto \int I_{ref}(t)I(t-\tau)\, dt. \quad (2.23)$$
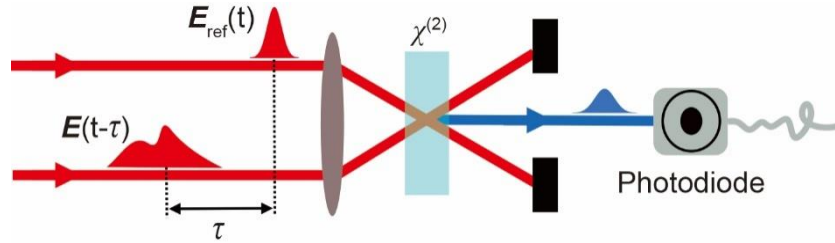
Figure 2.9 Scheme of a cross-correlator. The test pulse and the short reference pulse are focused in an NLO crystal with an angle and a variable delay between them, the generated sum-frequency signal is recorded by photodiode as a function of the delay between them.

2.3.2 Frequency-resolved optical gating technique

Autocorrelator is a measurement technique for ultrashort pulse which is operated purely in time domain. It just gives an estimate of the intensity or the pulse duration of wave envelope and does not provide a fully reconstruction of the measured electric field $E(t)$. Therefore, it is not a complete characterization method.

In order to achieve a fully reconstruction of the measured electric field $E(t)$, we need to consider a new approach which can measure the light pulse in time-frequency domain. Frequency-resolved optical gating (FROG) technique is one of the oldest and most used methods for self-referenced characterization of ultrashort pulse [74-81]. Fig. 2.10 shows the idea of FROG that uses a gate pulse to scan the test pulse in time domain and recorded the spectrum changes. FROG gives a two-dimensional signal of spectrum intensity in time and frequency domains:

$$S(\tau, \omega) \propto \left| \int E(t)G(t-\tau)e^{i\omega t}dt \right|^2, \quad (2.24)$$

where $G(t)$ is the gate pulse.
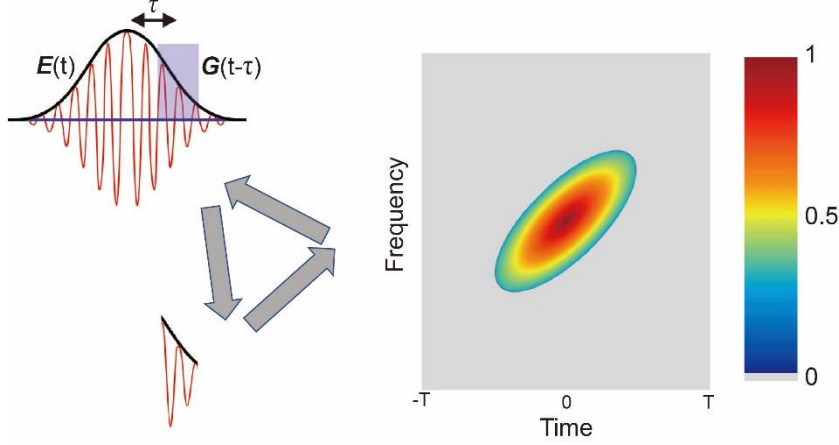
Figure 2.10: Principle of FROG setup. The test pulse $E(t)$ is temporally gated by a much shorter pulse $G(t-\tau)$. The spectrum of this gated pulse is recorded in variable delay time τ.

As summarized in Fig. 2.11, FROG setup can be performed by different optical geometries, such as XFROG [76, 80], second harmonic generation FROG (SHG-FROG) [83-89], self-diffraction FROG (SD-FROG) [75, 79] and polarization gate FROG (PG-FROG) [78].

XFROG setup uses one reference pulse to scan the test pulse. XFROG is very suitable for the measurement of shaped pulses. It has all the advantages of cross-correlation. The collected signal is expressed as:

$$S_{FROG}^{X}(\tau, \omega) \propto \left| \int E(t-\tau)E_{ref}(t) \, e^{i\omega t}dt \right|^2, \quad (2.25)$$

SHG-FROG uses second-order nonlinearity, while PG and SD FROGs uses third-order nonlinearities. Thusly, SHG FROG has high sensitivity. SHG-FROG is the most popular used FROG implementation. The signal is given as:

$$S_{FROG}^{SHG}(\tau, \omega) \propto \left| \int E(t)E(t-\tau) \, e^{i\omega t}dt \right|^2. \quad (2.26)$$

In SD-FROG, the beams induce a grating effect in medium which will diffract each beam into different directions. Measuring one of the diffractions, we can get:

$$S_{FROG}^{SD}(\tau, \omega) \propto \left| \int E(t)^2 E(t-\tau)^* \, e^{-i\omega t}dt \right|^2. \quad (2.27)$$

In PG-FROG, two beams are spatially overlapped in a $\chi^{(3)}$ medium. The gate pulse induces Kerr effect which leads to birefringence. For this case, the $\chi^{(3)}$ medium works like a wave plate. Measuring the light transmission, we can get:

$$S_{FROG}^{PG}(\tau, \omega) \propto \left| \int E(t)|E(t-\tau)|^2 \, e^{-i\omega t}dt \right|^2. \quad (2.28)$$
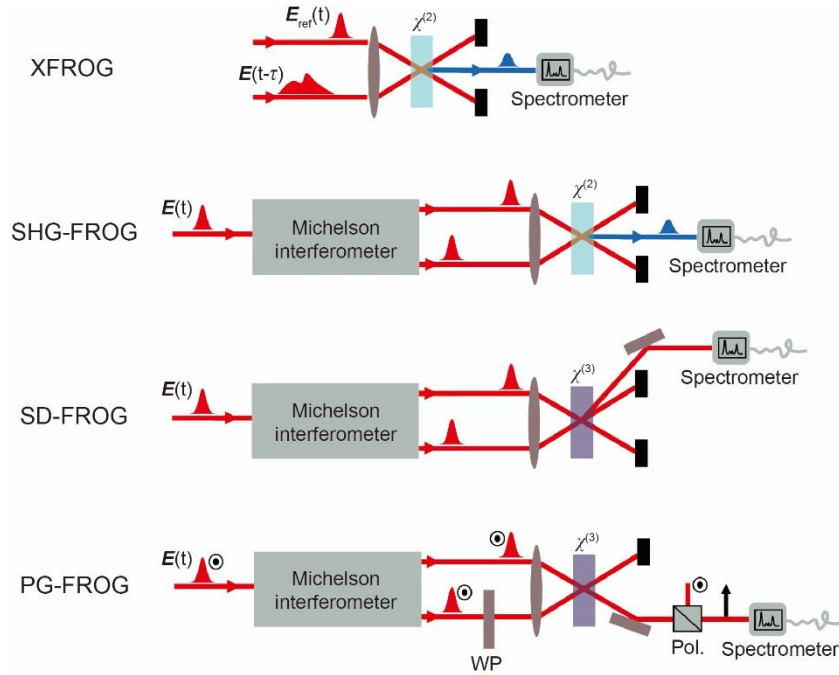
Figure 2.11: Scheme of different optical geometries for performing FROG measurement. (a) cross-correlation FROG, (b) second harmonic generation FROG (SHG-FROG), (c) self-diffraction FROG (SD-FROG) and (d) polarization gating FROG (PG-FROG). $\chi^{(2)}$ and $\chi^{(3)}$ are nonlinear susceptibilities, WP - the waveplate, and Pol. - the polarizer.

Theoretically, we can extract the amplitude and the phase information of the test pulse from the FROG 2D signal data. In fact, we can do it indeed, but it is not simple. This refers to a well-known 2D phase retrieval problem.

Up to now, several published algorithms [78, 79, 85, 90, 91] for 2D phase retrieval problem of FROG technique have been developed. Here we introduce a method which is called generalized projections [91, 92].

The purpose of algorithm is to find $E(t)$ or the electric field of signal $E_{sig}(t,\tau)$. There are two constraints:

$$S_{FROG}(\tau,\omega) \propto \left| \int E_{sig}(t,\tau) e^{-i\omega t} dt \right|^2, \quad (2.29)$$

$$\text{and } E_{sig}(t,\tau) \propto \begin{cases} E(t)|E(t-\tau)|^2 & \text{for PG FROG} \\ E(t)^2 E^*(t-\tau) & \text{for SD FROG} \\ E(t)E(t-\tau) & \text{for SHG FROG} \end{cases} \quad (2.30)$$

We start with an initial guess field $E_{sig}(t,\tau)$. Then make a projection onto the other constraint. Repeat this iteration and move the $E_{sig}(t,\tau)$ close to the right solution step by step.

2.4 Optical parametric amplifier

Optical parametric amplifier (OPA) exploiting second-order nonlinearity, represents an easy way to transfer energy from a high intensity pump pulse at a fixed frequency to weak signal/idler pulses at variable frequencies. In thus OPA provides a tunable laser source over a broad frequency range [93-100]. Non-collinear OPA can act as broadband amplifiers under suitable conditions and can thus shorten the achievable pulse duration to generate tunable ultrashort laser pulses. Due to these unique advantages, OPAs are nowadays widely used by not only physicists but also chemists and biologists.

2.4.1 Phase matching

The process of OPA requires a proper nonlinear optical (NLO) crystal. As shown in Fig. 2.12, the input beams include a pump beam and a signal beam. The pump has high frequency ω_3 and high intensity, while the signal beam has lower frequency ω_1 and lower intensity. In the NLO crystal, the pump beam transfers energy to the signal beam which is thus amplified. Simultaneously, a third new beam at frequency ω_2 is produced and we call this new beam as idler.
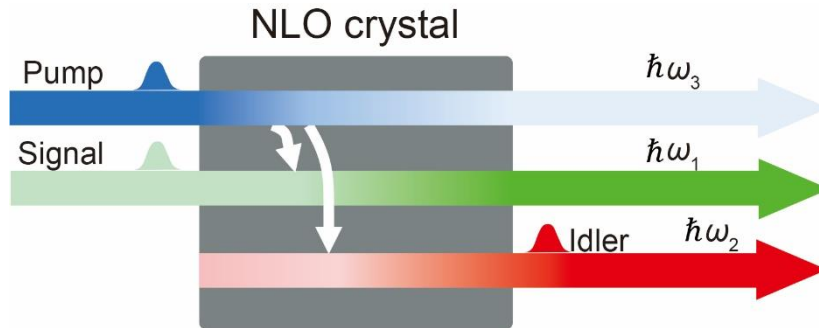
Figure 2.12: A simple model of optical parametric amplification. The energy flows from a high intensity pump beam ω_3 to a weak intensity signal beam ω_1 and a new generated idler beam ω_2.

The parameter $\Delta k = k_3 - k_2 - k_1$ determines the energy flow among the pump, signal and idler beams, where k_i (i = 1, 2, 3) are the wave-vectors of beams ω_i (i = 1, 2, 3). Thusly, for achieving maximum gain of OPA process, the phase matching condition should be satisfied that:
$$\Delta k = k_3 - k_2 - k_1 = 0. \quad (2.31)$$
Therefore, the beams pump, signal and idler fulfill the momentum conservation and the energy conservation relations:
$$\begin{aligned} \hbar k_3 &= \hbar k_1 + \hbar k_2 \\ \hbar \omega_3 &= \hbar \omega_1 + \hbar \omega_2 \end{aligned}. \quad (2.32)$$

As demonstrated in Fig. 2.13, OPA process can be briefly explained as follows: medium absorbs a photon at frequency ω_3 to get virtual level, and then a photon at frequency ω_1 stimulates the medium to emit two photons at frequencies ω_1 and ω_2. The beam ω_2 will also interact with the pump ω_3 which will contribute to the signal ω_1 amplification. Therefore, the OPA process is a positive feedback cycle and gives rise to the exponential parametric gain.
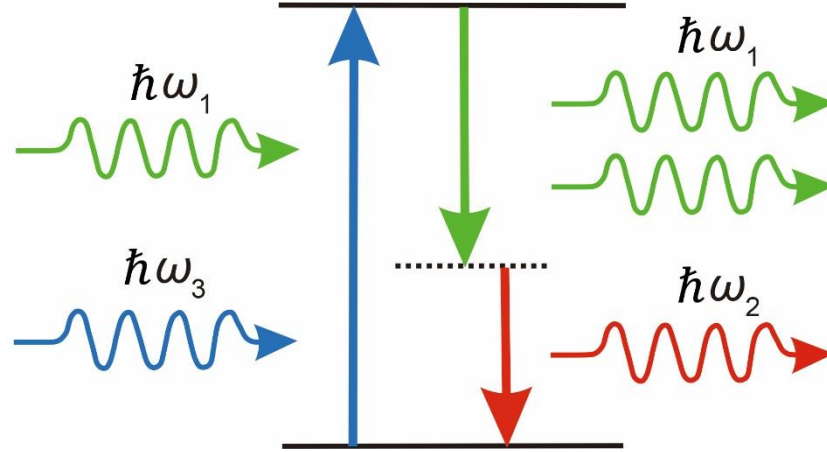
Figure 2.13: Simple model of optical parametric amplification. A photon at high frequency ω_3 (pump) is absorbed by medium, and then a photon at frequency ω_1 (signal) stimulates the medium to emit two photons at frequencies ω_1 and ω_2 (idler).

Because of $k = \omega n / c_0$ the phase matching condition can be rewritten as:

$$n_3\omega_3 - n_2\omega_2 - n_1\omega_1 = 0, \quad (2.33)$$
$$\Rightarrow \omega_3 n_3 = \omega_1 n_1 + (\omega_3 - \omega_1)n_2,$$
$$\Rightarrow \omega_3(n_3 - n_2) = \omega_1(n_1 - n_2). \quad (2.34)$$

Consider case $\omega_1 < \omega_2 < \omega_3$. In an isotropic medium with positive dispersion ($\partial n / \partial \omega > 0$) the refractive indexes have relation $n_1 < n_2 < n_3$. Eq. (2.34) has no solution because of $n_3 - n_2 > 0$ and $n_1 - n_2 < 0$. Considering the negative dispersion case $n_3 < n_2 < n_1$, we still can not find solutions for Eq. (2.34). This means that using isotropic media it is impossible to achieve the phase matching condition.

For solving this problem, we can use birefringent crystals because there are two frequency dependent refractive indexes in uniaxial crystals. Let pump, signal and idler beams propagate with different polarizations to achieve various interaction schemes. As shown in Fig. 2.14, on the plane σ the cross angle between wave-vector $\boldsymbol{k}$ and optical axis is θ. We define two normal directions E_o and E_e as ordinary (o) and extraordinary (e). The beam with ordinary polarization propagates with refractive index n_o, while the beam with extraordinary polarization propagates with variable refractive index

$n_e(\theta)$ from n_o to n_e. The uniaxial crystal can be positive $(n_o < n_e)$ or negative $(n_o > n_e)$. According to the ellipsoid equation, the $n_e(\theta)$ can be calculated by:

$$\frac{1}{n_e(\theta)^2} = \frac{cos^2\theta}{n_o^2} + \frac{sin^2\theta}{n_e^2}. \quad (2.35)$$

When we find a suitable angle θ, the refractive index $n_e(\theta)$ will be proper for fulfilling the phase matching condition. This angle θ is called phase matching angle and generally indicated with θ_m.
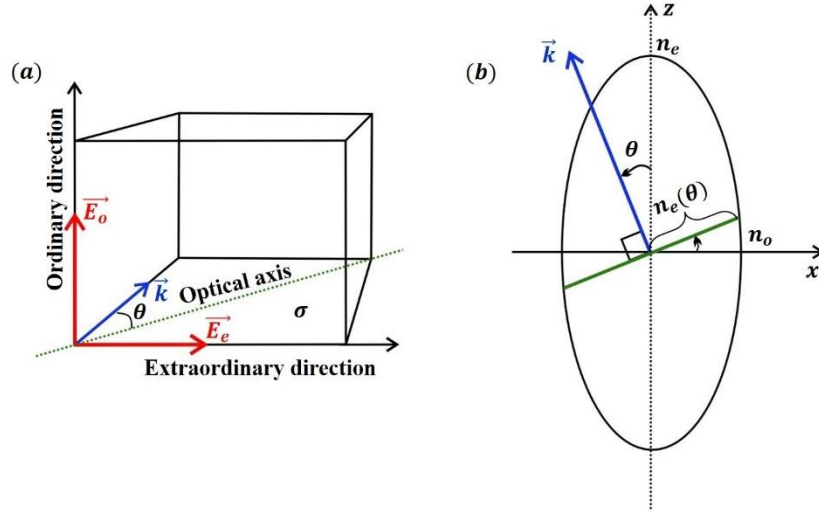
Figure 2.14: (a) Scheme of the ordinary and extraordinary directions in a birefringent crystal. (b) Scheme of the index ellipsoid: for a positive uniaxial crystal, choosing the optic axis to be in the z direction, and $n_x = n_y = n_o$ and $n_z = n_e$.

Table 2.2 summarizes all polarization configurations in second order processes.

For type 0, the pump, signal and idler beams feature the same polarizations: (ooo) or (eee).

For type I, the signal and idler beam feature the same polarization, while the pump polarization is different: (ooe) or (eeo).

For type II, the signal and idler feature cross-polarizations and thus we get: (eoe), (eoo), (oee) and (oeo).

Noticeably, not all cases listed in table 2.2 can meet the phase matching condition. For example, BBO crystal is negative uniaxial crystal $(n_e < n_o)$, and phase matching will never be met if ω_3 is extraordinary.

Table 2.2: Summary of polarization configurations of second order nonlinear
optical processes.

Type	ω_3 extraordinary	ω_3 ordinary
Type 0	eee	ooo
Type I	ooe	eeo
Type II	eoe	eoo
	oee	oeo

2.4.2 Non-collinear optical parametric amplifier

Considering the case of non-collinear parametric amplifier, the phase matching condition should be described in vectorial equation:

$$\Delta \vec{k} = \vec{k}_3 - \vec{k}_2 - \vec{k}_1 = 0. \quad (2.36)$$

Fig. 2.15 shows the situation when phase matching is fulfilled.
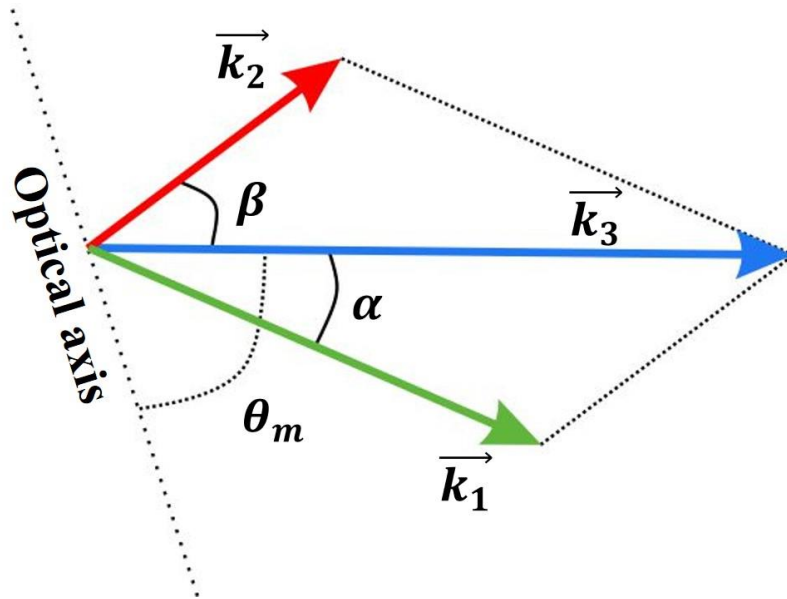
Figure 2.15: Non-collinear phase matching configurations. The phase matching condition can be fulfilled when pump beam $\vec{k}_3$, signal beam $\vec{k}_1$ and idler beam $\vec{k}_2$ propagate in different directions.

α is the angle between pump and signal, while β is the angle between pump and idler. Clearly, the vectorial $\vec{k}$ parameter allowing a cross angle between pump and signal beams helps for more flexible optical geometry to meet the phase matching condition. This non-collinear configuration supports

exact signal-idler temporal overlap and a broadband amplification. Fig. 2.16 presents the relations for different phase matching angles and signal wavelengths for NOPA in type I BBO crystal, pumped by the second harmonic frequency of an Yb-doped laser.
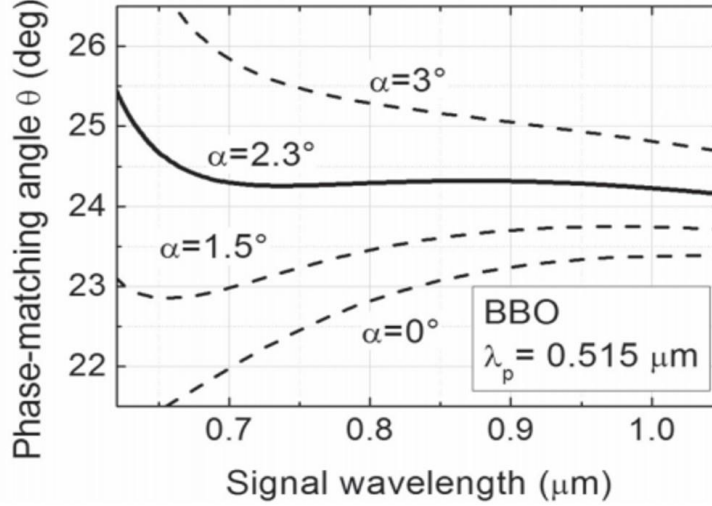
Figure 2.16: Scheme of phase matching angles and signal wavelengths for NOPA based on type I BBO crystal and pumped by 515 nm wavelength. α is the cross angle between signal and pump beams inside the BBO crystal. Solid line is the case of the broadest amplification bandwidth [101].

2.5 Supercontinuum generation

SC generation is an intricate interplay of various effects [46-49] such as self-focusing, plasma defocusing and self-phase modulation, etc.

2.5.1 Kerr effect

Kerr effect is a 3rd order nonlinear optical effect which can be understood as modifying the refractive index [102, 103]. As shown in Eq. (2.11), the induced polarization P contains linear and nonlinear optical terms. For medium with centrosymmetric crystal structure, the even order terms of Eq. (2.11) are vanished, and thus only odd order terms contribute to the induced polarization P. Because the higher order susceptibilities of medium have relationship $\chi^{(n)}/\chi^{(n+1)} \approx 10^{12}$, we can thereby neglect these higher order terms. Hence, we just need to consider the first $\chi^{(1)}$ and third $\chi^{(3)}$ terms. The induced polarization P is given as:

$$P = P^{(1)} + P^{(3)}. \quad (2.37)$$

The electric field is described as:

$$E = E_{\omega} cos\,(\omega t). \quad (2.38)$$

Thusly, the polarization P can be expressed as:

$$P = \varepsilon_0 \left(\chi^{(1)} + \frac{3}{4}\chi^{(3)}|E_\omega|^2 \right) E_\omega \cos(\omega t). \quad (2.39)$$

Observing this Eq. (2.39), it looks like we can rewrite the χ into two components, a linear susceptibility χ_L and an additional nonlinear term χ_{NL}:

$$\chi = \chi_L + \chi_{NL} = \chi^{(1)} + \frac{3\chi^{(3)}}{4}|E_\omega|^2. \quad (2.40)$$

In an isotropic material, $\chi^{(1)}$ and refractive index n_0 of material follow this relationship:

$$n_0 = \sqrt{1 + \chi^{(1)}} = \sqrt{1 + \chi_L}. \quad (2.41)$$

Now refractive index n can be described as:

$$n = \sqrt{1 + \chi} = \sqrt{1 + \chi_L + \chi_{NL}} \simeq n_0(1 + \frac{1}{2n_0{}^2}\chi_{NL}). \quad (2.42)$$

Using Taylor expansion since $\chi_{NL} \ll n_0{}^2$, we can get an intensity dependent refractive index:

$$n = n_0 + \frac{3\chi^{(3)}}{8n_0}|E_\omega|^2 = n_0 + n_2 I, \quad (2.43)$$

where n_2 is the 2nd order nonlinear refractive index, and I is the light intensity. From this equation, we can know that the refractive index change is $n_2 I$ which is proportional to the light intensity. As discussed above, the 3rd order nonlinear optics will contribute to the intensity-dependent refractive index. This effect is called as Kerr effect.

2.5.2 Self-focusing
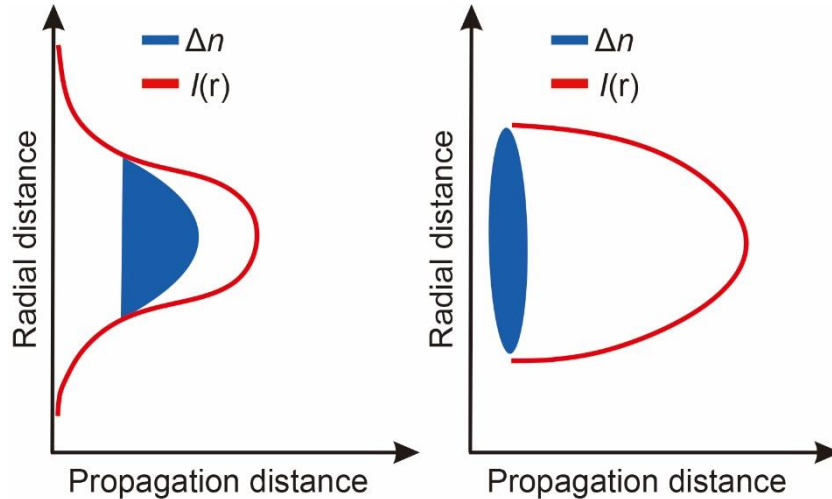
Figure 2.17: Scheme of self-focusing effect. The refractive index of medium is modified by the intensity of the laser and works like a focusing lens.

The local intensity of a beam is high at center and low at edges. According

to Eq. (2.43), we know that the change of refractive index is in direct proportional to the local intensity. Therefore, medium works like a lens, which can self-focus the incident beam. This nonlinear effect is called "self-focusing" which is a natural phenomenon resulted from Kerr effect [104]. Fig. 2.17 is a schematic diagram of self-focusing.

Self-focusing effect is determined by the input beam's power and occurs only if the beam power is high enough reaching the critical power [104-107]. J.H. Marburger et al. calculated the critical power P_{cr} for a standard Gaussian beam [104, 107]:

$$P_{cr} = \frac{3.72\lambda_0^2}{8\pi n_0 n_2}, \quad (2.44)$$

where λ_0 is the laser central wavelength.

Eq. (2.44) is valid for Gaussian beam shape. When the coefficient is equal to 3.72 [105], diffraction and self-focusing effects are balanced. If the beams feature other shapes, the coefficient 3.72 should be replaced by other values. It should be noted that the critical power given by Eq. (2.44) is proper for both ultrashort pulses and continuous wave lasers. However, for ultrashort pulses, the peak power is very high and thus we should consider many other optical effects such as group velocity dispersion, plasma defocusing and multiphoton absorption. In this case, self-focusing process will be very complex.

If input beam power is higher than P_{cr}, the collimated Gaussian beam will self-focus at a distance [104]:

$$z_{sf} = \frac{0.367 z_R}{\sqrt{[(\frac{P}{P_{cr}})^{\frac{1}{2}} - 0.852]^2 - 0.0219}}, \quad (2.45)$$

which is called the nonlinear focus. Here z_R is the diffraction length. This equation is derived for the continuous wave laser beam, but it also gives an accurate approximation in the case of ultrafast laser pulses as well.

2.5.3 Plasma defocusing

When the intensity of laser pulse is high enough, it will ionize the medium and generate plasma. The generation of plasma can cause local reduction in the refraction index. This effect is called "plasma defocusing" and the refraction index is expressed as [108]:

$$n \simeq n_0 - \frac{\rho(r,t)}{2\rho_c}, \quad (2.46)$$

where $\rho(r,t)$ is the density of free electrons and ρ_c is the critical plasma density. The parameter ρ_c is defined as

$$\rho_c \equiv \epsilon_0 m_e \omega_0^2 / e^2, \quad (2.47)$$

where ϵ_0 is the permittivity of vacuum, m_e - the electron mass and e - the electron charge.

The characteristic length L_{PL} for plasma defocusing is:

$$L_{PL} = \frac{2n_0\rho_c}{k_0\rho_{at}}, \quad (2.48)$$

where ρ_{at} is the neutral atom density.

Plasma defocusing effect works like a divergent lens. This is schematically shown in Fig. 2.18.
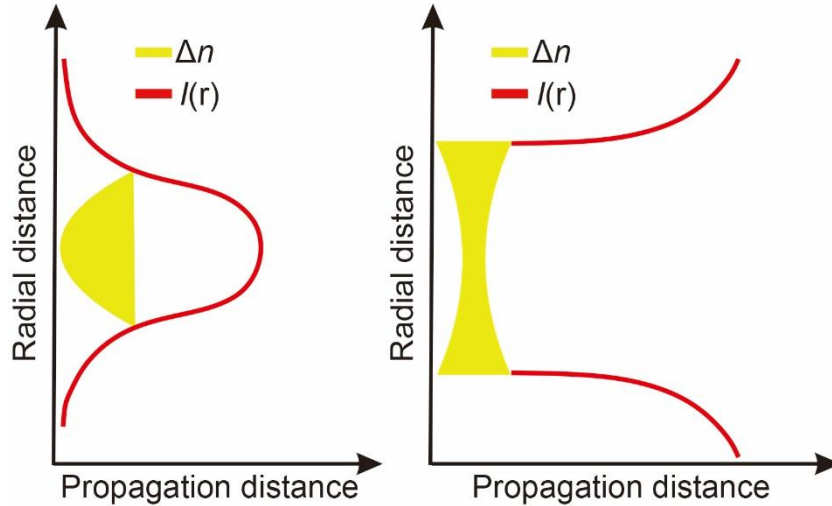
Figure 2.18: Scheme of plasma defocusing effect. The existence of plasma decreases the local refraction index of medium and thus causes beam defocusing.

2.5.4 Femtosecond filamentation

It has long been believed that, for intense ultrashort laser pulses, it is very difficult to propagate in air for long distance due to many effects. According to theoretical calculation, a pulse with duration time 30 fs and beam waist 5 mm will be reduced by a factor of $\sim 5\times10^3$ after propagating 1 km distance in air because of the influence of group velocity dispersion (factor of 50) and beam diffraction (factor of 100) [109].

However, many experiments show opposite results. In 1995, Braun et al. observed that a hard-coated mirror can not be burned by laser at the position of laser output, but if they place the same mirror 10 m far away from the laser output, the same mirror will be burned [110]. Subsequently, researchers explained that self-focusing nonlinear effect should be responsible for this phenomenon [111-117]. Self-focusing effect of a beam can form a dynamic structure which is called filamentation. This structure has an intense core and a small beam size, and can propagate longer than the diffraction length. Self-focusing and plasma defocusing affect the filament together, as shown in Fig. 2.19.
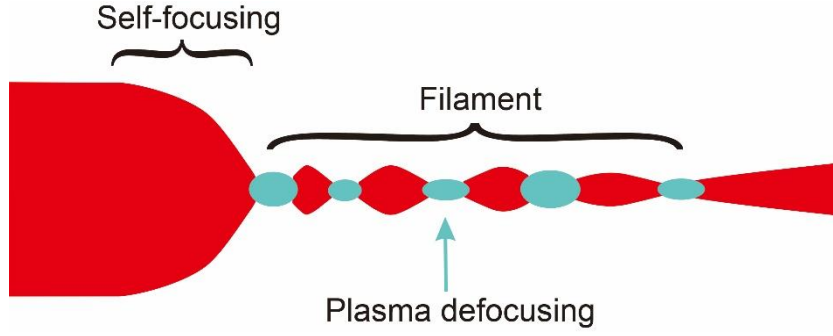
Figure 2.19: Scheme of filament. The formation of filament is a result of complicate interplay between diffraction, self-focusing, plasma defocusing, etc.

2.5.5 Self-phase modulation

Self-phase modulation (SPM) is a dominant process to generate new frequencies in the spectral range of the pumping laser pulse [118-124]. Following is a simple mathematical description for SPM theory.

The incident beam pulse propagating in z direction is:

$$E_{in}(z_0, t) = E_0(z, t)e^{i(knz-\omega_0 t)} + c.c. = E_0(z, t)e^{i\phi_0} + c.c., \quad (2.49)$$

where ω_0 is the carrier frequency, z the propagation distance and $k = \frac{\lambda}{2\pi}$ the wave number.

In the medium of length L, the phase of incident beam experiences an intensity dependent shift.

$$E_{out}(L, t) = E_0(L, t)e^{i(kn_0 L + kn_2 I(t)L - \omega_0 t)} = E_0(L, t)e^{i(\phi_{NL}(L,t) + \phi_0)}. \quad (3.16)$$

Time dependent phase $\phi_{NL}(L, t)$ comes from the time dependent intensity $I(t)$.

Nonlinear phase change of the pulse is:

$$\phi_{NL}(t) = -\frac{\omega_0}{c} n_2 I(t) z. \quad (2.50)$$

This phase change introduces a frequency change:

$$\delta\omega(t) = \frac{d}{dt} \phi_{NL}(t). \quad (2.51)$$

We can know the time-varying instantaneous frequency is:

$$\omega(t) = \omega_0 + \delta\omega(t). \quad (2.52)$$

This equation shows the spectral broadening of the incident pulse.

Substituting Eqs. (2.50) and (2.51) into Eq. (2.52), the instantaneous frequency $\omega(t)$ is given by:

$$\omega(t) = \omega_0 + \Delta\omega = \omega_0 - n_2 \frac{\omega_0}{c} z \frac{dI(t)}{dt}, \quad (2.53)$$

where ω_0 is the carrier frequency, $\Delta\omega$ - the frequency changes, n_2 - the 2nd order nonlinear refractive index, c - the speed of light, z - the propagation distance and I(t) is the light intensity.

The first term ω_0 in Eq. (2.53) is a constant which is determined by the frequency of pumping laser. The second term $\Delta\omega$ is responsible to the spectral broadening and only this term determines whether the instantaneous frequency $\omega(t)$ shows blue-shifting or red-shifting. More specifically, it can only be controlled by $\frac{dI(t)}{dt}$ because the other parameter $n_2 \frac{\omega_0}{c} z$ is positive. We first consider the general case where SC generation is performed using conventional Gaussian shaped pumping pulse, as shown in Fig. 2.20(a). The $\frac{dI(t)}{dt}$ value features positive sign (+) during the front half time of the Gaussian pulse, while the latter half part of the pulse results in minus (-) $\frac{dI(t)}{dt}$ value. Thus, the instantaneous frequency $\omega(t)$ caused by SPM effect features a negative frequency shift at the leading front of the pulse and a positive frequency shift at the trailing front of the pulse, as depicted in Fig. 2.20(c). It means the SC generated by a Gaussian pulse is positively chirped.

Now assume a case that we can obtain an inverse Gaussian pulse (see Fig. 2.20(b)) and use it to perform SC generation. We call this pulse a ghost pulse since negative intensities are not possible. A more formal definition is that ghost pulse is a short laser pulse (as normally defined), but with negative intensity in a quasi constant intensity field. Ideally, the intensity of the constant field is constant forever. Thus the (negative) intensity of the ghost pulse is limited by the intensity of the constant field. In reality, the constant field is to a very good approximation constant on the time-scale of the ghost pulse.

According to Eq. (2.53), this ghost pulse shown in Fig. 2.20(b) should give rise to opposite $\frac{dI(t)}{dt}$ comparing with the case caused by Gaussian pulse. Namely, the leading part of this ghost pulse will generate blue-shifted new frequency components while the trailing part will produce red-shifted frequency components, as depicted in Fig. 2.20(d). Therefore, using such kind of ghost driving pulse (Fig. 2.20(b)) it should be able to generate negatively chirped SC.

However, it is impossible to obtain a ghost pulse practically. An achievable solution is that on top of a rather flat intensity level a ghost pulse describes the sudden intensity loss, as shown in Fig. 2.20(e). The intensity deduction in this proposed approach can be achieved by different nonlinear effects, such as Kerr effect, SFG effect, etc.
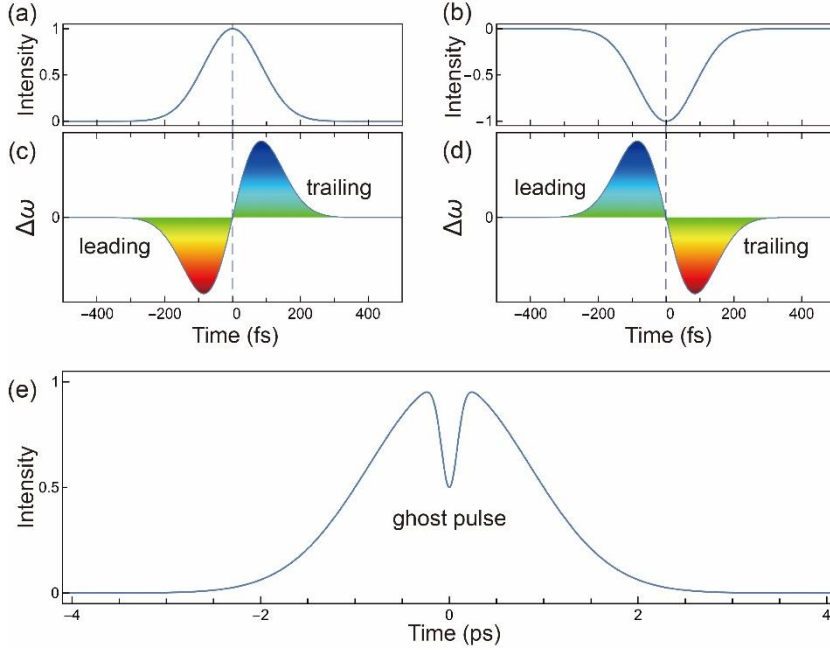
Figure 2.20: Intensity profiles of different pumping pulses and the corresponding SC generations. (a) Intensity profiles of a Gaussian pulse with pulse duration τ_p = 200 fs. (b) Intensity profiles of an assumed inverse Gaussian pulse (ghost pulse) with pulse duration τ_p = 200 fs. (c) The changes of instantaneous frequency produced by the Gaussian pulse shown in (a). (d) The changes of instantaneous frequency produced by inverse Gaussian pulse. (e) Simulated curve of a long Gaussian pulse (τ_p = 2 ps) with a centered short inverse Gaussian pulse (ghost pulse) (τ_p = 200 fs) at depth 50%.

The spectrum of the output pulse can be described as:

$$S(\omega) = |E_{out}(t)|^2 = \left| \int_{-\infty}^{\infty} E_0(t) e^{-i\omega_0 t - i\phi_{NL}(z,t)} e^{i\omega t} dt \right|^2. \quad (2.54)$$

The symmetric intensity profile leads to symmetric phase change $\Delta\phi$ and thus the spectrum has quasi-periodic oscillations. Newly generated waves can interfere. For example, two new waves have same frequencies but different phases; when $\Delta\phi_{12} = 2\pi$, they can interfere constructively; when $\Delta\phi_{12} = \pi$, they interfere destructively. Therefore, when we calculate the $S(\omega)$, we will get the below Fig. 2.21.
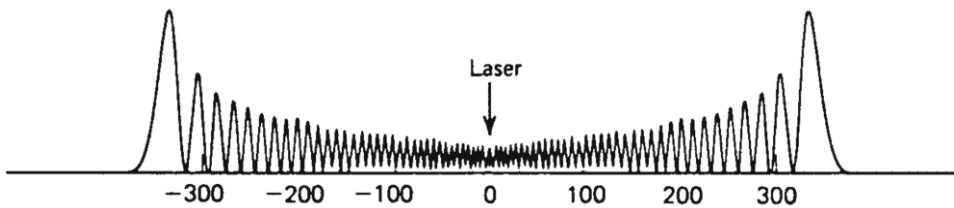
Figure 2.21: The output power spectrum generated by Gaussian fundamental pulse. Adapted from [18].

In this spectrum $S(\omega)$, the red-shifted and blue-shifted parts are Stokes and anti-Stokes broadenings respectively. The Stokes and anti-Stokes parts are symmetric.

2.5.6 Self-steepening

As mentioned above, the intensity-dependent refractive index is:

$$n = n_0 + n_2 I.$$

Therefore, the phase modulation $\Delta\phi$ is direct proportional to the time dependent intensity $I(t)$.

However, medium does not have an instantaneous response. The response time of medium results in a distortion of the phase modulation $\Delta\phi$. Thusly, even though the intensity $I(t)$ is symmetric, the spectrum $S(\omega)$ still show Stokes-anti-Stokes asymmetric.

The group velocity depends on the intensity $I(t)$:

$$v_{group} = \frac{c}{n(I) + \omega\frac{\partial n(I)}{\partial \omega}}, \quad (2.55)$$

where $n(I)$ means the refractive index is modified by laser intensity.

From this Eq. (2.55), we can know the center part of the pulse will have a smaller group velocity because the center part features the peak intensity. Thus, the center part of the pulse falls away from the leading part and comes near the trailing edge. This leads to a steep intensity trailing edge of the pulse and we call this effect self-steepening [125-128]. The following Fig. 2.22 shows self-steepening effect visually. Self-steepening effect can modify the pulse shape in time domain and further affect the temporal SPM.
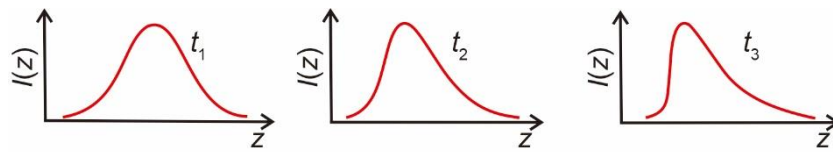
Figure 2.22: Scheme of self-steepening effect of a Gaussian pulse with $t_1 < t_2 < t_3$. Starting at time point t_1 from a standard Gaussian pulse, the pulse peak slows down with respect to the group velocity at time point t_2 and finally form a steep edge in the trailing part at time point t_3.

2.6 Summary

In this chapter, we systematically make an overview on the essential theoretical background which is the basis of the following chapters in this dissertation, such as the contents of ultrashort laser pulse, nonlinear optics, optical parametric amplifier and supercontinuum generation. Also, techniques

for ultrashort pulse characterization which are widely used in modern optical research field, are discussed in considerable detail. Sections 2.1 and 2.2 present the contents of ultrashort laser pulse and nonlinear optics which are the universal physics throughout the whole thesis. Sections 2.3 and 2.4 describe the physics of pulse measurement techniques and optical parametric amplifier which are used to characterize a test pulse. Section 2.5 presents the necessary knowledge about the process of supercontinuum generation which is the core content of this dissertation.

Chapter 3

Negatively chirped supercontinuum generation by ghost pulse

This chapter is devoted to the negatively chirped supercontinuum (SC) generation by ghost pulse which is the core content of this dissertation. The chapter is organized as follows: Section 3.1 is a brief background introduction of SC generation. Section 3.2 is an overview of experimental setups. It describes the approach of the setup design and setup schemes used in this work. The experimental setups mainly consist of 4f-line pulse shaping system, sum frequency generator (SFG) setup, SC generation and SC characterization setups. The 4f-line and SFG setups are used to produce stable ghost pulses. In the Section 3.3 the key units of the SC generation and characterization setups are described in detail, and the concerned experimental results are discussed. Section 3.4 presents a summary and shows the potential applications of our studies.

3.1 Introduction

Supercontinuum (SC) generation has been the research subject of numerous investigations since its first observation by Alfano et al. in the 1970s [20, 21]. Now it represents a unique technique to provide coherent light sources with extremely broad tunable spectrum from near UV to far IR [17-19]. The importance of SC generation is apparent for a variety of applications including ultrafast spectroscopy [38], optical microscopy [39, 40], attosecond science [41], frequency comb technology [42-45], etc. For example, SC generation is on demand for time-resolved pump-probe spectroscopy [38] to study the ultrafast molecular dynamics which occur in solid state physics, chemistry and biology. Moreover, extremely broad SC spectrum is an indispensable seeding source for optical parametric amplifiers [101] which has become a standard tool for the generation of ultrashort pulses exceeding the supporting range by conventional laser instruments.

The physics of SC generation is a subject of continuous in-depth research and shows to be quite complicated. Detailed analyses suggest that SC generation in bulk media arises from a complex interplay between self-focusing, SPM (self-phase modulation) effect and multiphoton absorption/ionization-induced free electron plasma [17-19]. Wherein, self-focusing effect determines the propagation dynamics of the ultrashort laser

pumping laser pulses. SPM effect primarily governs the spectral broadening which introduces new red-shifted and blue-shifted frequencies on the leading and trailing fronts of the driving pulse respectively. However, both the self-focusing and SPM effects are highly affected by the chromatic dispersion which finally determines the extent and shape of the SC spectrum indirectly.

SPM theory suggests that the newly generated SC should feature positive chirp, and thus on the subject of dispersion issue we usually just consider the group velocity dispersion (GVD) of working media. Therefore, SC generation is generally studied in two distinct cases defined by the sign of the media GVD. In the region of normal GVD (positive GVD) of dielectric media, the input pulse broadens temporally owing to GVD. New red-shifted and blue-shifted frequencies generated by SPM effect appear on the leading and trailing fronts of the pulse and are further dispersed. In the case of anomalous GVD (negative GVD), the input wave packet is temporally shrinked leading to the formation of self-compressed pulses and self-phase modulation, the newly generated SC frequencies are swept back to the pulse center.

Before the present work, research attention of SC generation was mostly paid on the comparisons of different pump laser parameters, various dielectric media used for SC generation, and normal/ anomalous GVD of working media. For example, SC generation has been studied with different femtosecond laser sources spanning pump wavelengths from UV to mid-IR [129-131], with different pulse duration [132-134] and even with different shaped beams such as Gaussian, Bessel [135], vortex [136], singular beams [137], etc. Different wide bandgap dielectric media such as glasses [53, 130], water [138], YAG [139], sapphire [140], etc. and normal/zero/anomalous GVD regions [141-143] have also been theoretical studied by numerical simulation models of different complexity, and afterwards confirmed experimentally. Although extensive theoretical and experimental studies have been performed on SC generation, however, no results on negatively chirped SC generation have been reported so far, and the rich variety of GVD induced effects remain unexplored.

In this chapter, we describe a novel method to generate negatively chirped supercontinuum by ghost pulse in normal GVD regime. The ghost pulse is produced by a 4f-line pulse shaping setup and a following SFG process. Driving by this ghost pulse, we have succeeded in generating negatively chirped SC. XFROG and NOPA techniques have been built to characterize the newly generated SC. To our knowledge, this is the first time generated a negatively chirped SC in a material with normal GVD.

3.2 Experimental setups design

In this work, SC generation by ghost pulse has been performed with the use of two kinds of experimental setups and the produced SC is characterized by NOPA and XFROG techniques. A simple overview of the experimental setups is presented in Fig. 3.1. The theoretical aspects of the experimental

design have been demonstrated in section 2.5.5. According to our design approach, negatively chirped SC can be generated by ghost pulses. Therefore, we need to obtain a ghost pule first. In the setups shown in Fig. 3.1, a 4f-line system and an SFG process are responsible for the creation of the desired ghost pulse. The generated SC are characterized by XFROG and NOPA techniques.
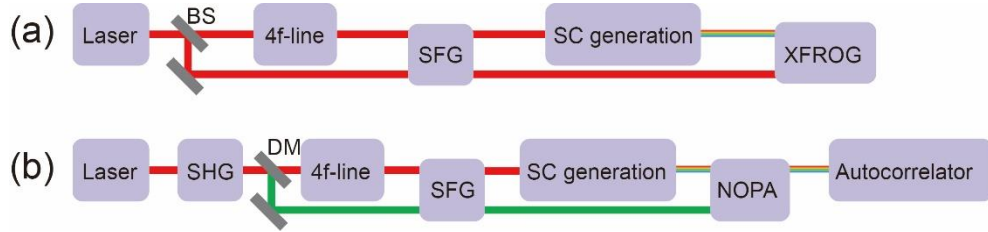
Figure 3.1: An overview of the experimental setups for SC generation by ghost pulse and SC characterization. The red line represents the light path of the fundamental 1028 nm laser beam, the green line denotes the second harmonic of the fundamental pulse and the multicolor line denotes the generated SC. BS - beam splitter; DM - dichroic mirror.

The 4f-line can produce a long pulse ($\tau_p = 1 - 7\ ps$) by narrowing the spectral bandwidth of the fundamental pulse ($\tau_p \approx 200\ fs$). The following SFG process is used to create a ghost pulse by depleting the energy near the center of the long pulse. In setup (a), the SFG process is performed using beams at the same wavelength ($\lambda_0 = 1028\ nm$) but with different durations ($\tau_p \approx 2\ ps$ and $200\ fs$). The generated SC is characterized by a home-built XFROG setup. In the setup (b), an additional SHG process is added before the 4f-line to produce the second harmonic ($\lambda_0 = 514\ nm$) of the fundamental beam, and in this case the SFG process is carried out between the fundamental and the second harmonic beams. The generated SC is characterized by a NOPA setup and a commercial autocorrelator is also adopted to further measure the pulse duration of the NOPA output. The red, green and multicolor lines in Fig. 3.1 denote the paths of the fundamental 1028 nm laser beam, the second harmonic 514 nm laser beam and the generated SC, respectively.

In this work, the setup in Fig. 3.1(a) was first built to implement the generation of negatively chirped SC by ghost pulse. Fig. 3.2 presents a simplified scheme of the experimental setup Fig. 3.1(a). The Yb:KGW laser system delivers linearly polarized pulses of duration ~200 fs at 1028 nm with 2 kHz repetition rate. The initial laser pulse is divided into two beams $E_1(t)$ and $E_2(t)$ by a beam splitter. As shown in Fig. 3.2, one beam $E_1(t)$ is guided into a 4f-line pulse shaping system which is built using a folded optical geometry. The grating in 4f-line converts the input pulses from time domain to frequency domain and thus all frequency components are spatially separated in Fourier plane. Two metal plates are placed in the Fourier plane to form a narrow slit. Only the central finite frequencies are not blocked by the plates

and thus the spectral bandwidth of the input pulse becomes narrower. According to Fourier transform limit, the duration of a given pulse is limited by its spectral bandwidth:

$$\tau_p \geq \frac{TBP \cdot \lambda^2}{c \cdot \Delta\lambda}, \quad (3.1)$$

where τ_p is the pulse duration, TBP - the time bandwidth product, λ - the central wavelength of laser beam, c - the speed of light and $\Delta\lambda$ - the spectral bandwidth of laser beam. As illustrated in Eq. (3.1), pulse length τ_p is inversely proportional to its spectral bandwidth $\Delta\lambda$. Narrower spectral bandwidth leads to longer pulse duration. Thereby, the output pulse $E_{4f}(t)$ shaped by the 4f-line will feature long duration. Afterwards, the long pulse $E_{4f}(t)$ and the short pulse $E_2(t)$ are focused and overlapped inside a nonlinear crystal to perform the SFG process. Here a 2 mm type I BBO (θ = 23.4°) crystal is used. Due to the energy transfer happened in the SFG process, the pulse intensity of the overlapped part of the long pulse $E_{4f}(t)$ is depleted, and thus a ghost pulse $E_{ghost}(t)$ looking like the one shown in Fig. 2.20 (b) is obtained. The short pulse $E_2(t)$ could be also slightly affected by the SFG process and here the pulse $E_2(t)$ after the SFG BBO crystal is labelled as $E_2'(t)$.
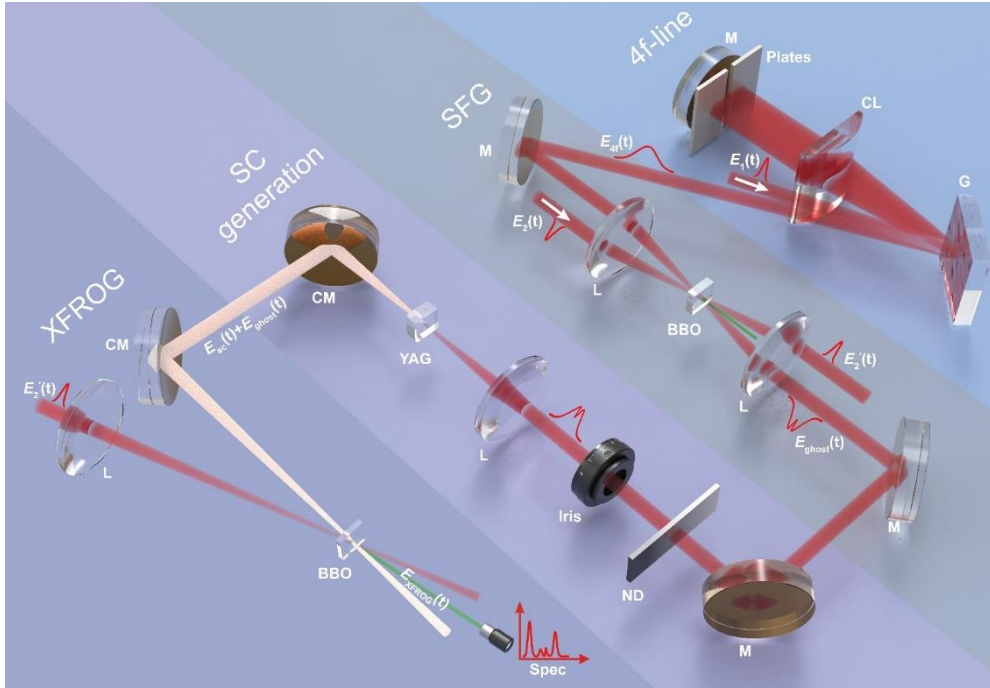
Fig. 3.2: Simplified scheme of the experimental setups for SC generation by ghost pulse and SC characterization by XFROG technique. White arrows in this figure denote the propagation direction of the two input pulses $E_1(t)$ and $E_2(t)$. Two plates are placed in the Fourier plane of the 4f-line pulse shaping system so that the spectral bandwidth of the input pulse is narrowed. In thus, the input pulse is temporally expanded. In the following SFG setup, the energy transfer happened in the nonlinear SFG process deplete the intensity of a part

of the long pulse in time domain, which will create a ghost pulse. In the SC generation, a neutral density filter and an iris are inserted before the focal lens to adjust the pumping power and beam size respectively. The SC generation is performed using a YAG crystal. A home-built XFROG setup is used to characterize the generated SC. G is grating; CL - cylindrical lens; M- mirror; L- lens; ND - variable neutral density filter; CM - concave mirror; Spec - spectrometer.

According to our approach, the ghost pulse $E_{ghost}(t)$ will be used to generate negatively chirped SC. In the setup part of SC generation, before the crystal for SC generation a variable neutral density filter is used to adjust the laser power because SC generation is inherently very sensitive to variations in the driving power. An iris is also inserted to extract the small core size of the beam where the laser intensity distribution is spatially uniform. Then the ghost pulse $E_{ghost}(t)$ created by SFG process is focused into a bulk media to generate negatively chirped SC. Here a 4 mm YAG crystal is used for SC generation.

The chirp of the generated SC is characterized by a following XFROG setup. Specifically, the generated SC pulse $E_{SC}(t)$ together with the ghost pulse $E_{ghost}(t)$ are collimated and refocused into a thin type I BBO (20 μm thick, θ = 23.4°) crystal by two concave mirrors. The reference beam is $E_2'(t)$ which is also focused into the same BBO and overlapped with pulses $E_{SC}(t)$ and $E_{ghost}(t)$ temporally and spatially. The spectrum of the resulted SFG pulse is recorded as a function of the variable delay time. In order to describe the setup clear, in Fig. 3.2 some optical elements are neglected such as wave plates, delay line, etc. More details about the setups can be found in Figs. 3.3 and 3.4, and Sections 3.3 and 3.4.

Fig. 3.3 shows a further detailed scheme of setup Fig. 3.1(a). The input beam is vertical polarized. However, the grating in the 4f-line requires an input beam with horizontal polarization to achieve a high diffraction efficiency. Therefore, a half-wave plate is used before the 4f-line to rotate the beam polarization from vertical to horizontal. In the following SFG process, the polarization of two input beams should meet the type I phase matching condition, and thus a second half-wave plate is needed to change back the beam polarization from horizontal to vertical. A detailed scheme of the experimental setup Fig 3.1(b) can be found in Fig. 3.4. This setup is similar to the setup shown in Fig. 3.3, but an additional thick BBO crystal (5 mm thick, type I, θ = 23.4°) is added for the second harmonic generation. In the case of this setup, the ghost pulse is produced by the SFG process between the fundamental pulse and the second harmonic pulse. The SFG process does not deplete too much the second harmonic beam and the residual energies is used as the pump beam in the NOPA setup unit.
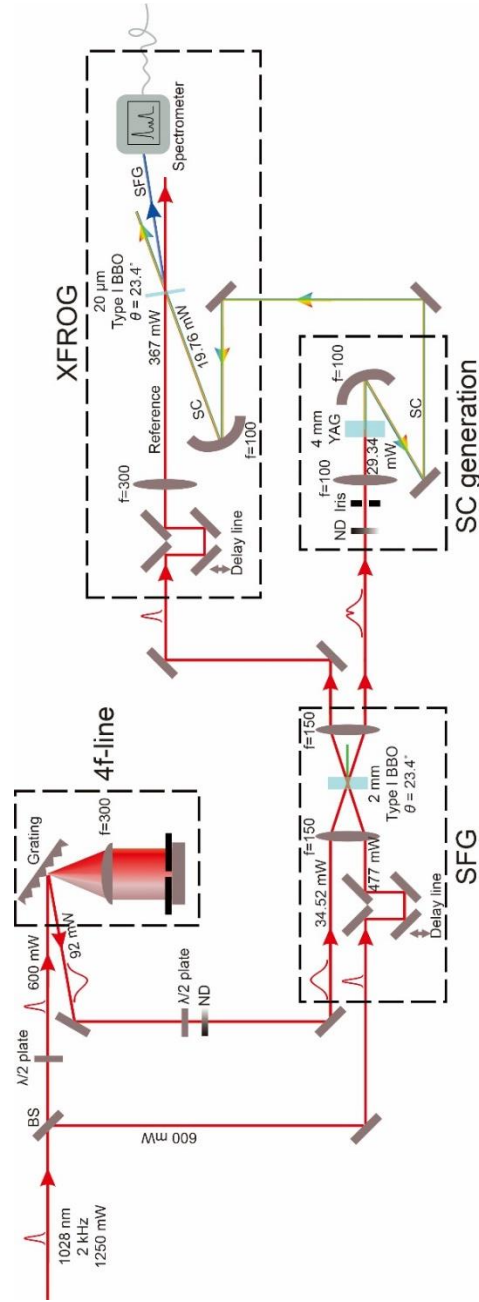
Fig. 3.3: Detailed scheme of the experimental setup using only fundamental wavelength ($\lambda_0 = 1028\,nm$). The beam powers are measured at some key positions and labeled in this figure. Some other details are also noted such as the focal lengths of lenses, thickness and cutting angles of the BBO crystals, etc. Two half-wave plates are inserted before the 4f-line and the SFG setup to adjust the beam polarization. In the SFG process, a type I BBO crystal is used. Two delay stages are built inside the units of SFG and XFROG setups. The delay stages allow one to finely adjust the temporal overlap of laser beams inside the BBO crystals. The red line represents the light path of the 1028 nm laser beam and the multicolor line denotes the generated SC. BS is beam splitter; DM - dichroic mirror; ND - variable neutral density filter.
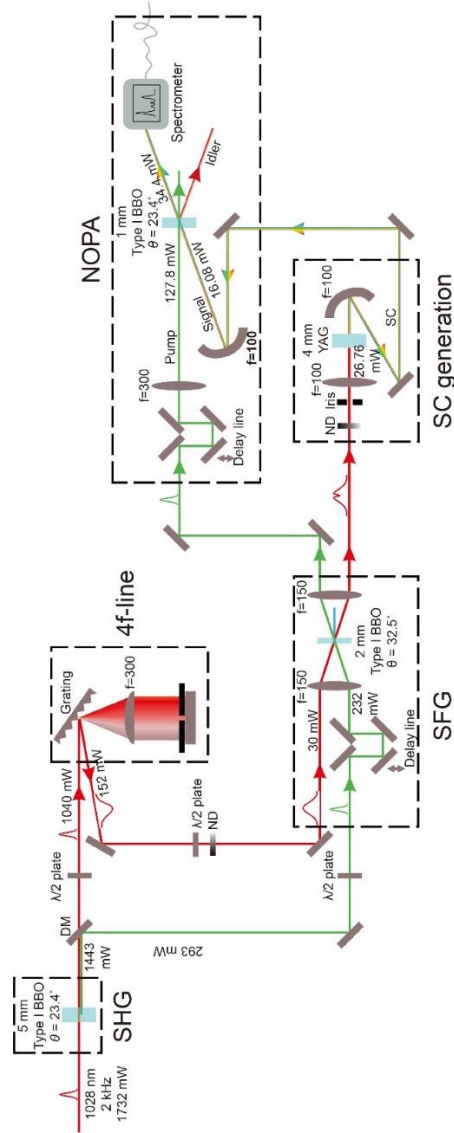
Fig. 3.4: Detailed scheme of the experimental setup using fundamental beam ($\lambda_0 = 1028\ nm$) and its second harmonic ($\lambda_0 = 514\ nm$) for SC generation by ghost pulse and SC characterization. The beam powers are measured at some key positions and labeled in this figure. Some other details are also noted such as the focal lengths of lenses, thickness and cutting angles of the BBO crystals, etc. Three half-wave plates are inserted before the 4f-line and the SFG process to adjust the beam polarization, respectively. In the SFG process, a type I BBO crystal is used. Two delay stages are built inside the units of SFG and XFROG setups respectively. The delay stages allow one to finely adjust the temporal overlap of laser beams inside the BBO crystals. The red line represents the light path of the 1028 nm laser beam, the green line indicates the light path of the 514 nm second harmonic laser beam, the blue line denotes the SFG signal and the multicolor line denotes the generated SC. BS is beam splitter; DM - dichroic mirror; ND - variable neutral density filter.

3.3 Supercontinuum generation by ghost pulse

3.3.1 Laser system

In this work, we use a commercially available femtosecond laser system "PHAROS SP" from Light Conversion in Lithuania [144]. Table 3.1 is a summary of the main output parameters of our laser system. As shown in this table, the PHAROS laser has output femtosecond pulse with high energy (1 mJ) and high average power (6 W). Some of its parameters can be tuned conveniently, such as average power (up to 6 W), pulse energy (up to 1 mJ), pulse duration (190 fs - 20 ps) and repetition rate (single pulse to 1 MHz). In this work, the laser system outputs of 1.8 W average power at 2 kHz repetition pulse are used. The pulse duration is typically adjusted to be close to Fourier transform limited.

Table 3.1 Output characteristics of our laser system. The 2nd column data is taken from the official website of Light Conversion company. [144]

Model	Pharos SP	In this work
Max. average power	6W	1.8 W
Pulse duration range (assuming Gaussian pulse shape)	190 fs (bandwidth -limited) – 10 ps	192 fs
Max. pulse energy	1 mJ	0.9 mJ
Base repetition rate	1 kHz – 200 kHz	2 kHz
Centre wavelength	1028 ± 4 nm	1028 ± 4 nm
Polarization	Linear, horizontal	Linear, horizontal
Room temperature	15 – 30 ℃	26 ℃

Fig. 3.5 presents the output spectrum of PHAROS laser system characterized by a commercially available spectrometer (HR 2000, Ocean Optics). The achievable wavelength resolution of spectrometer is about 0.47 nm. The Gaussian fitting result reveals that the laser wavelength is 1028 ± 4 nm which agrees with the manual data.
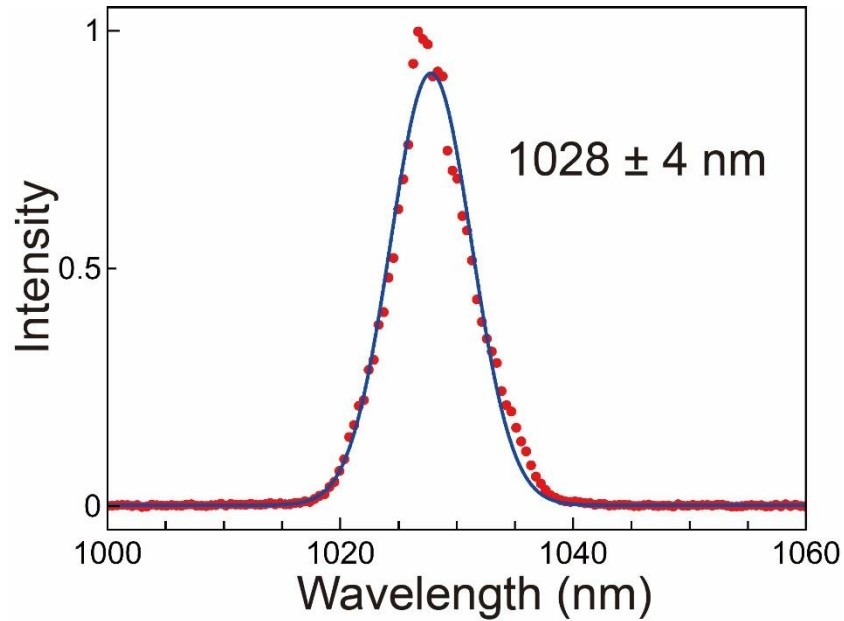
Figure 3.5: Spectrum of Pharos laser output. The red dots denote the measured spectral data. The solid blue line presents the Gaussian fitting curve which shows the center wavelength is 1028 nm and the bandwidth is about 8 nm.

Substituting our experimental values (λ_0 = 1028 nm and $\Delta\lambda$ = 8 nm) into Eq. (3.1), and considering TBP = 0.44 (for Gaussian pulse), the Fourier transform limited τ_p can be calculated:

$$\tau_p = 193 \text{ fs.}$$
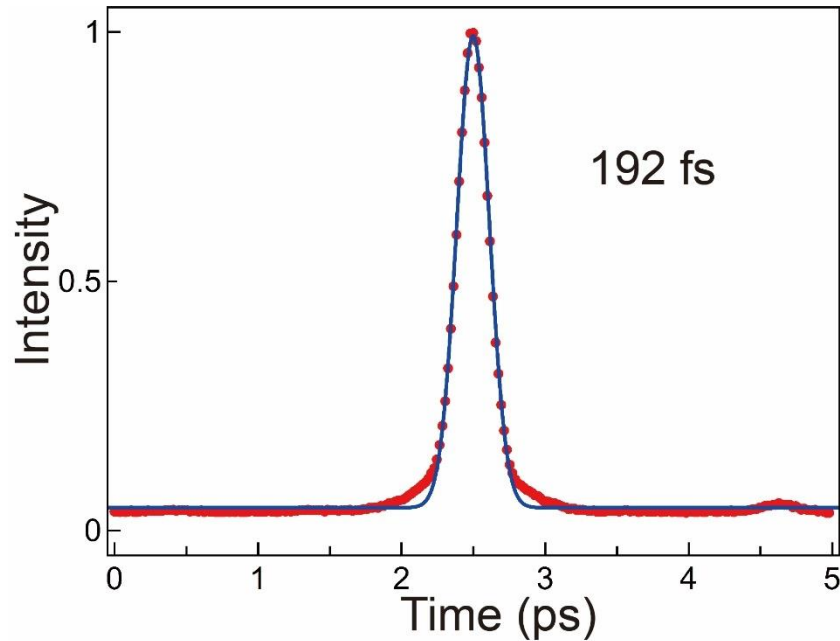
Figure 3.6: The achievable shortest duration time of laser output pulse. The red dots denote the measured autocorrelation data. The solid blue line presents the Gaussian fitting curve which shows the duration time is about 192 fs.

The pulse duration is checked using a commercial autocorrelator (PulseCheck, APE GmbH, Berlin). Tuning the compressor inside the laser system, we find that the shortest achievable duration time is about 192 fs (see Fig. 3.6) which matches the theoretical value well.

3.3.2 Second harmonic generation setup

The SHG setup shown in Figs. 3.1(b) and 3.4 is accomplished via a BBO crystal. The average power of the fundamental (λ_0 = 1028 nm) pump beam is ca. 1.8 W (corresponding to 0.9 mJ pulse energy). Fig. 3.7 is a schematic depiction of the SHG setup. In the SHG process, a type I BBO crystal (thickness 5 mm, θ = 23.4°) yields ca. 20.3% conversion efficiency. Generally, if we do not focus the incident beam into BBO crystal, the SHG conversion efficiency is in range of 15-25%. Our BBO crystal used here is not coated with an anti-reflection surface which lead to a serious power loss. The second harmonic is reflected by a dichroic mirror which is designed for high reflection at 532 nm and high transmission at 1064 nm. Fig. 3.8 presents the measured spectrum of the second harmonic pulse. The intense residual fundamental component passes through the dichroic mirror directly.
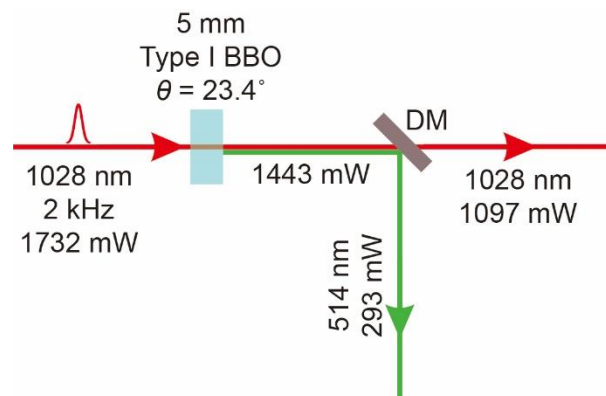
Figure 3.7: Schematic depiction of the SHG process: BBO is a type I crystal of 5 mm thickness and θ = 23.4°; DM - dichroic mirror.
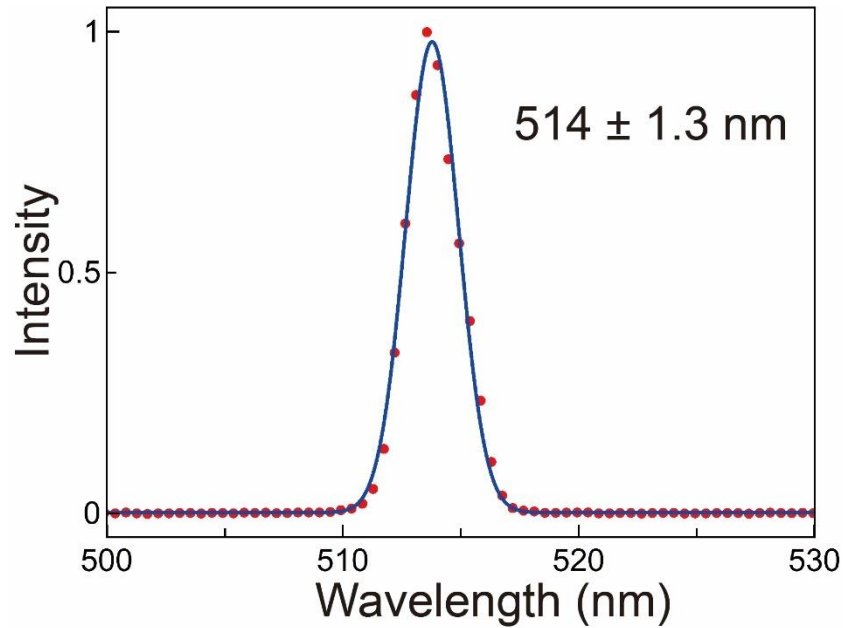
Figure 3.8: Spectrum of second harmonic 514 nm beam measured behind the dichroic mirror. The red dots denote the measured spectral data. The solid blue line presents the Gaussian fitting curve which shows the center wavelength of 514 nm and the bandwidth of 2.6 nm.

Some publications [145-148] investigated the relationship between the spectral bandwidths of the fundamental pulse and the second harmonic. Ehmke et al. [148] suggested a narrowing factor of $\frac{1}{2\sqrt{2}} \approx 0.35$ of the second harmonic wavelength bandwidth compared to the fundamental pump pulse. Therefore, in our case, the spectral bandwidth of the second harmonic 514 nm pulse should be $8 * \frac{1}{2\sqrt{2}} \approx 2.8$ nm. Our experimental measured result, as shown in Fig. 3.8, reveals that the spectral bandwidth is about 2.6 nm which is a little narrower than the predicted value. The different phase matching conditions which can alter the spectral shape and influence the spectral bandwidth should be responsible for the narrow spectral bandwidth of second harmonic pulse [149-151].

3.3.3 4f-line pulse shaping and XFROG setups

Although now mode-locked lasers based on solid state gain media are the most widely used laser source of ultrashort pulses. However, sometimes we need flexible laser pulses which can not be satisfied by commercial laser sources. For solving this problem, we need to adopt the technology of pulse shaping which can be treated as an important complement to femtosecond pulse generation.

In 1983, Froehly developed a 4f-line system for pulse shaping [152]. This is a kind of zero dispersion system and now widely adopted for generating almost arbitrarily shaped ultrashort pulses. As shown in Fig. 3.9 (a), the 4f-line includes two gratings, two lenses and one pulse shaper. The distance between two adjacent optical components is f (the focal length of lens). This is the reason why we call it 4f-line. Pulse shaping in time domain directly is difficult due to the limited response time of electronic devices and thus pulse shaping process is generally carried out in frequency domain. In the 4f-line system, the input pulse is decomposed into different spectral components by a grating and a lens. This converts the input pulses from time domain to frequency domain. The second lens and grating recover the shaped pulse from frequency domain to time domain. In the Fourier plane, a pulse shaper is inserted and used to modulate the phase, amplitude and polarization of pulses. It is the device which carries out pulse shaping process.
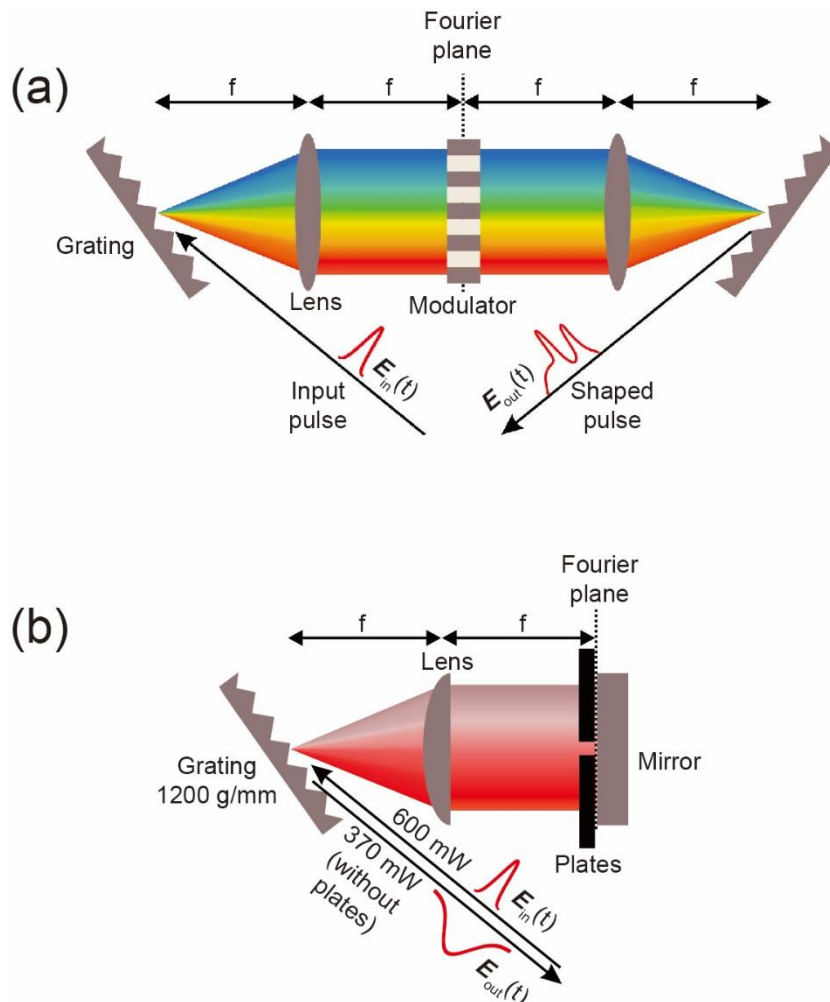
Figure 3.9: (a) Scheme of a typical 4f-line setup. This is a zero dispersion system and the output pulse is identical to the input pulse. A modulator is used in the Fourier plane to program the input pulse. (b) A scheme of the 4f-line used in this work. It is built by folded optical geometry which is composed of

one grating (1200 grooves/mm), one cylindrical lens and one reflection mirror in the Fourier plane. All different frequencies are spatially separated and focused in the Fourier plane. Two metal plates placed next to the Fourier plane works like a filter to block spectral components.

In practice, 4f-line can be performed in different optical geometries [153-155]. Fig. 3.9(a) presents the standard style of the 4f-line. In this work, a folded optical geometry of the 4f-line was adopted, as presented in Fig. 3.9(b). It just includes one grating, one cylindrical lens and one reflection mirror at the position of Fourier plane. The grating (10RG1200-1000-2, Newport Company USA) used here has typical diffraction efficiency in the m = -1 diffraction order about 62% (measured) at the Littrow angle for wavelength 1028 nm. Its specification is summarized in Table 3.2. The focal length of cylindrical lens (LJ1212L1, Thorlabs GmbH, Dachau, Germany) is 300 mm. This kind of geometry is almost aberration-free and does not have many degrees of freedom. Thus, it is convenient to be well aligned.

Table 3.2: The specifications of grating used in this work.

Specifications	
Type	Ruled
Wavelength of maximum efficiency	1000 nm
Nominal blaze angle	36.8°
Grooves per mm	1200
Tolerance wavelength on nominal blaze angle	± 25 nm (first order, Littrow, typical)

The 4f-line system must be aligned very carefully because misalignment introduces spatial chirp and lead to bad beam quality. The alignment procedure is briefly described here. Firstly, make sure that the input laser is horizontal to the laser table. This can be checked by steering laser through two small irises at the same height. Then, the grating should be mounted perpendicular to the table plane, which can be achieved by observing different diffraction orders to be along the line parallel to the laser table. The cylindrical lens is placed at a distance of focal length from the grating. The mirror is placed at the Fourier plane and is adjusted to reflect the beam back to the grating. For separating the output beam from the input beam, we can tilt the mirror a little so that the output beam is slightly higher than the input beam.

If the 4f-line is well aligned, it should be ideally free of temporal and spatial dispersions. The output beam should be exactly the same as the input beam both in temporal and spatial domains when we take away the metal plates.

For testing the setup, the pulse length before 4f-line is adjusted to be

transform limited and measured using a commercial autocorrelator (see Fig. 3.10(a)). The pulse length after the 4f-line is also verified by the autocorrelator to be Fourier transform limited, as shown in Fig. 3.10(b). We can find that the duration time remains nearly unchanged before and after the 4f-line. This result proves the 4f-line does not introduce distortion in temporal domain. For visualizing the spatial dispersion, we can sweep a card across the spatially dispersed light in the Fourier plane. If there is dispersion at the output, we can observe changes of beam profile at a faraway position. If there is no dispersion, the output beam will be just attenuated as the card block some frequencies in the Fourier plane.
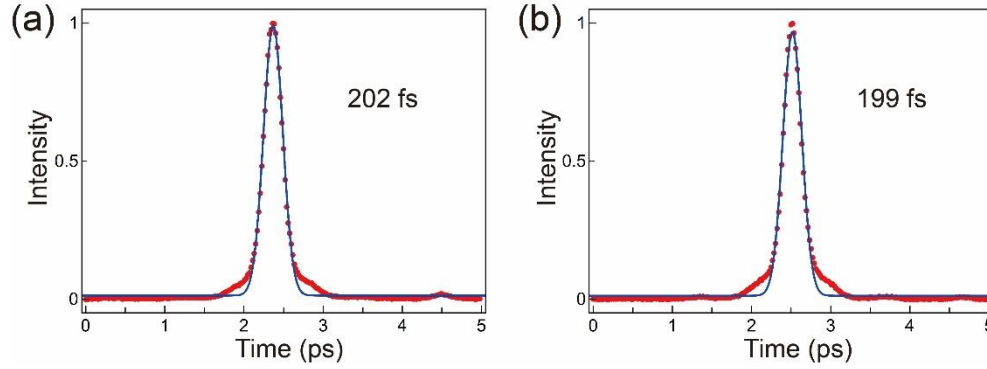
Figure 3.10: The pulse durations of fundamental pulse ($\lambda_0 = 1028$ nm) measured (a) before and (b) after the 4f-line system. The red dots denote the measured data. The solid blue line presents the Gaussian fitting curve which shows the pulse durations before and after the 4f-line to be around 200 fs.

In this work, our purpose is to obtain a long pulse according to the Fourier transform limit and thus the programable modulator in the 4f-line is not necessary. Now considering that the incident pulse features Gaussian shape in time and space, the central wavelength is λ_0, and Δx_{in} is the FWHM in spatial domain. As shown in Fig. 3.11, incident angle is θ_i and central wavelength λ_0 of the input beam is diffracted at angle θ_d. Here, d is grating period and f is focal length of lens. In the Fourier plane, the size of each spectral component is Δx_0. Calculating by several simple mathematic steps, we can get:

$$\Delta x_0 = 2ln\,(2)\frac{cos\theta_i}{cos\theta_d}\frac{f\lambda_0}{\pi\Delta x_{in}}. \quad (3.2)$$

This means each frequency spreads over such a spatial size Δx_0. Therefore, the parameter Δx_{in} can be narrowed by using plates to block selected frequencies in the Fourier plane.
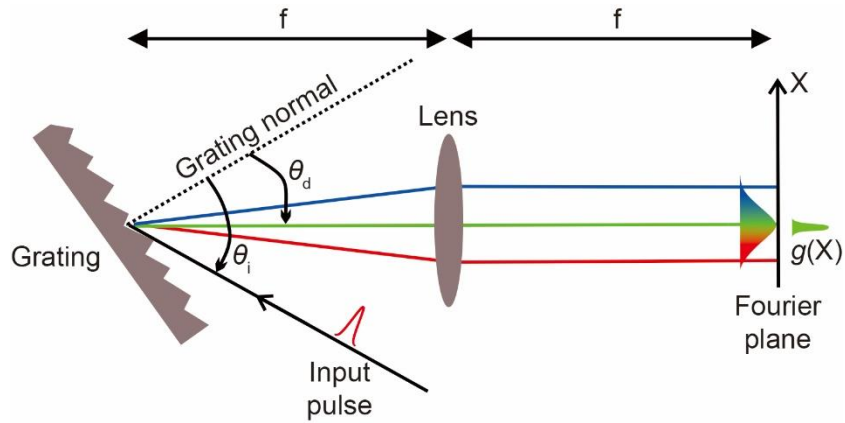
Figure 3.11: Scheme of a half 4f-line. The Fourier plane is located at the back focal plane of the lens. θ_i denotes the incident angle on the grating; θ_d is the diffraction angle; X denotes the spatial coordinate of the Fourier plane; $g(X)$ represents the spatial size of a given frequency component.

As we have mentioned in Section 3.2, the minimum duration of a given pulse is limited by its spectral bandwidth. Specifically, pulse duration is inversely proportional to spectral bandwidth. Therefore, as we narrow the spectral bandwidth of the input light by blocking frequency components in the Fourier plane of the 4f-line, the pulse duration of the output light should become longer. Fig. 3.12 shows a series of autocorrelation curves obtained by gradually narrowing the spectrum's FWHM. As it should be, narrower spectrum leads to longer duration time.
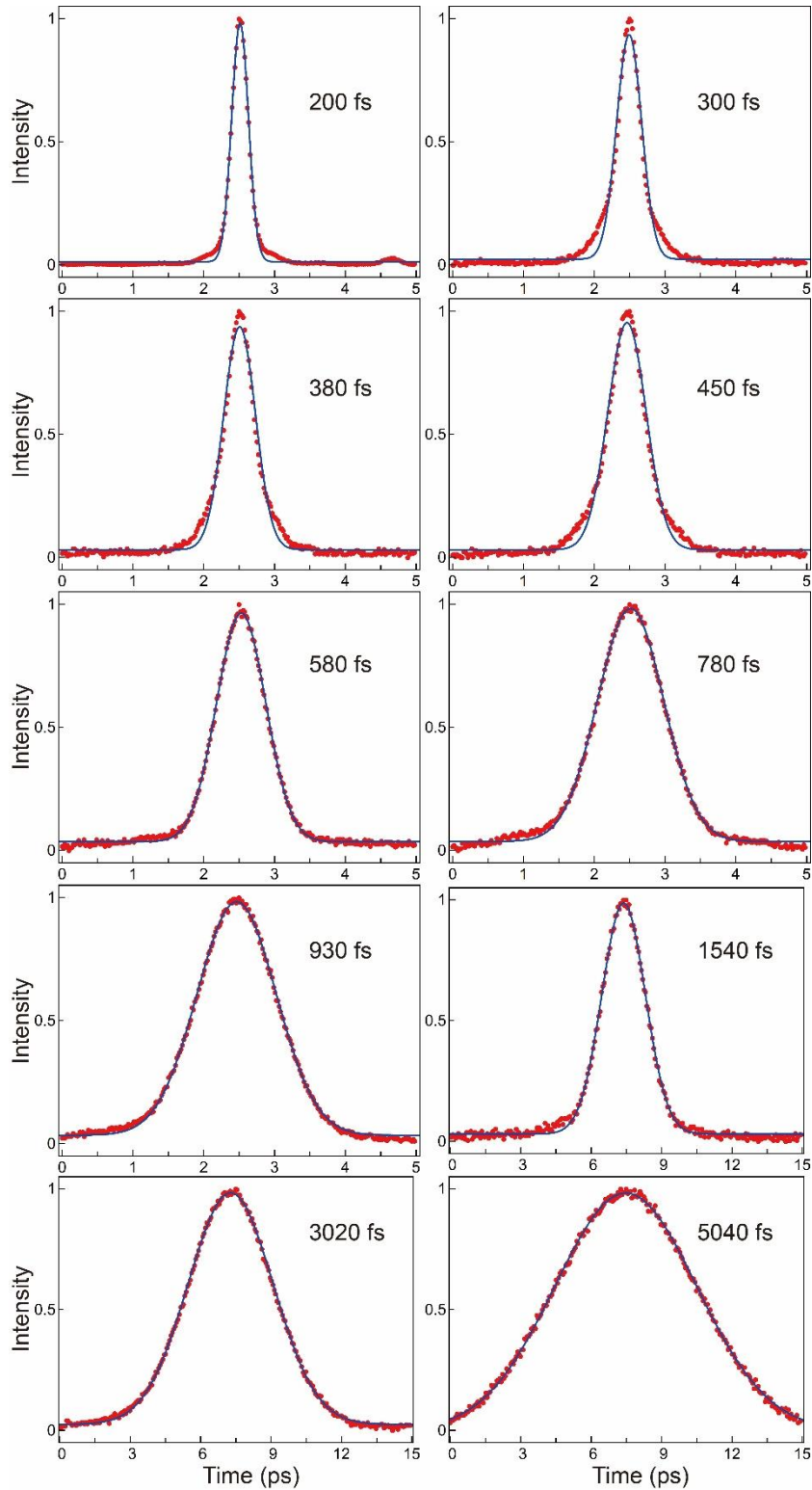
Figure 3.12: Changes of autocorrelation curve width after pulse shaping in the 4f-line system. The red dots denote the measured data. The solid blue lines represent the Gaussian fitting curves.

As we have discussed in chapter 2, autocorrelator is not a complete characterization method because it operates purely in time domain. FROG

technique allows a clear view of pulse duration together with chirp information [74-81]. Thus, we also build a XFROG setup here to characterize the created long pulse by the 4f-line and the generated SC. Fig. 3.13 presents a scheme of the XFROG setup. The generated SC is focused inside a BBO crystal (type I, 20 μm thickness, $\theta = 23.4°$) by a concave mirror ($f = 100$ mm). Here, a thin BBO crystal (20 μm thickness) is chosen for avoiding additional positive chirp and this also enables a high temporal resolution of the XFROG measurement. The fundamental 1028 nm pulse $E(t)$ with short duration ($\tau_p \approx 200 \, fs$) is used as the reference beam and is also focused into the same BBO crystal by a lens ($f = 300$ mm). A hand-tuned optical delay stage is inserted in path of the reference $E(t)$ beam to vary the time delay between the reference and SC beams for achieving an exactly temporal overlap between them inside the BBO crystal. The intensity and spectrum of resulted SFG beam is recorded by a spectrometer as a function of different delay time t.
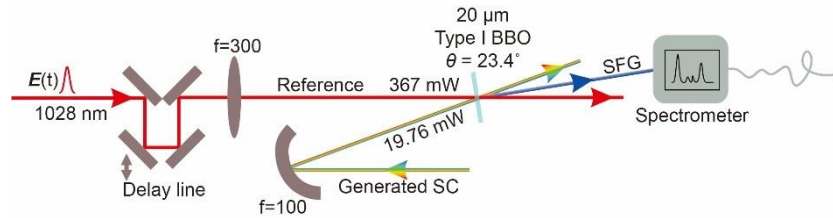
Figure 3.13: Scheme of the XFROG setup: the test SC and reference beam (fundamental 1028 nm pulse $E(t)$) are focused into a thin BBO crystal (type I, 20 μm thickness, $\theta = 23.4°$) by a concave mirror ($f = 100$ mm) and a lens ($f = 300$ mm), respectively. The resulted SFG beam is measured and recorded by a spectrometer.

In this XFROG setup, the fundamental 200 fs 1028 nm pulse serves as the reference beam. Firstly, we avoid SFG process in the setup (see Fig. 3.3) by moving the delay line. At the same time, we shift the YAG crystal a little to avoid SC generation, and then run the XFROG. For this case, we get the result shown in Fig. 3.14(a) which proves that the 4f-line produces a long pulse successfully. Fig. 3.14(b) indicates that the pulse duration is about 2.1 ps.
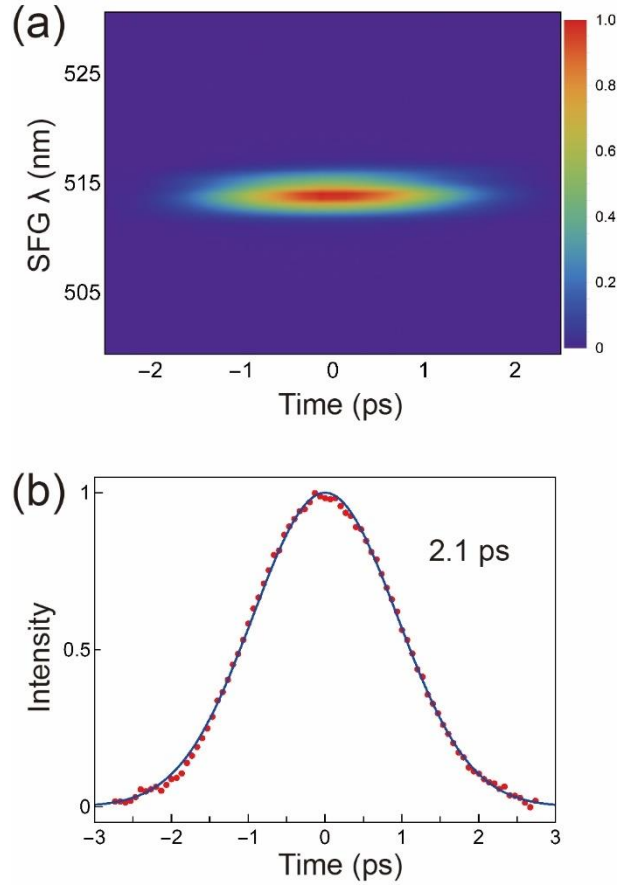
Figure 3.14: The XFROG results of (a) the long pulse created by 4f-line, (b) the intensity integration of this long pulse revealing that the pulse duration is about 2.1 ps. The red dots denote the measured data. The solid blue line represents the Gaussian fitting curve.

3.3.4 Sum frequency generation process

In principle, ghost pulse can be achieved by different nonlinear optical processes, such as Kerr effect, SFG, etc. In this study, SFG effect is chosen for the creation of a stable ghost pulse. As depicted in Fig. 3.15, SFG setups are built using different incident beams. In case (a), the wavelengths of both incident beams are 1028 nm, but one beam $E_{4f}(t)$ is shaped by the 4f-line and the other one is the fundamental 1028 nm beam $E(t)$. In case (b), the beams for performing SFG process are 1028 nm beam $E_{4f}(t)$, and the second harmonic 514 nm beam $E_{SHG}(t)$. Type I phase matching is chosen for SFG process and thus both input beams should have the same polarization. In case (a), the BBO is type I, 2 mm thickness, $\theta = 23.4°$, while for case (b), the specification of BBO crystal is type I, 2 mm thickness, $\theta = 32.5°$. The focal length of lenses used here is chosen to be 150 mm for forming suitable beam sizes at focal position.

Note that, the lenses used in case (b) are made from CaF_2 material which transmits light both at 514 nm and at 1028 nm and has low GVD. If we have

the SFG from the beams $E_{4f}(t)$ and the fundamental $E(t)$ (or the second harmonic $E_{SHG}(t)$), the energy of $E_{4f}(t)$ at the overlap area is depleted. Thus, the pulse $E_{4f}(t)$ has hole and is our ghost pulse. We label this ghost pulse generated by the SFG process as $E_{ghost}(t)$.

For checking the SFG setup we detect the signal of sum frequency. In case (a), the wavelength of sum frequency beam generated by SFG process is around 514 nm. It has green color and thus we can observe the sum frequency beam by eye directly.
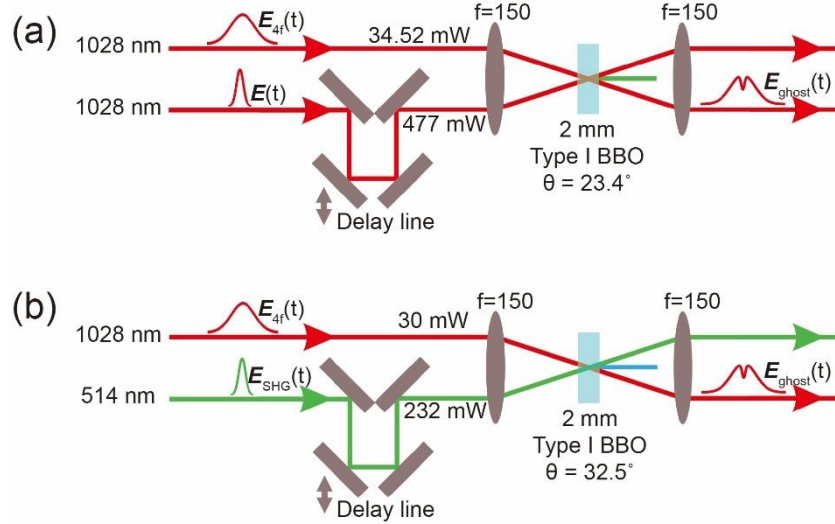
Figure 3.15: Scheme of the ghost pulse creation by the SFG process: (a) the wavelength of both incident beams is 1028 nm and one beam comes from the 4f-line while the other beam is the short-pulse 1028 nm beam; (b) the SFG process is carried out by 1028 nm beam obtained by 4f-line and 514 nm generated by SHG process. The BBO crystal used in (a) is type I, 2 mm thickness, θ = 23.4°, while in (b) is type I, 2 mm thickness, θ =32.5°. A delay line stage is built to adjust the temporal overlap of the two beams inside the BBO crystal.

In order to verify that the ghost pulse can be created by the SFG process, we firstly did some theoretical simulations. Figs. 3.16(a) and (b) depict theoretical calculated curves that a Gaussian pulse features a negatively ghost Gaussian pulse at the center position. The depths of the ghost pulse are 50% and 90% in cases (a) and (b) respectively. Figs. 3.16(c) and (d) present the corresponding autocorrelation curves for pulses shown in 3.16(a) and (b). Afterwards, we experimentally measured the autocorrelation curves behind the SFG BBO crystal with and without the SFG process respectively. Fig. 3.17 shows an experimental example in which the pulse duration of pulse $E_{4f}(t)$ is shaped to be ~750 fs. When we block the fundamental beam $E(t)$ (or the second harmonic $E_{SHG}(t)$), the measured autocorrelation curve presents the pulse lengths of beam $E_{4f}(t)$, as shown in Fig. 3.17(a). When we open the

fundamental beam $E(t)$ (or the second harmonic $E_{SHG}(t)$), the pulse length of beam $E_{ghost}(t)$ is measured, as shown in Fig. 3.17(b). The shape of autocorrelation curve matches our theoretical calculation (Fig. 3.16). This experimental result proves the creation of the ghost pulse by the SFG process.
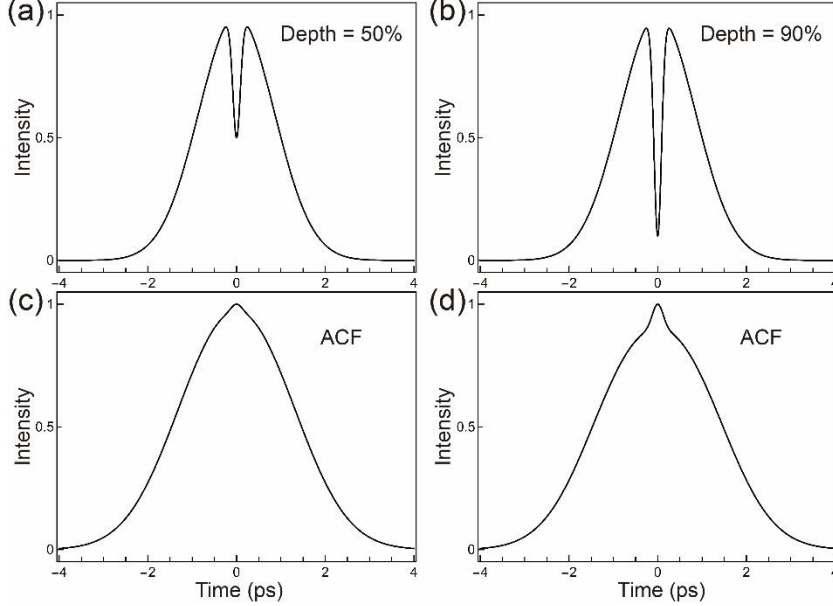
Figure 3.16: Simulated curves of a long Gaussian pulse (τ_p = 2 ps) with a centered short inverse Gaussian pulse (ghost pulse) (τ_p = 200 fs) at different depths (a) 50% and (b) 90%. (c) and (d) are simulated autocorrelation function (ACF) curves for the pulses shown in (a) and (b), respectively.
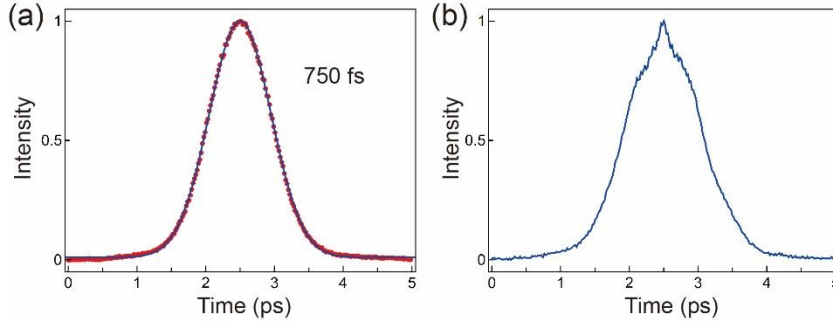
Figure 3.17: (a) Autocorrelation curve of the long 1028 nm pulse $E_{4f}(t)$ obtained by the 4f-line and its Gaussian fitting. The red dots denote the measured data. The solid blue line represents the Gaussian fitting curve. (b) Autocorrelation curve of the ghost pulse $E_{ghost}(t)$. The curve shape matches the theoretical result and indicates the formation of a ghost pulse as a hole of about 90% depth.

The XFROG setup is also used to characterize the ghost pulse. Because the SC generation setup is located before the XFROG setup (see Fig. 3.2), we need to shift the YAG crystal to avoid the SC generation first and then adjust the pulse duration of $E_{4f}(t)$ to be ~2 ps. Fig. 3.18(a) shows the XFROG

results with a hole at the center position of the pulse. Fig. 3.18(b) shows the corresponding intensity integration curve which presents the XFROG projection of the ghost pulse. It directly proves that we can create a ghost pulse by performing SFG process between the long carrier pulse and the short fundamental pulse. Figs. 3.18(c) and (d) respectively present the theoretical calculated and experimental measured autocorrelation curves of this ghost pulse. The curves in Fig. 3.18(d) agrees with the curve in Fig. 3.18(c). Thusly, the autocorrelation curve can also verify the formation of the ghost pulse.
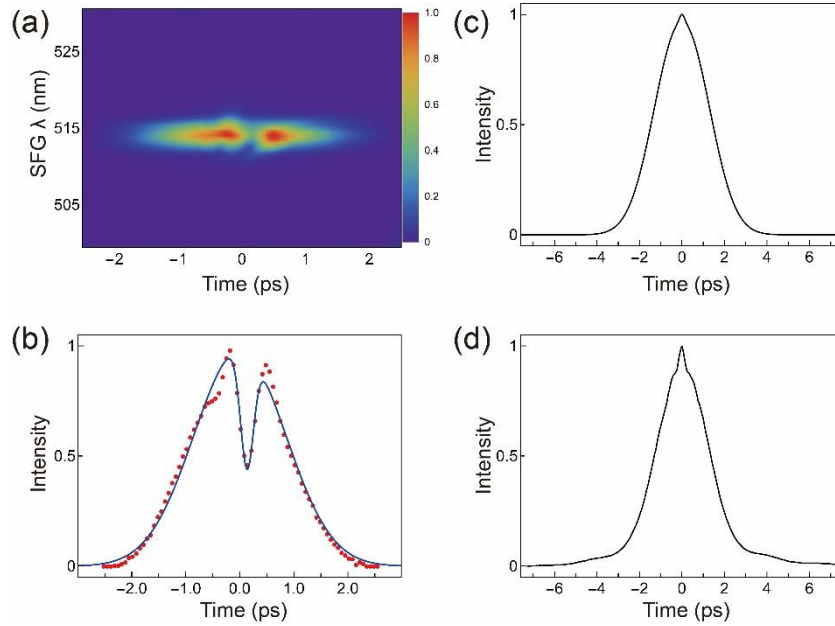
Figure 3.18: (a) XFROG result of pulse $E_{ghost}(t)$ proving that a ghost pulse is created by the SFG process. (b) The plotting of intensity sum of the XFROG result (red dots), and its Gaussian fitted profile (blue curve) which shows the XFROG projection of the ghost pulse. (c) The simulated autocorrelation curve of the pulse shown in (b). (d) The experimental measured autocorrelation curve of the pulse shown in (b).

3.3.5 Supercontinuum generation by ghost pulse and its characterization by XFROG and NOPA-technique

For guaranteeing the generation of reproducible and stable SC within a desired wavelength range, the primary issue is to choose a proper nonlinear medium. Fig. 3.19 summaries the widely used nonlinear media, different driving laser sources and the corresponding spectra of the generated SC. Using different media and different driving lasers, different SC will be produced. In this work, YAG and sapphire crystals are used as the media for the SC generation due to their outstanding physical properties, such as transparency range and nonlinear index of refraction. Table 3.3 lists the GVD coefficients and refractive indexes of YAG and sapphire at 1028 nm pump wavelength. We

firstly used a thick 4 mm YAG crystal for SC generation by ghost pulse. The setup for SC generation is shown in Fig. 3.20. The ghost pulse $E_{ghost}(t)$ is focused into a 4 mm YAG crystal by a lens (f = 100 mm) to generate SC which is further collimated by a concave mirror with 100 mm focal length. A variable neutral density filter and an iris are inserted before the focusing lens to adjust the laser power and beam size, respectively. For minimizing the GVD effect induced by the YAG crystal, the pumping beam should be focused as close to the far side of the crystal as possible, as depicted in Fig. 3.21. In order to take away the residual pump beam $E_{ghost}(t)$ so that we can get a pure SC beam, a harmonic separator HS_{1030} (1 mm fused silica, 0° incident angle, EKSMA Optics) is also used to block the beam $E_{ghost}(t)$ ($\lambda_0 = 1028\ nm$) and to transmit the generated SC.
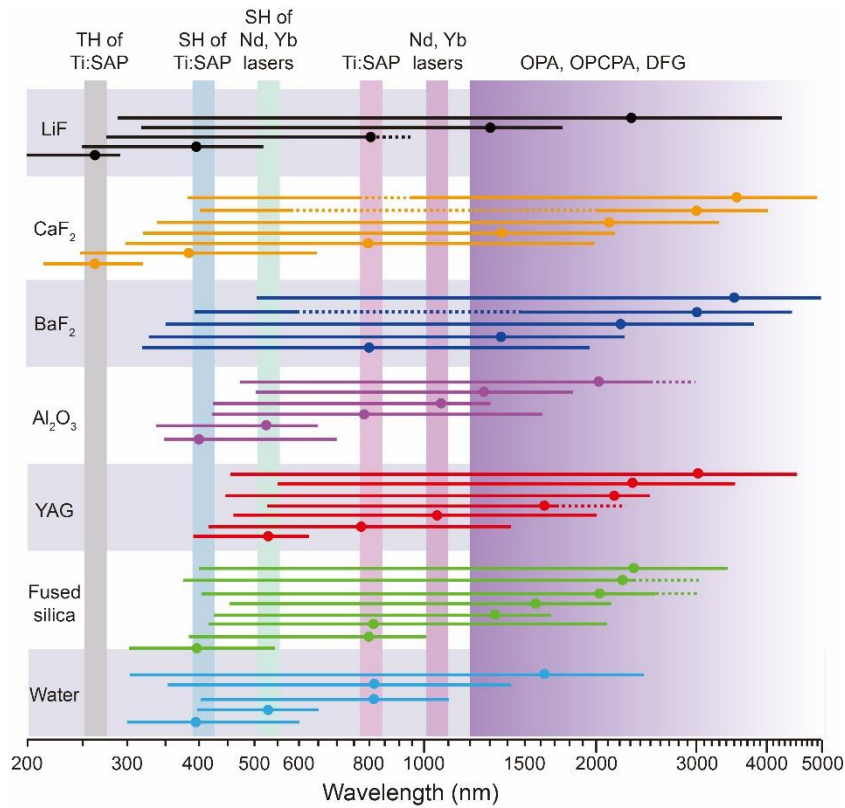
Figure 3.19: Summary of SC spectra generated by different media and different pump wavelengths. In this work, YAG and sapphire crystals are used for performing SC generation by ghost pulse. Data are from [19].

Table 3.3 The GVD coefficients and refractive indexes of YAG and sapphire at 1028 nm pump wavelength.

	λ (nm)	GVD (fs²/mm)	n_0	n_2 (10^{-16} cm²/W)
YAG	1028	66.92	1.81	6.5
Sapphire	1028	32.41	1.75	3.06
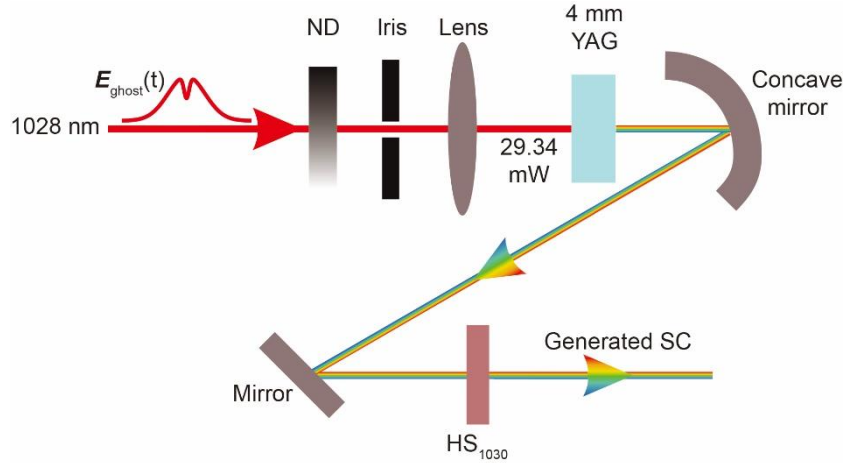
Figure 3.20: Schematic drawing of the SC generation setup used in this work: the ghost pulse $E_{ghost}(t)$ is transmitted through a neutral density filter and an iris, and then is focused into a 4 mm YAG crystal. The generated SC is collimated by a concave mirror (f = 100 mm). The residual driving beam $E_{ghost}(t)$ is blocked by a harmonic separator HS_{1030} to have pure SC pulse at the output. ND - variable neutral density filter; HS_{1030} (1 mm fused silica, 0° incident angle, EKSMA Optics) is a harmonic separator for 1030 nm.
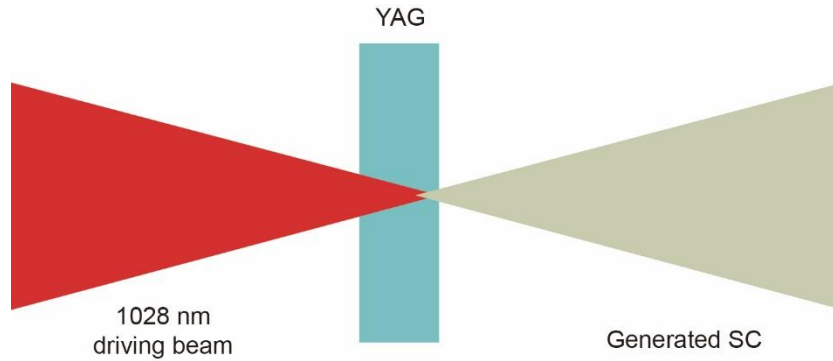
Figure 3.21: A diagram indicating that, in order to minimize GVD effect of a crystal, the focus of driving beam should be as close to the exit side of the YAG crystal as possible.

As mentioned in Section 2.5.2, the critical peak power for self-focusing can be calculated by [104, 107]:

$$P_{cr} = \frac{3.72\lambda_0^2}{8\pi n_0 n_2}.$$

Considering the refractive indexes of YAG and sapphire at 1028 nm pump wavelength shown in table 3.3, we can know the critical peak powers P_{cr} are 1.35 MW for YAG, and 2.99 MW for sapphire, respectively. In our experiment, the powers before YAG and sapphire crystals are about 30 mW and 27 mW, respectively. As shown in Fig. 3.14, the pulse duration is about 2.1 ps. Therefore, for the YAG crystal the peak power is around 7 MW which is about

4 times higher than the critical peak powers P_{cr}. For the sapphire crystal the peak power is 6.4 MW and this is about one time higher than the P_{cr}. Typically, a ratio of $\frac{peak\ power}{P_{cr}}$ is experimentally of the order of ~1-5 for SC generation in bulk [156, 157]. Therefore, the laser powers measured experimentally match the theoretical estimations well.

Fig. 3.22 are two photographs of SC generation phenomena. When we focus the ghost pulse into the YAG crystal, it is easy to trigger the SC generation and we can observe the SC filament inside the crystal by eye. For example, if we focus the driving beam in the center of the YAG crystal, the SC is generated at the center position. For this case the SC filament length is about a half of the crystal thickness, as shown in Fig. 3.22(a). As we shift the focus position of the driving beam, the SC generation position is also shifted. As shown in Fig. 3.22(b), the length of the SC filament is about 1/3 of the thickness of the YAG crystal. As we have mentioned above, for minimizing GVD effect, it is better to focus the driving pulse as close possible to the exit side of the YAG crystal. We can observe the SC spot with a white paper.
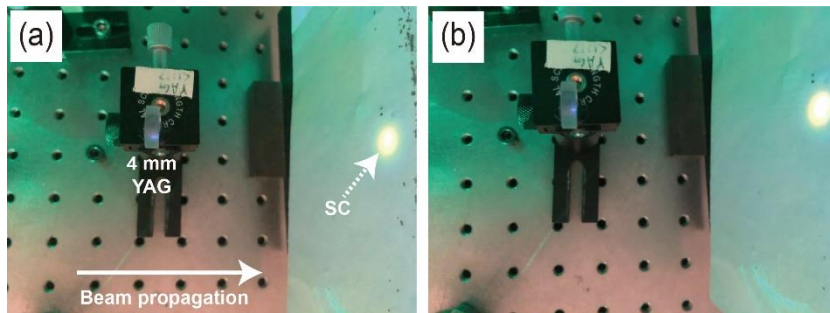
Figure 3.22: Photographs of SC generation in a 4 mm YAG crystal with different filament lengths. (a) The SC filament is about 1/2 of the thickness of the YAG crystal. (b) The SC filament is about 1/3 of the thickness of the YAG crystal. The solid white arrow denotes the direction of the beam propagation. The dot white arrow points to the SC emission spot.

Self-focusing and diffraction in media can also modify pulse shapes in space domain and further affect the spatial SPM. This is analogous to the modification of temporal SPM by self-steepening effect. Consequently, different frequency components diffract into cones with different divergence angles. The generated SC looks like a round disk surrounded by rainbow-like pattern. We call this effect conical emission. Fig. 3.22 shows a photo of our experimentally generated SC with clear conical emission phenomenon.
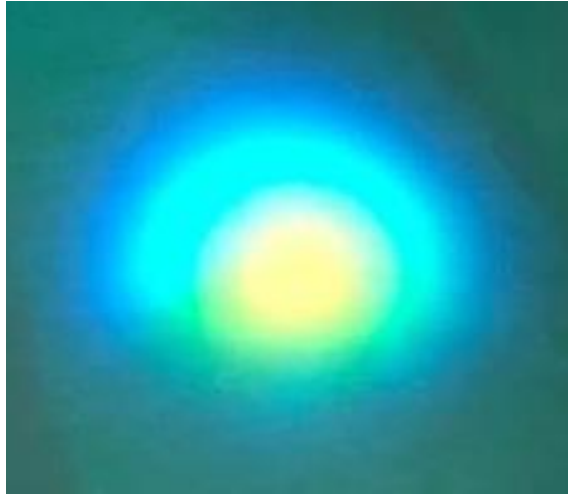
Figure 3.23: Photo of conical emission of SC generated in a YAG crystal (4 mm thickness). Different frequencies diffract into cones with different divergence angles.
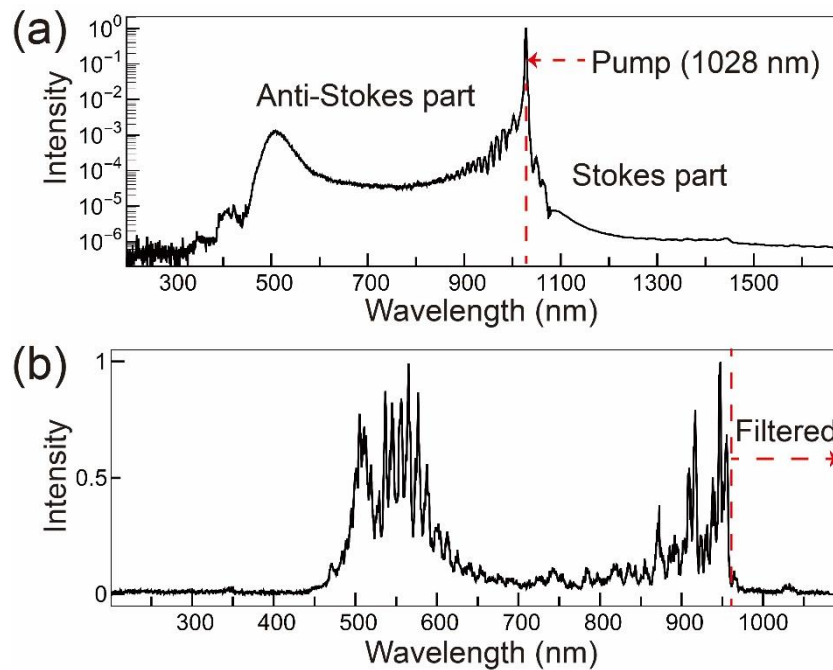
Figure 3.24: The measured spectra of the SC generated by (a) the ghost pulse and (b) the fundamental pulse ($\tau_p \approx 200\,fs$, $\lambda_0 = 1028\,nm$) in a YAG crystal. The result (a) was measured without the harmonic separator HS_{1030}, while the result (b) was obtained with the harmonic separator HS_{1030}.

The spectrum of SC generated by ghost pulse was measured by a commercial spectrometer (Ocean Optics, HR 2000) and shown in Fig. 3.24(a). The Stokes and anti-Stokes parts are asymmetric. Moreover, there exist many small peaks due to the interference effect. Here, we also did a control experiment generating SC using the fundamental laser pulse ($\tau_p \approx 200\,fs$,

$\lambda_0 = 1028\,nm$). Fig. 3.24(b) shows the spectrum of SC generated by the fundamental laser pulse. The interferometric coherent structure is very strong in the case of effective SC generation. The possible reason is that the normal Gaussian driving beam gives rise to multi-filaments which further interference each other. If we decrease the laser power of the pump pulse drastically, the spectral structure of the generated SC can become much smoother. However, in this situation the low laser power cannot generate a stable SC anymore. Therefore, ghost pulse is much better than Gaussian pulse for a stable SC generation with smooth spectral profile.

Our XFROG setup shown in Fig. 3.3 is also used to characterize the SC generated by ghost pulse. Fig. 3.25 presents the XFROG result. In order to prove that the SC is really generated at ghost position, we moved away the harmonic separator HS_{1030} and thus the XFROG result can characterize the pulse $E_{ghost}(t)$ and the generated SC $E_{SC}(t)$ together. As shown in Fig. 3.25, it is clear that the spectral broadening only appears at the ghost pulse position.
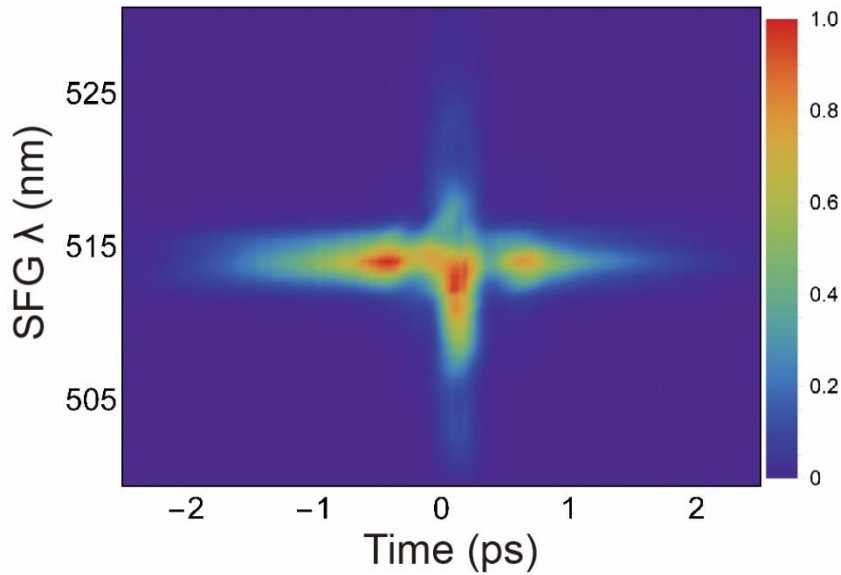
Figure 3.25: XFROG result of newly generated SC $E_{SC}(t)$ together with the ghost pulse $E_{ghost}(t)$ demonstrating that the SC is only generated by the ghost pulse.

XFROG setup is also used to characterize the SC generated by the fundamental pulse ($\tau_p \approx 200\,fs$, $\lambda_0 = 1028\,nm$). Fig. 3.26(a) presents the XFROG results of the short fundamental pulse $E(t)$, while Fig. 3.26(b) shows the XFROG results of the short fundamental pulse $E(t)$ together with the generated SC $E_{SC}(t)$. From Fig. 3.26 we can find that the SC is obviously positively chirped and matches the theoretical calculation (see Fig. 2.20(c)).
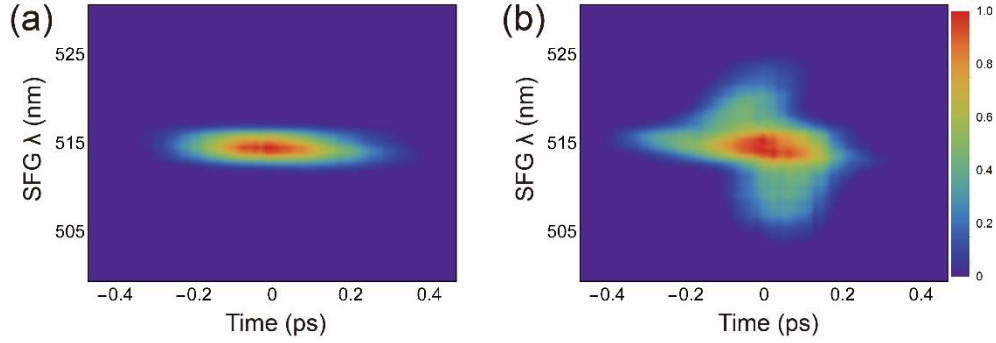
Figure 3.26: (a) XFROG result of the 200 fs 1028 nm fundamental pulse $E(t)$; (b) XFROG result of the 200 fs 1028 nm fundamental pulse $E(t)$ together with the generated SC beam $E_{SC}(t)$, presenting that the newly SC is positively chirped which matches the theoretical calculation.

Comparing Figs. 3.25 and 3.26, it is clear that the SC generated by ghost pulse and by fundamental pulse are different. The SC generated by the 200 fs fundamental pulse is obviously positively chirped (Fig. 3.26(b)). However, from Fig. 3.25 the generated SC by ghost pulse does not present significant negative chirp. It shows nearly zero chirp. This result does not agree with our expectation that it should show clear negative chirp. The possible reasons are the YAG crystal is too thick and the GVD coefficient of YAG (66.92 fs^2/mm) is rather high. The negative chirp of the SC generated by the ghost pulse has been compensated by the GVD effect.
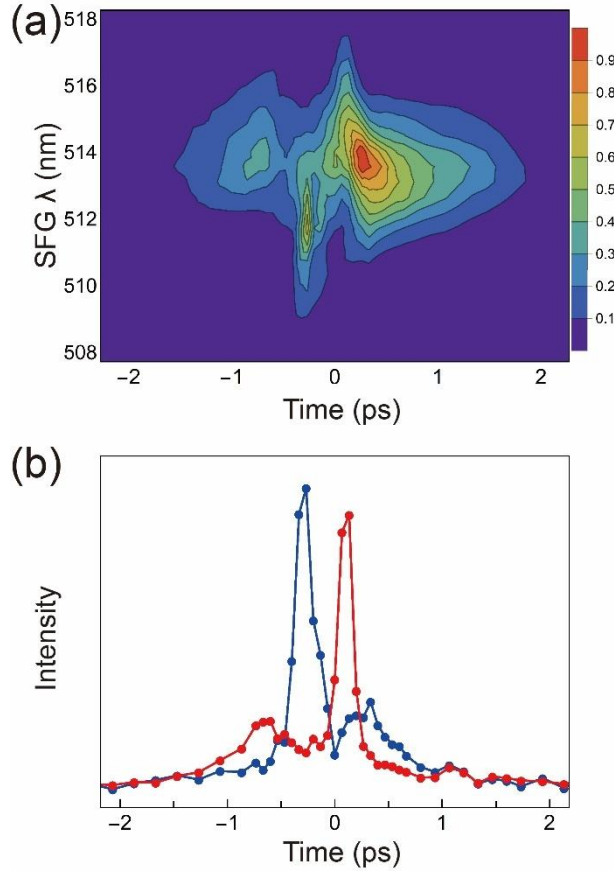
Figure 3.27: SC generation by ghost pulse in a 1 mm sapphire crystal. (a) XFROG result of the negatively chirped SC generated by ghost pulse. (b) Comparing the red-shifted and blue-shifted components in time domain, further showing that the blue-shifted light comes before the red-shifted light.

For proving our assumption, the 4 mm YAG crystal was exchanged by a 1 mm thin sapphire crystal. Comparing with YAG medium, sapphire has much lower GVD coefficient (32.41 fs^2/mm) what is beneficial to keeping the SC negatively chirped. As shown in Fig. 3.27(a), the XFROG result suggests that the SC generated in a 1 mm sapphire demonstrates clear negative chirp, i.e. the shorter wavelength at 510 nm appear before the longer wavelength at 515 nm. Further, we compare the sum intensity of red-shifted ($\lambda > 515$ nm) and blue-shifted ($\lambda < 511.6$ nm) wavelengths, as shown in Fig. 3.27(b). Obviously, the blue-shifted wavelengths appear earlier than the red-shifted wavelengths. This proves that the SC generated by the ghost pulse is negatively chirped.

In Fig. 3.4, another experimental setup is shown for negatively chirped SC generation by ghost pulse. In this setup, the ghost pulse $E_{ghost}(t)$ is produced by the SFG process between $E_{4f}(t)$ and second harmonic $E_{SHG}(t)$ pulses. The generated SC is studied by a NOPA-technique. On one hand, the NOPA setup can be regarded as a practical application of the negatively chirped SC generated by ghost pulse. On the other hand, the NOPA technique can be a good approach to test the negatively chirped SC generated by ghost pulse. Moreover, the generated SC is rather weak and thereby it is not easy to

be characterized directly. A NOPA setup can amplify the SC for the further study. The pulse duration of NOPA output can be easily measured by a commercial autocorrelator.

Fig. 3.28 presents the NOPA setup built by us for the characterization of the generated SC. In this NOPA, the generated SC $E_{SC}(t)$ acting as the seed beam is focused into a BBO crystal (type I, 1 mm thickness, $\theta = 23.4°$) by a concave mirror ($f = 100$ mm). The second harmonic 514 nm beam $E_{SHG}(t)$ is focused into the same BBO crystal by a lens ($f = 300$ mm) and serves as the pump beam of NOPA. A hand-tuned optical delay stage varies the time delay between the pump and seed beams in the BBO crystal. The amplified signal is monitored by a spectrometer.
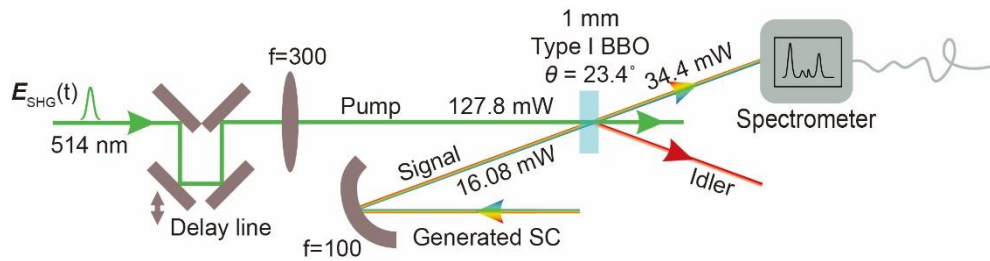
Figure 3.28: Scheme of the NOPA setup: the second harmonic pulse $E_{SHG}(t)$ and the generated SC $E_{SC}(t)$ are focused into a BBO crystal (type I, 1 mm, $\theta = 23.4°$) by a lens ($f = 300$ mm) and a concave mirror ($f = 100$ mm), respectively. A delay line is inserted in the second harmonic beam for adjusting the temporal overlap of the two beams in the BBO crystal. A spectrometer is used to register the NOPA output.

If the NOPA setup is well aligned, we should be able to observe the phenomenon as shown in Fig. 3.29. Bright central spot denotes the pump beam $E_{SHG}(t)$. Right side spot is the amplified signal $E_{SC}(t)$, while the idler beam appears on the left side.

As we have discussed in section 2.4, in the process of non-collinear optical parametric amplification, the beams should meet the phase matching condition:

$$\Delta \vec{k} = \vec{k}_{pump} - \vec{k}_{idler} - \vec{k}_{signal} = 0,$$

where $\vec{k}$ denote wave vectors and signal is our SC seed.

Different frequency components in seed beam can be amplified in NOPA and the $\vec{k}$ vectors of the newly produced idler components have different directions to fulfill the phase matching condition. Thusly, as shown in Fig. 3.29 the idler beam spreads like a colorful line in space.
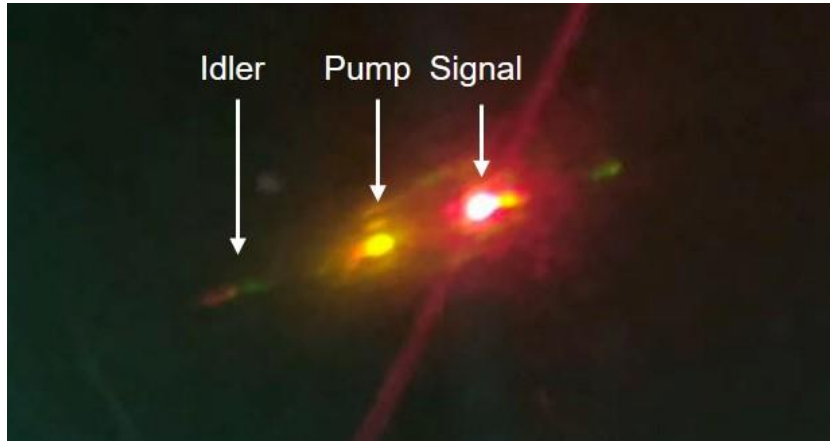
Figure 3.29: Photograph of NOPA phenomenon. Bright central spot and the right spot are the pump and the amplified signal beams, respectively. The left colorful line denotes the produced idler beam.

Fig. 3.30(a) shows the output spectrum of the NOPA seeded with the SC generated by the ghost pulse. The phase matching condition is satisfied over a broad spectral range and the light at the corresponding frequencies is amplified. Fig. 3.30(b) is the output spectrum of NOPA seeded with the SC generated by fundamental pulse ($\tau_p \approx 200\ fs$, $\lambda_0 = 1028\ nm$). From these (a) and (b) figures we can see that the NOPA has rather broad amplification. However, we find there are some differences when we align the NOPA setup. If the NOPA is seeded by the SC generated by the ghost pulse, it is easy to amplify a very broad spectral range covering 650-930 nm (about 4600 cm^{-1}). If it is seeded by the SC generated by 200 fs fundamental pulse, it is difficult to amplify the whole range of 650-980 nm. From this experimental result, it can be deduced that the temporal overlapping between the pump and SC generated by the ghost pulse is easier. A possible reason is that the SC generated by ghost pulse is shorter than the pump pulse. According to this experimental result, we can assume that the SC generated by the ghost pulse could be negatively chirped and further compressed in optical elements with positive GVD. This property can be used for generating short pulses from the NOPA or for expanding the usable spectral range up to about 4600 cm^{-1} in FSRS (femtosecond stimulated Raman spectroscopy) experiments.
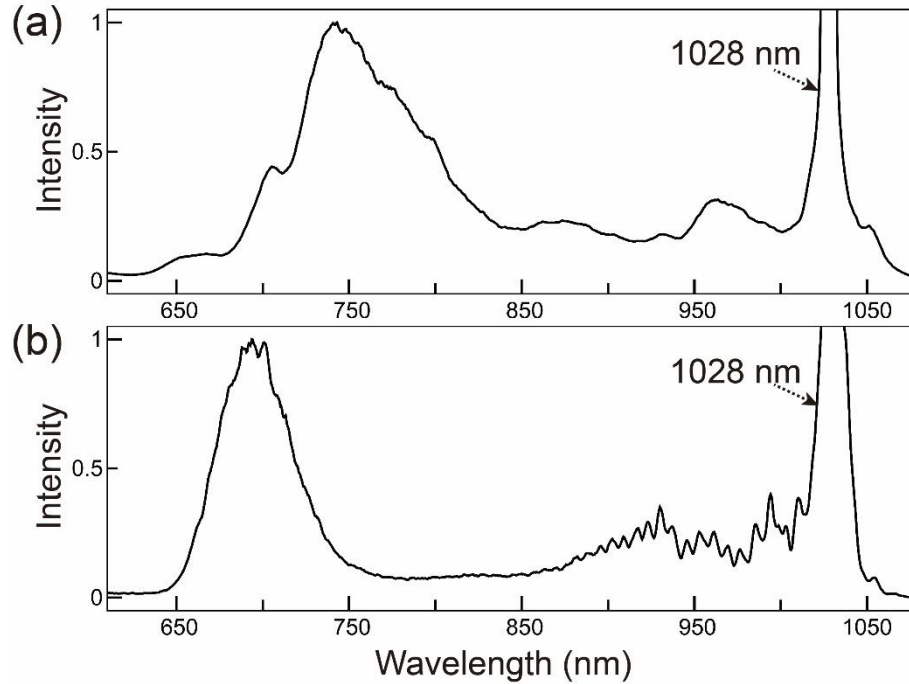
Figure 3.30: The output spectra of NOPA seeded by different SC (a) generated by the ghost pulse, (b) generated by the 200 fs 1028 nm fundamental pulse $E(t)$. The dot arrows point to the fundamental driving wavelength.
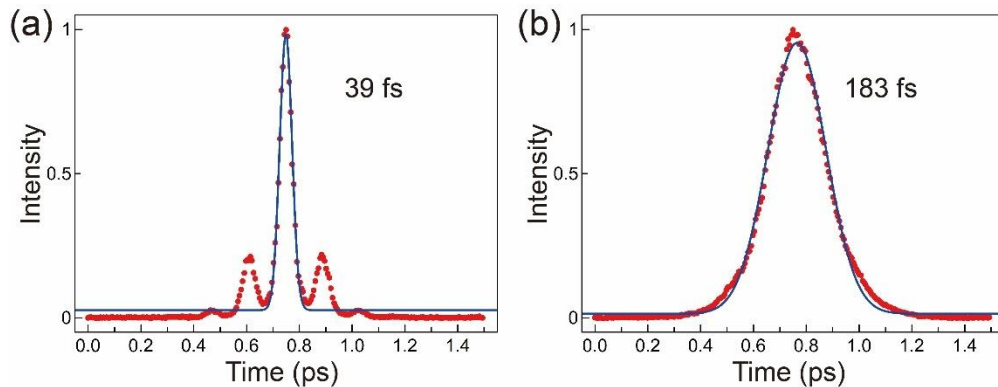
Figure 3.31: The autocorrelation curves of the outputs of NOPA seeded with different SC as signal: (a) SC generated by the ghost pulse, (b) SC generated by the 200 fs fundamental pulse $E(t)$. The red dots denote the measured data. The solid blue line represents the Gaussian fitting curve.

The autocorrelation curves of the NOPA output are also measured using a commercial autocorrelator. As shown in Fig. 3.31(a), when NOPA is seeded with the SC generated by the ghost pulse, the autocorrelation curve of NOPA output shows about 40 fs pulse length. If we use the SC generated by the 200 fs 1028 nm fundamental pulse as the signal beam for NOPA, the duration of NOPA output is about 184 fs (Fig. 3.31(b)). Because in these two different cases, the pump beams are the same and thus the different pulse durations of the NOPA output should result from the different signal seed beams. For the

case shown in Fig. 3.31(a), the seed SC pulse generated by the ghost pulse must be very short, otherwise we should not obtain such short NOPA output. Combining the XFROG results (see Figs. 3.26 and 3.27), it can be deduced that the generated SC is negatively chirped and afterwards the chirp is compensated in the optical elements, such as YAG, sapphire and BBO crystals. When the SC arrives to the NOPA's BBO crystal, the negative chirp of the SC pulse could be good compensated and be shorter than the SC generated by the fundamental pulse. This could explain short (39 fs) NOPA output.

3.4 Summary

This chapter is mainly devoted to the description of the negatively chirped SC generation by the ghost pulse. We present the details of the experimental setups, as well as analyze and discuss the experimental results. According to the SPM theory, a ghost pulse should be able to generate a negatively chirped SC. Motivated by this idea, specific experimental setups including several key units such as 4f-line, SFG setup, SC generation and characterization setups were built. The 4f-line and SFG setup are used to create the desired ghost pulse. The formation of the ghost pulse was verified by a home-built FROG setup and a commercial autocorrelator device. Afterwards, the ghost pulse is focused into a YAG/sapphire crystal to produce negatively chirped SC. Finally, the NOPA and XFROG techniques are used to characterize the negatively chirped SC. From the NOPA result, we can deduce that the SC generated by ghost pulse should be negatively chirped. The XFROG result gives more convinced proofs. It verifies that the SC can be generated by the ghost pulse because the spectral broadening appears just at the position of the ghost pulse. It also proves that the generated SC in 1 mm sapphire by the ghost pulse is negatively chirped.

Chapter 4

Two-stage non-collinear optical parametric amplifier

In this chapter, a two-stage non-collinear optical parametric amplifier (NOPA) pumped by the second harmonic (λ_0 = 514 nm) of Yb:KGW laser light is described. The NOPA output tuned from 650 to 1000 nm. Pulse compression of the NOPA output is performed using an Acousto-Optic Programmable Dispersive Filter (AOPDF).

4.1 Introduction

Ultrafast optics has become a major technology in many modern studies of light-matter interaction [54, 63]. It is necessary to develop applicable laser sources which can supply pulse with ultrashort duration, high peak power and broad frequency bandwidth. For example, in the field of pump-probe spectroscopy, the research objects (atom, molecule, etc.) are excited by a "pump" pulse and then the sample's subsequent evolution is monitored by observing the pump-induced absorption change which is measured by a delayed "probe" pulse [38]. For investigating some fast-physical process, the probe pulse should have a very high temporal resolution which means the duration time of probe pulse should be very short. Moreover, different study samples require variable beam powers and frequencies of both pump and probe pulses. Hence, for a long time the generation of a tunable ultrashort pulse is one of the major challenges in the field of ultrafast optics.

Basing on Ti:sapphire and Yb:doped gain media, Kerr-lens mode-locking and chirped-pulse amplification (CPA), rugged, reliable and power scalable sources of ultrafast pulses have been developed [65-68]. Up to now, this technology is still the mainstream method to generate ultrashort pulse. However, such kind of laser source can not supply tunable output radiation and is limited in a narrow range around the fundamental frequencies (1040 nm for Yb and 800 nm for Ti:sapphire).

In most cases, optical parametric amplifier (OPA) using nonlinear optical effect can achieve frequency tunability. Up to now, OPA has become a standard tool for the generation of ultrashort pulses over the spectral range from UV to IR [93-100]. Non-collinear OPA, namely NOPA, is able to achieve phase matching conditions over a broad frequency range and thus an ultrabroad amplification output can be obtained. In order to get ultrashort pulses,

generally the NOPA output should be compressed. Traditional methods for pulse compression are based on pairs of prisms/gratings [158-160], or SLM [161-173] placed in the Fourier plane of a 4f-line configuration. Many valuable studies have been reported with such devices [158-173]. However, these traditional setups for pulse compression are rather complex and achievable tunability is limited. In 1997, P. Tournois proposed a device, namely Acousto-Optic Programmable Dispersive Filter (AOPDF) [174], which can compress pulses in large dispersion-compensation ranges. AOPDF is an easy applicable device.

In this chapter, firstly the basic concepts of AOPDF are described. Then the build of two-stage NOPA and the experimental results are present and discussed.

4.2 Acousto-optic programmable dispersive filter
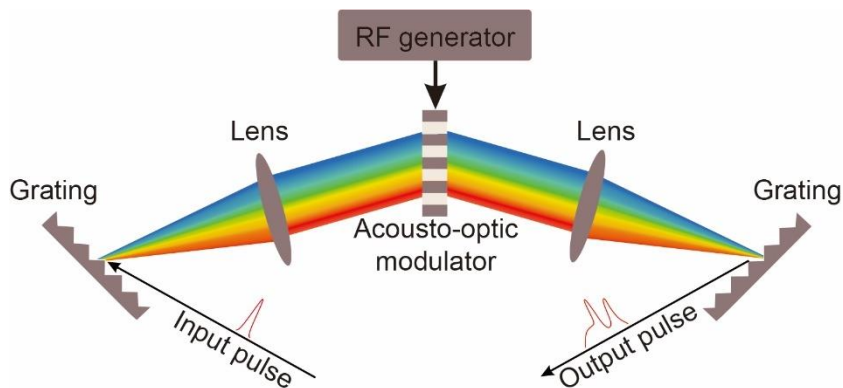
Figure 4.1: Scheme of a pulse shaping setup using an AO modulator. The construction structure of the setup is based on a 4f-line. Inside the AO modulator, the acoustic wave shapes the incoming optical wave. This interaction process is similar to the Bragg diffraction.

AOPDF is a device which enables independent phase and amplitude control over each pulse [51, 174-178]. In an AOPDF, a radio-frequency (RF) generator produces an electrical RF signal which then drives a piezoelectric transducer. Afterwards the transducer launches a traveling acoustic wave into an appropriate crystal. The acoustic wave induces changes of the refractive index of the crystal and thus the diffraction angles of the light beam have been changed. Modulator action is based on this principle. Therefore, when we modulate the amplitude and phase of the electrical RF signal, the amplitude and phase of the diffracted beam should be shaped. As shown in Fig. 4.1, the pulse shaping setup using an acousto-optic (AO) modulator is similar to the 4f-line system shown in Fig. 3.9(a), but with the lenses and gratings displaced to account for the beam deflection angles that accompanies AO modulation. In this setup we can use the RF generator to produce arbitrary electronic waveforms to drive the modulator so that the profile of the output pulse can be

controlled.

Dazzler is the commercial name of AOPDF which is produced by Fastlite [179]. As shown in Fig. 4.2, it is mainly composed of three parts: an acousto-optic crystal unit, an RF generator and a corresponding Laptop. In this study, a Dazzler designed for working in the spectral range of 510-900 nm is used to compress the NOPA output pulse.
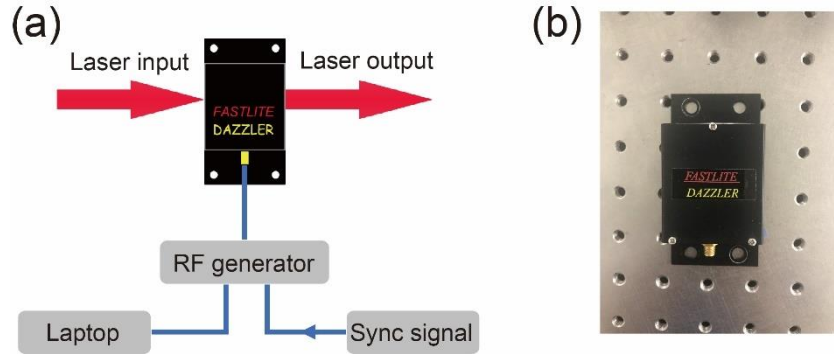
Figure 4.2: (a) System components of a Dazzler device and (b) a photo of the crystal unit of the Dazzler used in our study.

The AOPDF device can be manufactured using various crystals, such as $LiNbO_3$, $PbMoO_4$, or TeO_2. As shown in Fig. 4.3, the commercial Dazzler adopts a 25 mm long TeO_2 crystal as the active component for the acousto-optic interaction. The acoustic wave is launched by a piezoelectric transducer. The incident ordinary optical wave propagates collinearly with the acoustic waves inside the TeO_2 crystal. The anisotropic interaction between them leads to diffraction of an extraordinary wave (Fig. 4.4). Therefore, pulse shaping in spectral amplitude and phase can be realized by controlling the optical path of extraordinary propagation of spectral components. The maximum achievable group delay is determined by the crystal length, e.g. ~3 ps for 25 mm long TeO_2 crystal.
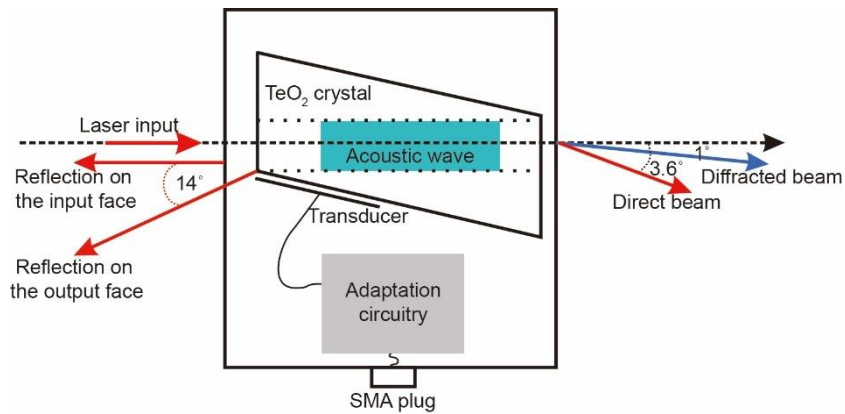
Figure 4.3: Top view of the Dazzler model. A TeO_2 crystal is used as the host medium. The input laser is shaped by the acoustic wave.
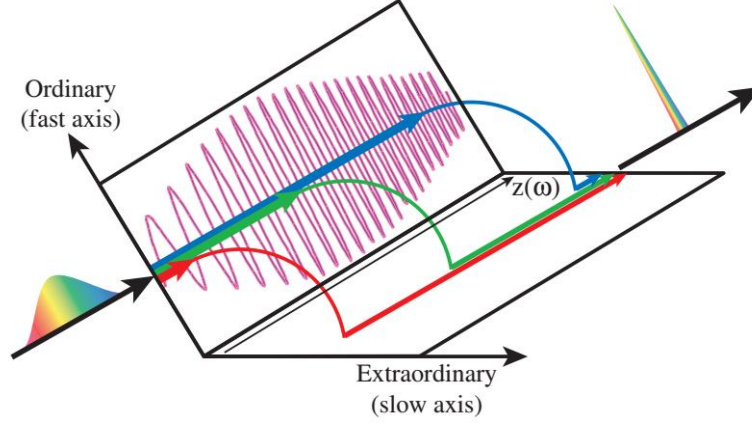
Figure 4.4: AOPDF principle. By acoustic grating diffraction, different spectral components are converted from ordinary axis to extraordinary axis at different positions in the TeO$_2$ crystal. The figure is reprinted from Ref. [180].

Inside the TeO$_2$ crystal with a propagating acoustic wave, the optical beam experiences Bragg diffraction. As shown in Fig. 4.4, consider a collinear acousto-optic interaction in the direction of z axis in an anisotropic photoelastic medium. The nonlinear acousto-electric interaction is given as [174]:

$$E_{out}(\omega_{out})e^{i(\omega_{out}t-\mathbf{k}_{out}z)} = E_{in}(\omega_{in})e^{i(\omega_{in}t-\mathbf{k}_{in}z)} \times S_{ac}(\omega_{ac})e^{i(\omega_{ac}t-\mathbf{k}_{ac}z)},$$
(4.1)

where $E_{out}(\omega_{out})$, $E_{in}(\omega_{in})$ and $S_{ac}(\omega_{ac})$ respectively denote the complex spectral amplitudes of the diffracted optical signal, the incident optical signal and the acoustic signal; ω_{out}, ω_{in} and ω_{ac} respectively represent the frequencies of the diffracted optical signal, the incident optical signal and the acoustic signal; $\mathbf{k}_{out}$, $\mathbf{k}_{in}$ and $\mathbf{k}_{ac}$ are the wavenumbers of the diffracted optical signal, the incident optical signal and the acoustic signal.

The incident optical beam transfers energy to the diffracted optical beam only with satisfying the phase matching conditions:

$$\begin{aligned} \omega_{out} &= \omega_{in} + \omega_{ac} \\ \mathbf{k}_{out} &= \mathbf{k}_{in} + \mathbf{k}_{ac} \end{aligned}.$$
(4.2)

The working time window of AOPDF is [180]:

$$T_{max} = \delta n_g(\lambda_0)cos^2(\theta_{in})\frac{L}{c}, \quad (4.3),$$

where $\delta n_g(\lambda_0) = n_{g,e}(\lambda_0) - n_{g,0}(\lambda_0)$ (4.4)

is the group index difference, λ_0 - the center wavelength of the incoming beam, L - the TeO$_2$ crystal length, c - the light velocity, and θ_{in} - the angle between a reference crystallographic axis and the incident wave vector.

The pulse shaping resolution in frequency can be calculated by [180]:

$$\delta\lambda = \frac{0.8\lambda^2}{\delta ncos^2(\theta_{in})L}. \quad (4.5)$$

The RF generator in Fig. 4.2 is interfaced with a Laptop and is controlled by a commercial software (Fig. 4.5) from Fastlite. Using this software one can

program the acoustic wave conveniently. The RF generator can be triggered by an internal digital signal or by an externally synchronized signal from the laser system. The delay time between the RF generator and the trigger signal can also be programmed. For a laser system output pulse at repetition rate 2 kHz, the RF generator is triggered every 500 μs. The acoustic signal needs 25 μs to travel through the 25 mm TeO_2 crystal and thus the maximum repetition rate supported by Dazzler is 40 kHz.
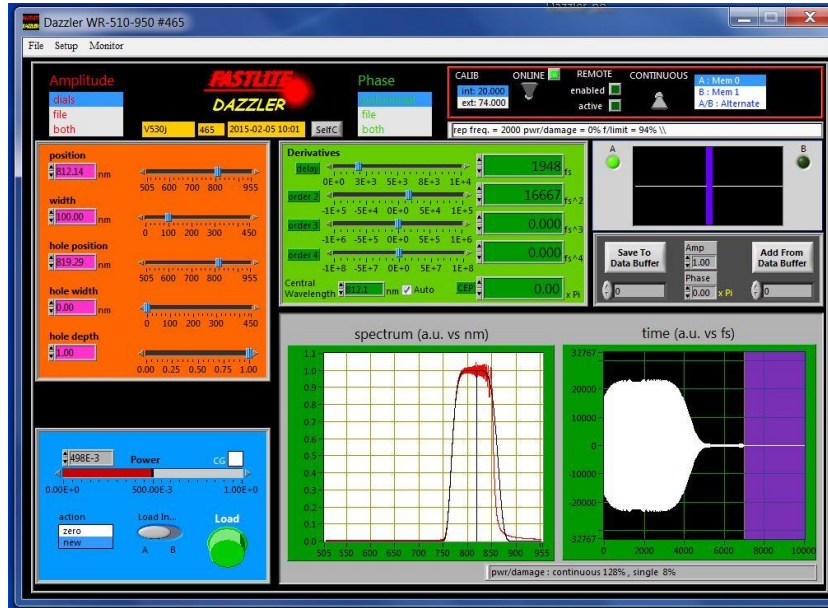
Figure 4.5: GUI view of the commercial Dazzler software which provides flexible controlling of key parameters.

4.3 Experimental setup of two-stage NOPA

4.3.1 Overview of the setup

Figure 4.6: Simple scheme of the setup of a two-stage NOPA using a Dazzler for the output compression. The laser pulses are delivered to the two-stage NOPA system and the NOPA output is compressed by Dazzler device and characterized by an autocorrelator.

AOPDF is generally used as a convenient device to shape spectral amplitude and phase of optical waves [51, 174-178]. For example, in an ultrafast CPA laser system the AOPDF can be inserted between the stretcher and the amplifier to avoid gain narrowing and get a smooth spectral shape. AOPDF can also be used to produce two or more separated pulses in time. In

this work, Dazzler is used as a pulse compressor at the output of a two-stage NOPA. Fig. 4.6 shows the setup scheme. The layout of the two-stage femtosecond NOPA is presented in Fig. 4.7.
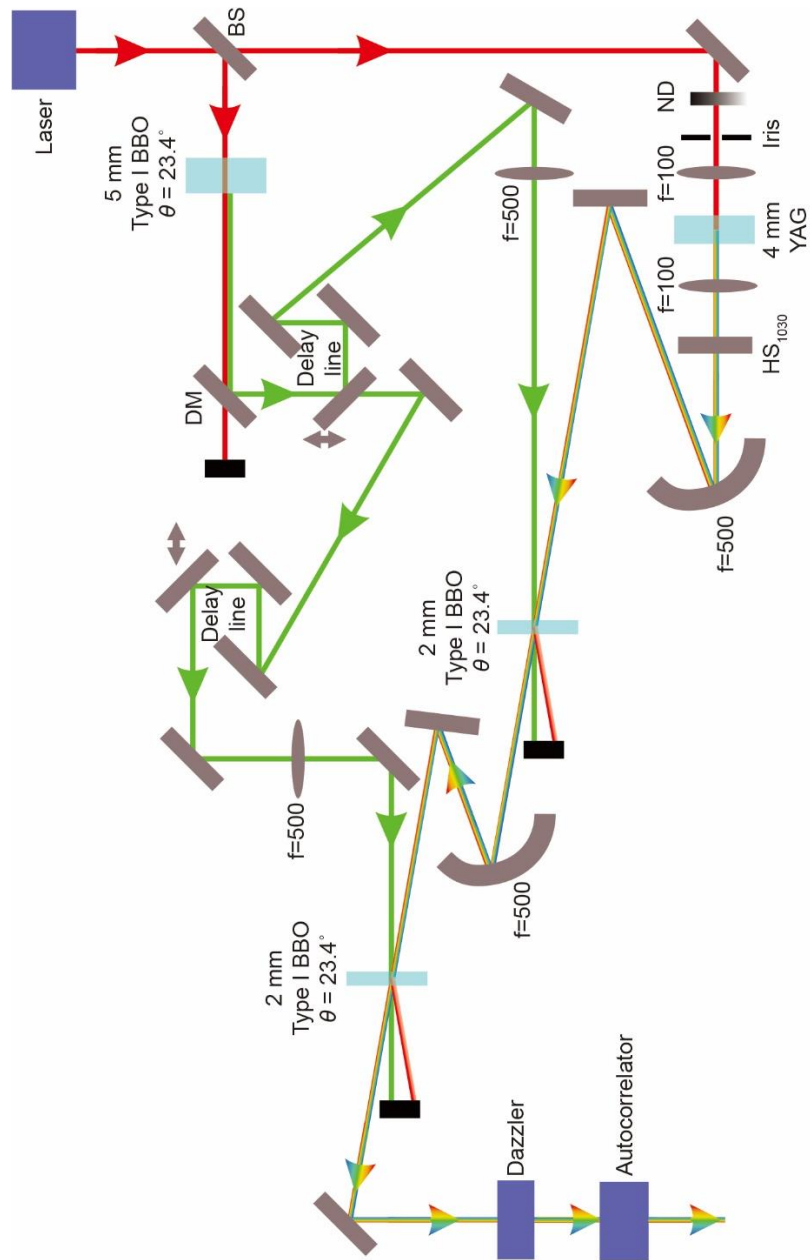
Figure 4.7: Optical layout of the setup: The main part of this setup is the two-stage NOPA, and its output is compressed by a Dazzler device; then the pulse duration is characterized by an autocorrelator. The red line denotes the fundamental laser ($\lambda_0 = 1028\ nm$) light. The green line denotes the second harmonic ($\lambda_0 = 514\ nm$) of fundamental laser light and this beam acts as the pump beam in the NOPA. The multi-color line denotes the signal beam which covers a broad spectral range. BS is beam splitter; DM - dichroic mirror; ND - neutral density filter; HS_{1030} (1 mm fused silica, 0° incident angle, EKSMA Optics) is a harmonic separator for 1030 nm.

The start beam is supplied by an ultrafast Yb:KGW laser system with output wavelength of 1028 $\pm$ 4 nm, 2 kHz repetition rate, 2000 mW average power, vertical polarization and ~200 fs duration time. This fundamental beam is split by a beam splitter (R:T = 90:10). The reflected 1800 mW power light is used to produce the second harmonic green pump pulse for the NOPA, while the transmitted 200 mW power is used to generate the SC seed pulse. Here we do not focus the fundamental beam into the BBO crystal to achieve higher second harmonic generation ratio. Depending on the actual situation, Galilean telescope arrangement with different focal lengths of the lenses can be used here for obtaining more pump power for NOPA. A type I BBO crystal (5 mm thick, θ = 23.4°) is used for SHG process and it can yield a SHG efficiency ~16% and good quality spatial mode of the beam. The SHG green pulse is reflected by a dichroic mirror (HR 532, HT 1064) to a delay line. The left mirror of the delay line as shown in Fig. 4.7 is replaced by a beam splitter (R:T = 35:65). Therefore, this beam splitter is used to split the pump at 514 nm into two beams at ratio 35:65. The reflected 35% SHG pump is used to perform the 1st amplification process while the remaining transmitted 65% of the SHG are used for the 2nd stage of non-collinear amplification.

The 10% transmitted beam of the fundamental laser is used to generate the SC to be the seed signal for the NOPA. A convex lens (f = 100 mm) is used to focus 200 mW fundamental pulse into a 4 mm thick YAG crystal to perform SC generation. The strong SC with good spatial quality looks uniform. For obtaining a good SC beam, an iris is also inserted to control the fundamental beam size so that only the center uniform beam is used to perform SC generation, and a variable attenuator is also added to reduce the intensity at the YAG crystal until a uniform SC mode is observed. A lens with focal length f = 100 mm is used to collimate the generated SC. A dichroic harmonic separator (HS$_{1030}$, Femtoline Laser Harmonic Separator, R > 99.5% at 1030 nm, EKSMA Optics) is used to remove the residual fundamental laser light. As shown in Fig. 4.7, the generated SC is focused by a concave mirror (f = 500 mm) a few millimeters behind a 2 mm thick, type I BBO crystal cut at θ = 23.4°. The 1st stage non-collinear parametric amplification is carried out in this type I BBO crystal. The 2nd stage amplification setup is similar to the 1st stage. The 65% SHG beam goes through a delay line and then is focused in a second type I BBO crystal (2 mm thick, θ = 23.4°) using a convex lens (f = 500 mm). The output of the 1st stage NOPA is focused in the same BBO crystal by a concave mirror (f = 500 mm) as the signal beam for the 2nd stage of the NOPA. The NOPA's output is compressed by the Dazzler device.

4.3.2 Signal and pump beams for NOPA

In our NOPA system, the SC is used as the seed pulse. As shown in Fig. 4.7, SC generation is realized by focusing a small fraction of the fundamental pulse (λ_0 = 1028 nm) into a plate. Here we use a YAG plate with thickness of

4 mm. We can adjust the pulse energy by a neutral density filter, the focusing conditions by shifting the position of the plate slightly and the spot size of the focused beam by placing an iris, until a good single SC filament is obtained.

Fig. 3.5 shows the spectra of the driving beam ($\lambda = 1028 \pm 4\,nm$) for the SC generation. Using this 1028 nm Yb-based driving pulses, some media with lower bandgap allows the generation of stable SC. In particular, for the driving light at 200 – 400 fs pulse duration typically provided by Yb-based lasers, a 4 – 6 mm thick YAG plate is a suitable choice which allows stable SC generation without any damages of the plate. A very broadband seed is provided using the SC generated in YAG plate. The duration of the NOPA output pulses is determined by the temporal length of the amplified broad bandwidth.

The spectrum of generated SC is shown in Fig. 4.8. We can observe that at the position of the driving pulse wavelength there is an intense residual peak. This suggests the driving beam contains most of the energy. Besides this, a broad continuum is formed in range of about 400 – 1000 nm. Here, the measurement range is limited by our spectrometer working range which just covers wavelength range of 178 – 1090 nm. In our experiments, the spectral energy density of the broad continuum is 3 or 4 orders lower than that of the driving pulse. The SC displays diffraction-limited spatial beam quality and very good shot-to-shot stability. Therefore, it is an ideal seed for the NOPA setup.
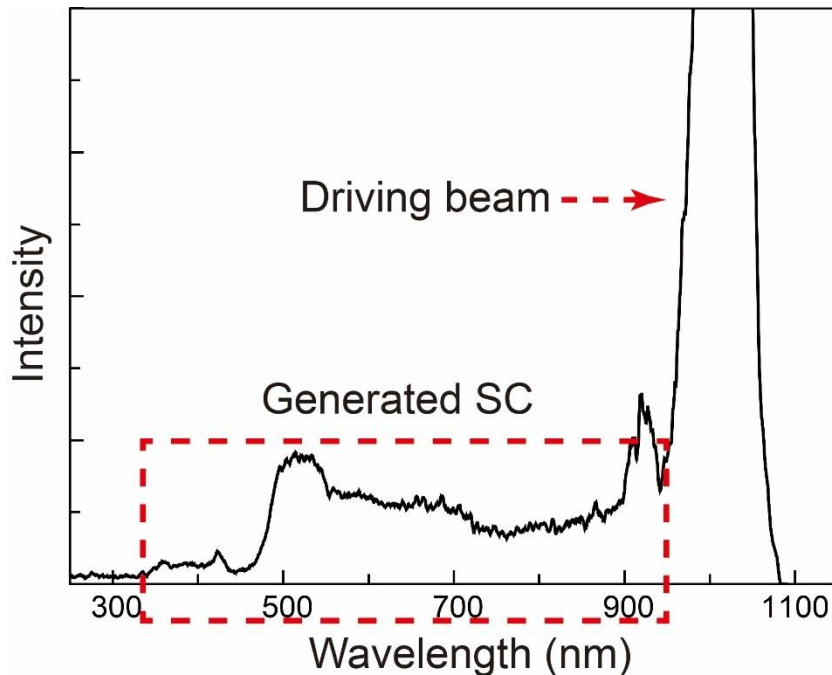
Figure 4.8: A part of the spectrum of the generated SC. The wavelength range longer than 1090 nm is not measured because of the limit of our spectrometer.

In the process of optical parametric amplification, energy transfers from the strong pump beam to the weak signal beam. The characteristics of the

pump pulse is one of the most important parameters which influence the performance of NOPA setup. The pump wavelength affects the spectral tuning range; the pulse duration and energy of pump determine the gain efficient, the interaction length and the obtained energy of the amplified signal; the pump repetition rate decides the average power flowing through the crystals.

In this work, the second harmonic of the Yb:KGW laser acts as the pump beam for the NOPA. Fig. 4.9 shows the pump spectrum. The Broad spectral region of 690 – 960 nm can be well covered by NOPA pumped by the second harmonic of Yb:KGW laser.
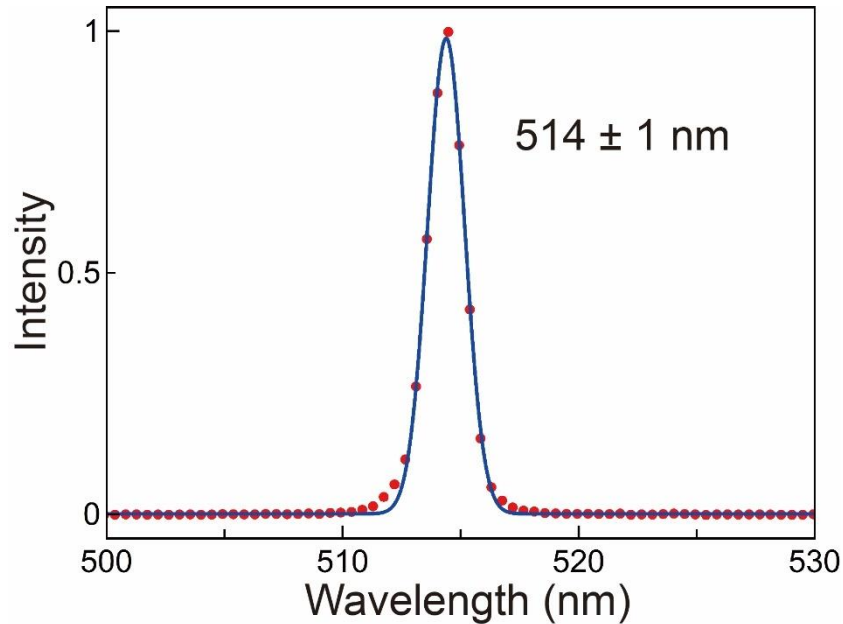
Figure 4.9: Pump spectrum of the NOPA. In this work, the second harmonic of fundamental beam acts as the pump beam for the NOPA. The red dots and the solid blue line denote the experimental measured data and the Gaussian fitting curve, respectively.

4.3.3 Setup details

When we align the NOPA setup, bright superfluorescence rings (emanating as a cone) in the visible can be observed after the NOPA BBO crystal (see Fig. 4.10(a)). Because the polarization of pump beam is horizontally, the BBO crystal should be also oriented horizontally along its optical axis to generate superfluorescence. Once the intensity of pump beam is high enough, it is not difficult to observe the superfluorescence rings. If superfluorescence is not observed, the pump focus can be slightly adjusted and the BBO can be slightly rotated along the vertical axis. If the pump intensity is too high, the NOPA BBO crystal will also generate SC. This should be avoided. We should ensure that the colored rings seen after the NOPA BBO are superfluorescence rings. If the ring diameters change drastically with the rotation of the crystal, it should be the superfluorescence rings. In the case of

the colored rings generated due to supercontinuum, they remain constant under crystal rotation.
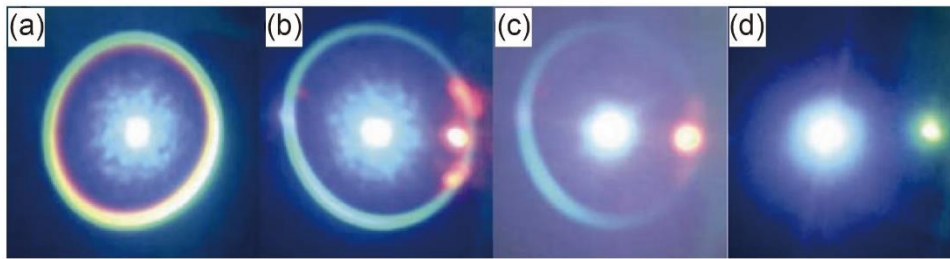
Figure 4.10: Photographs of the output beams after the NOPA BBO crystal pumped at 400 nm under different overlapping conditions. The central and right-side bright spots denote the pump and signal beams, respectively. (a) The pump beam induces multicolored parametric superfluorescence rings. (b) The case that the pump and signal beams do not overlap well. (c) The case that the phase matching is not completed. (d) The case that the phase matching conditions have been satisfied completely. The figure is reprinted from Ref. [181].

The crossing angle is determined by the pump wavelength and the signal wavelengths that we want to amplify. Fig. 2.16 shows the theoretical phase matching angle for NOPA using type I BBO crystal and central pump wavelength of 514 nm. The white light seed and the green pump are crossed at an angle of 2.3°, as can be seen in Fig. 2.16. It is worth noting that, the crossing angle inside crystal is significantly different with the angle outside of the BBO due to the influence of the high index of refraction of BBO.

The internal angle can be calculated based on the pump and signal wavelengths and the phase matching conditions. The external angle is the angle outside of the BBO crystal. When the pump and signal beams enter the crystal, the high refractive index of the BBO crystal bends the beams' path so that the external angle is different with the internal angle. The external angle can be calculated by Snell's Law. At this angle, the white light can be seen along the circumference of the superfluorescence ring and this is a good guiding factor to ensure correct alignment. If the white light is not seen on the circumference of the superfluorescence ring, the amplifier's BBO can be rotated slightly along its vertical axis to change the superfluorescence ring diameter in order to overlap with the white light seed.

The delay between the seed and the green pump can be set to zero by adjusting the delay line stage, as shown in Fig. 4.7. While adjusting the delay, one can obtain a bright signal as shown in Figs. 4.10(c) and (d). The idler (in the infrared region) can be easily seen on a screen in front of the amplifier crystal around the zero delay, through an infrared viewer or using a webcam (with IR filter removed) while adjusting the delay. The idler beam appears on the left side of the ring and on the left side of the pump spot. The signal is the

amplification of the seed, appearing on the right side of the ring, along the seed. While moving the delay line stage, once the idler is appeared, one can fix the delay line stage at that position. We only need to move it slightly around that delay position to detect the signal which might appear weak at first. At this point the spatial overlap of the white light seed and the pump can be checked at the crystal. The focal volume of the seed pulse should overlap with the focal volume of the pump. Also, it should be ensured that the seed and the pump remain spatially overlapped inside the crystal even while the delay stage position is changed. Also, the pump power can be increased carefully for a brief time, while looking for the signal. Once the signal is obtained, it can be maximized by adjusting the wavelength tuning translation stage. Also, it is important to have the lenses which are used to focus the pump and seed beams on a XYZ lens mount. This will allow one to finely adjust the spatial overlap between the seed and the pump and also move the focal point of the white light. A poor overlap between the seed and pump pulse can give rise to a signal with structures as shown in Fig. 4.10(b). One can observe that the superfluorescence ring has completely disappeared, as shown in Fig. 4.10(d), when the green or red amplified signal pulse is generated. When the angle between the seed and the pump, and the crystal angle are slightly adjusted, all the colors in the superfluorescence disappear and the output signal pulse spectrum broadens (Fig. 4.10(d)).

4.4 Results and discussion

NOPA stands for the most widely used devices for obtaining few-cycle tunable pulses [93-100]. In this work, we investigated the use of an Yb:KGW laser at 1028 nm as laser source for NOPA that allows the full coverage from visible to near IR spectral range. We focused on a NOPA pumped by the second harmonic of the fundamental Yb:KGW laser pulses. This allows to extend the tuning spectral range considerably to shorter wavelengths.

4.4.1 Broadband optical parametric amplification

In the process of optical parametric amplification, the pump wavelength limits the shortest achievable amplification wavelength for a given nonlinear crystal. As the amplified signal spectrum gets close to the pump wavelength, idler wavelengths become long in IR range and can be absorbed by the crystal. In our study, due to idler absorption above 3.1 µm, signal amplification at wavelengths below 620 nm ceases in BBO.

Fig. 4.11 depicts the output spectra of the two-stage NOPA which covers a broad amplified wavelength range from 620 nm to beyond 950 nm. This amplified range matches the theoretical calculation as shown in Fig. 2.17. Spectral range of over 200 nm width can be easily amplified. This provides

sufficient bandwidth for pulses with a transform limit duration around 10 fs.
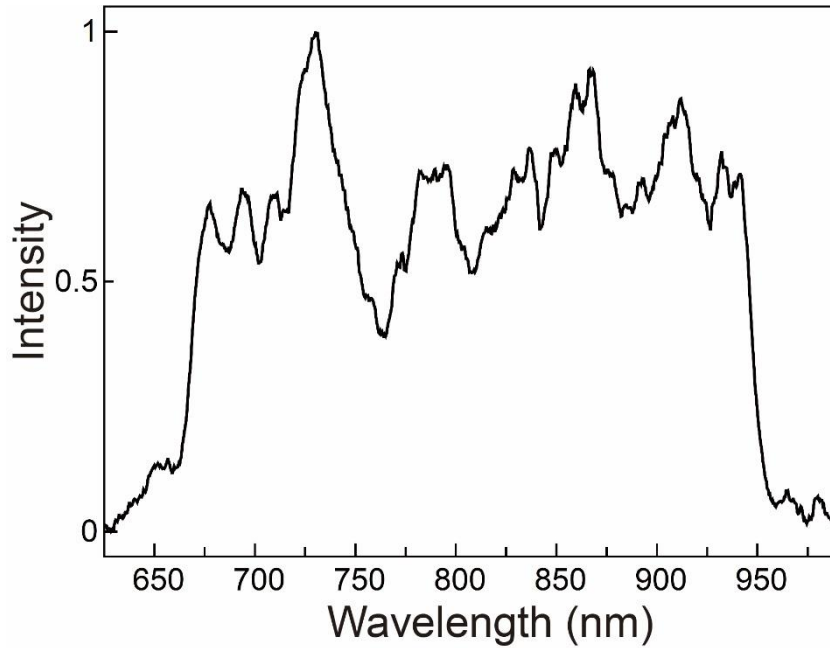
Figure 4.11: Amplified spectrum of the two-stage NOPA pumped by 514 nm beam.
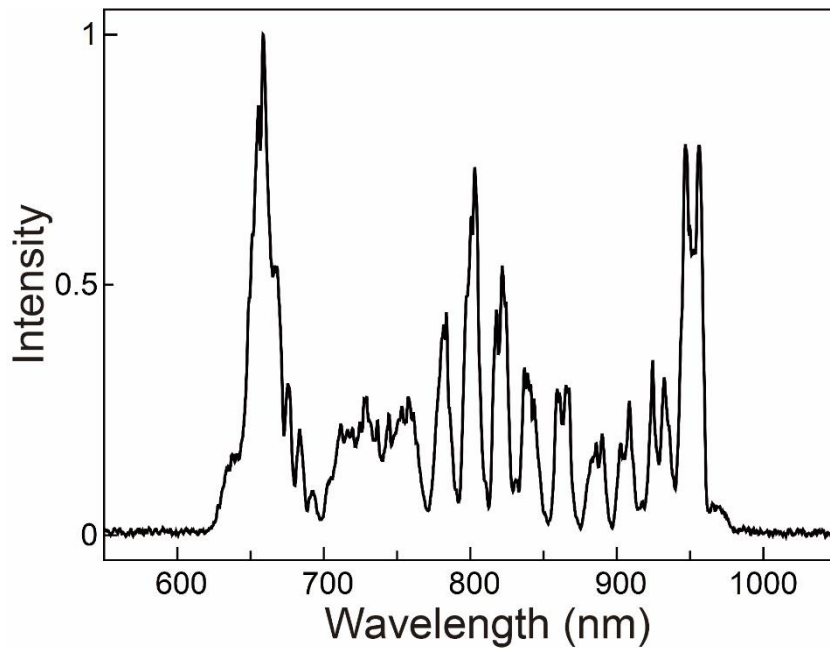
Figure 4.12: When the NOPA is seeded by multi-filaments SC, the NOPA output presents interference structures.

The seed quality is important for obtaining good NOPA output. For example, when high intensity of driving beam is used to generated SC seed, this strong beam produces multi-filaments of SC which finally interfere and form constructive/destructive structures. Thusly the NOPA output also shows

interference structures (see Fig. 4.12). To avoid this unwanted process of multiple filaments emerging from the focus, it is best to adjust the power of our 1028 nm driving beam and focus it on the far surface of the YAG crystal (see Fig. 3.13)

Fig. 4.13 shows typical output spectra of NOPA setup. It is convenient to realize tuning by slightly modifying the phase matching angle and non-collinearity for optical parametric amplification, and by delaying the green (514 nm) pump pulse with respect to the longer (and chirped) seed pulse. The produced outputs can be tuned continuously over visible to near IR regions. Throughout all the tuning spectral range, the spectral curves are rather smooth.
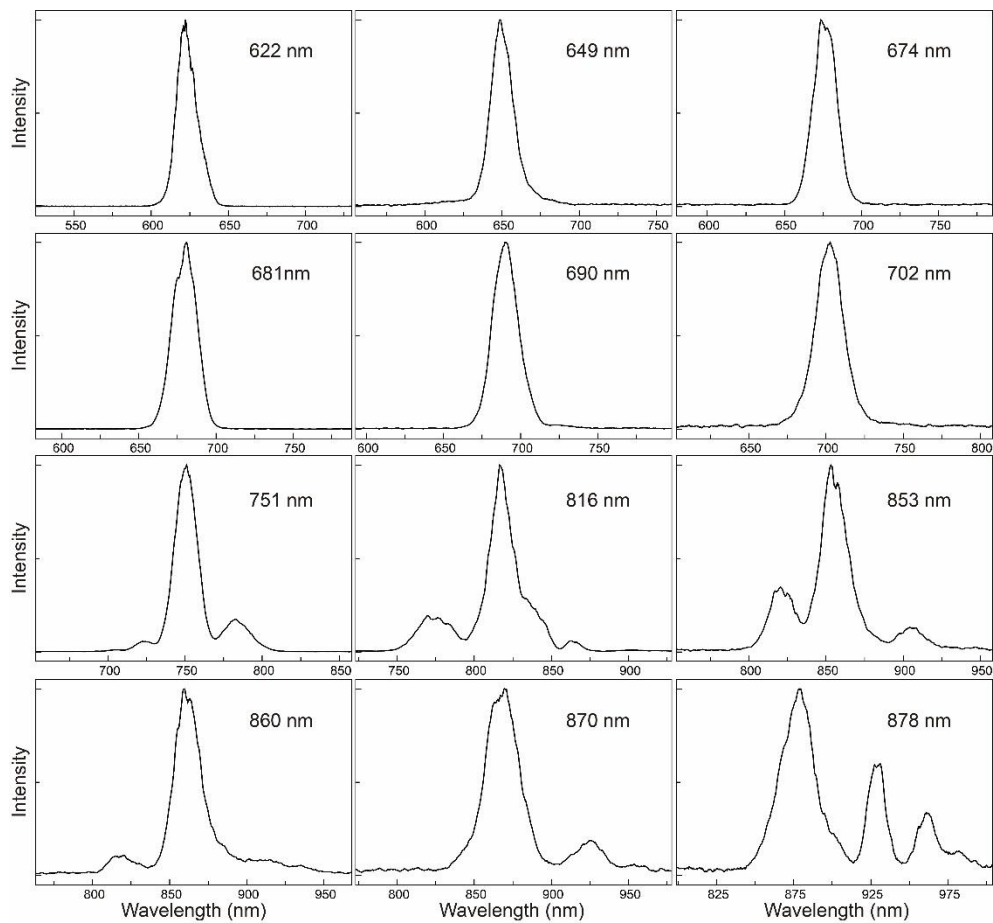
Figure 4.13: Tunable spectra of NOPA outputs. Using the two-stage NOPA, we can obtain tunable outputs covering a broad spectral range from visible to near IR.

4.4.2 Pulse compression using AOPDF

In this experiment, the commercial AOPDF named Dazzler has been used to compress the NOPA output yielding around 16 fs pulses in the 640-840 nm spectral range. Fig. 4.14 shows the spectrum after the Dazzler. Fig. 4.15 shows the second harmonic intensity autocorrelation obtained with the help of a commercial autocorrelator (pulseCheck, APE, Berlin). The pulse duration is

around 16 fs assuming a Gaussian pulse profile. Comparing Figs. 4.11 and 4.14, the optical yield of the Dazzler is commonly 60% in the whole spectral range.
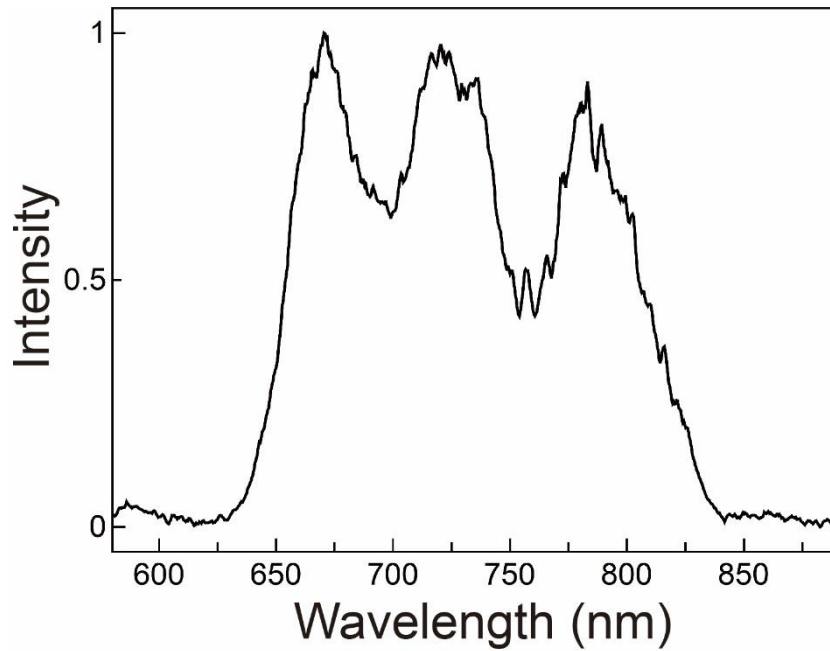
Figure 4.14: The spectrum of the NOPA output diffracted by Dazzler. Because of the spectral restrictions of the Dazzler, only a part of the spectral bandwidth of NOPA output can be shaped by Dazzler.
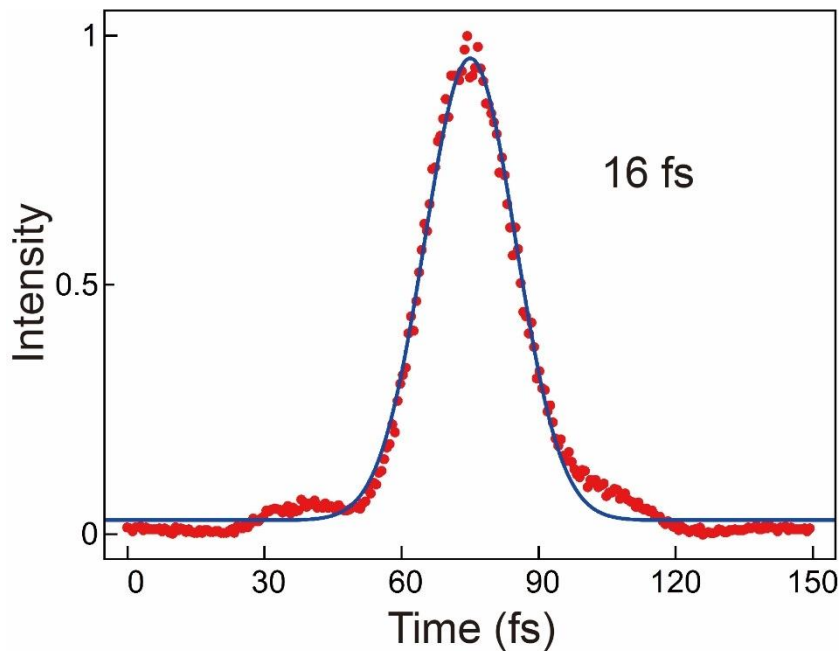
Figure 4.15: The autocorrelation curve of the NOPA output pulse compressed by Dazzler. The red dots and the solid blue line denote the experimental measured data and the Gaussian fitting curve, respectively.

The pulse compression of NOPA output by Dazzler is not ideally completed since the broad bandwidth introduces complicate high dispersion orders. The pulse can not be well compensated by a linear acoustic chirp and it is necessary to use nonlinear chirp signals. In this work, we tried to use nonlinear 2nd and 3rd orders acoustic signals. However, the final compressed signal (Fig. 4.15) still shows slightly low pre- and post-pulses. There is still some residual uncompensated higher order dispersion.

4.5 Summary

Summarizing, in this chapter, we introduce principles of AOPDF and demonstrate the two-stage NOPA pumped with the second harmonic pulses of the ultrafast Yb-based laser system. In the first amplification stage, the supercontinuum generated in a 4 mm YAG plate is used as a seed. The SC contains a wide spectral range, which can be parametrically amplified. The seed beam after the first amplification stage is used as an intense signal for the second amplification stage in the NOPA. The output wavelength range of the two-stage NOPA is tunable between 620 and 950 nm by varying the phase matching conditions or controlling the time overlap between the chirped signal and the pump pulses. The pulse compression of NOPA output is achieved using the AOPDF. By optimizing pulse compression using different dispersion orders, we obtained a ~16 fs ultrashort pulse.

Chapter 5

Summary and outlook

Supercontinuum (SC) generation represents a versatile and unique source of coherent radiation and has become one of the hottest topics in optical and photonic sciences. This dissertation provides a novel method to generate negatively chirped SC by so called ghost pulse. Using the presented method, we succeeded in generating negatively chirped SC in the optical range of normal GVD of used materials.

The SC generation in bulk media is mostly due to the self-phase modulation (SPM) effect which produces the light at new red-shifted and blue-shifted frequencies on the leading and trailing fronts of the driving pulse respectively. It means that the newly generated light features positive chirp. It could be theoretically good explained and modeled using a Gaussian-shaped pumping pulse. We proposed and developed the idea of negatively chirped SC generation due to application as the pump pulse the one with a Gaussian-like hole. In the dissertation we call such kind of pulse a ghost pulse because it has a hole, or negative intensity, in the working time-interval of the SC generation.

To generate the ghost pulse we use the following procedure. A part of the short-pulse radiation is directed into a 4f-line pulse shaping system to produce picosecond long pulse, which cannot generate SC itself due to its low peak power. Then the long pulse is combined with the short pulse or its second harmonic in a type I BBO crystal to realize sum frequency generation (SFG) process. Due to strong energy depletion of the long pulse in the range of overlapping with the short one we create the intensity hole and, as result, our ghost pulse.

In our case the beam of linearly polarized pulses of duration ~200 fs at 1028 nm with 2 kHz repetition rate is divided into two fractions by a beam splitter. One beam after the 4f-line pulse shaping system, which is built using a folded optical geometry, consists of 1-3 ps long pulses. Further, due to SFG in a 2 mm BBO crystal we create the ghost pulse with the 50-70% depletion intensity hole of about 150-300 fs duration. The formation of the ghost pulse was verified by a home-built frequency-resolved optical gating (FROG) setup and a commercial autocorrelator.

The chirp of the generated SC is characterized by a home-built XFROG setup. The experimental results reveal that the SC can be generated by ghost pulse and it differs from the SC generated by short Gaussian pulse. The SC generated by a short pulse is positively chirped, so that the red-shifted frequencies appear earlier than the blue-shifted frequencies like it should be according to the SPM effect. The SC from the ghost pulse is generated in 1

mm sapphire and 4 mm YAG crystals. The SC shows clear negative chirp, which is stronger in sapphire crystal. It is explained by lower GVD coefficient of this crystal in comparison with YAG.

We tested the effect of negatively chirped seed on the duration of output pulses in non-collinear optical parametric amplifier (NOPA). Such NOPA technique is also a good approach to test the negatively chirped SC generated by ghost pulse.

When NOPA is seeded with the SC, generated by the ghost pulse, we manage to get very short output pulses of about 40 fs of the NOPA without pulse compression. In case of seeding the NOPA with the SC generated by the 200 fs at 1028 nm laser pulse, the duration of NOPA output pulse was about 180 fs.

This is a clear demonstration of negatively chirped seed generated by the ghost pulse. Because of positive GVD in all optical elements and crystals in visible and near infrared, we get some compression of the negatively chirped seed and, as result, very short NOPA's pulses.

Moreover, we built a two-stage NOPA. Its output wavelength could be tuned between 620 and 950 nm. We use an acousto-optic programmable dispersive filter (AOPDF) to compress the output pulse. We managed to obtain in this case an ultrashort pulse of about 16 fs duration. Our study shows the improvement of ultra-short pulse generation in a two-stage NOPA and very good spectral tunability of our NOPA based on Yb laser source.

Our experiments inspire future studies in distinct fields. First, this work presents a unique way to generate a negatively chirped SC, which is of importance in the fields of broadband spectral laser sources for ultrafast spectroscopy, optical imaging etc. Future experiments could be focused on systematical investigation of the ghost-pulse shaping to control parameters of the negatively chirped SC. It could help to get perfect compression of the seed due to positive GVD in optical elements and generate ultra-short NOPA-pulses. It is worth to develop the ghost-pulse technique for the laser sources with relatively long pulses, that cannot generate SC by themselves. Introducing very short ghost pulses using laser pulses at other wavelengths in these long pulses, we could generate SC in the spectral range of the long pulses, e.g, IR or UV.

Literature

1. J. Hecht: *Beam: The Race to Make the Laser*. Oxford University Press (2005).

2. M. Csele: *Fundamentals of Light Sources and Lasers*. Wiley (2004).

3. M. Bertolotti: *The History of the Laser*. Institute of Physics (1999).

4. O. Svelto: *Principles of Lasers (4th ed.)*. Springer (1998).

5. A. M. Weiner: *Ultrafast Optics*. Hoboken, NJ: Wiley (2009).

6. J. C. Diels and W. Rudolph: *Ultrashort Laser Pulse phenomena*. New York, Academic (2006).

7. R. Paschotta: *Encyclopedia of Laser Physics and Technology-ultrashort pulses, femtosecond, laser*. www.rp-photonics.com.

8. A. Baltuska, T. Fuji and T. Kobayashi: *Visible pulse compression to 4 fs by optical parametric amplification and programmable dispersion control*. Opt. Lett. **27**, 306-308 (2002).

9. A. Shirakawa, I. Sakane, M. Takasaka and T. Kobayashi: *Sub-5-fs visible pulse generation by pulse-front-matched noncollinear optical parametric amplification*. Appl. Phys. Lett., **74**, 2268-2270 (1999).

10. M. Liebel, C. Schnedermann and P. Kukura: *Sub-10-fs pulses tunable from 480 to 980 nm from a NOPA pumped by an Yb:KGW source*. Opt. Lett. **39**, 4112-4115 (2014).

11. R. Boyd: *Nonlinear Optics (3rd ed.)*. Academic Press (2008).

12. P. Franken, A. Hill, C. Peters and G. Weinreich: *Generation of Optical Harmonics*. Phys. Rev. Lett., **7**, 118-119 (1961).

13. R. C. Eckardt and J. F. Reintjes: *Phase Matching Limitations of High Efficiency Second Harmonic Generation*. IEEE J. Quantum Electron., **20**, 1178-1187 (1984).

14. J. A. Giordmaine and R. C. Miller: *Tunable coherent parametric oscillation in $LiNO_3$ at optical frequencies*. Phys. Rev. Lett. **14**, 973-

976 (1965).

15.   R. A. Baumgartner and R. Byer: *Optical parametric amplification.* IEEE J. Quantum Electron. **15**, 432-444 (1979).

16.   D. Brida, et al.: *Few-optical cycle pulses tunable from the visible to the mid-infrared by optical parametric amplifiers.* J. Opt. **12**, 013001 (2010).

17.   A. Dubietis and A. Couairon: *Ultrafast Supercontinuum Generation in Transparent Solid-State Media.* Springer (2019).

18.   R. R. Alfano: *The Supercontinuum Laser Source: Fundamentals with Updated References.* Springer (2006).

19.   A. Dubietis, et al.: *Ultrafast supercontinuum generation in bulk condensed media.* Lith. J. Phys. **57**, 113 (2017).

20.   R. R. Alfano and S. L. Shapiro: *Emission in the region 4000 to 7000 Å via four-photon coupling in glass.* Phys. Rev. Lett. **24**, 584-587 (1970).

21.   R. R. Alfano and S. L. Shapiro: *Observation of self-phase modulation and small-scale filaments in crystals and glasses.* Phys. Rev. Lett. **24**, 592-594 (1970).

22.   R. R. Alfano, J. Gersten, G. Zawadzkas and N. Tzoar: *Self-phase-modulation near the electronic resonances of a crystal.* Phys. Rev. A **10**, 698-708 (1974).

23.   R. R. Alfano, P. Ho, P. Fleury and H. Guggeneheim: *Nonlinear optical effects in antiferromagnetic $KNiF_3$.* Opt. Commun. **19**, 261-264 (1976).

24.   R. R. Alfano, et al.: *Induced spectral broadening of a weak picosecond pulse in glass produced by an intense picosecond pulse.* Opt. Lett. **11**, 626-628 (1986).

25.   R. R. Alfano, et al.: *Induced spectral broadening about a second harmonic generated by an intense primary ultrashort laser pulse in ZnSe.* Phys. Rev. A **35**, 459-462 (1987).

26.   R. R. Alfano, et al.: *Harmonic cross-phasemodulation in ZnSe.* App. Phys. Lett, **54**, 111-113 (1989).

27.   W. Yu, R. R. Alfano, C. L. Sam and R. J. Seymour: *Spectral broadening of picosecond 1.06 μ pulse in KBr.* Opt. Commun. **14**, 344-347 (1975).

28. W. Werncke, et al.: *An anomalous frequency broadening in water.* Opt. Commun. **4**, 413-415 (1972).

29. A. Penzkofer, A. Laubereau and W. Kaiser: *Stimulated Short-Wave Radiation due to Single-Frequency Resonances of $\chi^{(3)}$.* Phys. Rev. Lett. **31**, 863-866 (1973).

30. W. L. Smith, P. Liu and N. Bloembergen: *Superbroadening in H_2O and D_2O by self-focused picosecond pulses from a YAlG: Nd laser.* Phys. Rev. A **15**, 2396-2403 (1977).

31. P. B. Corkum, C. Rolland and T. Srinivasan-Rao: *Supercontinuum Generation in Gases.* Phys. Rev. Lett. **57**, 2268-2271 (1986).

32. J. H. Glownia, J. Misewich and P. P. Sorokin: *Ultrafast ultraviolet pump–probe apparatus.* J. Opt. Soc. Am. B **3**, 1573-1579 (1986).

33. C. Lin and R. H. Stolen: *New nanosecond continuum for excited-state spectroscopy.* Appl. Phys. Lett. **28**, 216-218 (1976).

34. P. L. Baldeck and R. R. Alfano: *Intensity effects on the stimulated four photon spectra generated by picosecond pulses in optical fibers.* J. Lightwave Technol. **5**, 1712-1715 (1987).

35. A. H. Zewail: *Femtochemistry: atomic-scale dynamics of the chemical bond.* J. Phys. Chem. A **104**, 5660-5694 (2000).

36. R. L. Fork, C. V. Shank, C. Hirlimann, R. Yen and W. J. Tomlinson: *Femtosecond white-light continuum pulses.* Opt. Lett. **8**, 1-3 (1983).

37. T. Morioka, K. Mori and M. Saruwatari: *More than 100-wavelength-channel picosecond optical pulse generation from single laser source using supercontinuum in optical fibres.* Electron. Lett. **29**, 862-864 (1993).

38. T. Stensitzki, et al.: *Acceleration of a ground-state reaction by selective femtosecond-infrared-laser-pulse excitation.* Nature Chem. **10**, 126-131, (2018).

39. K. Goda, K. K. Tsia and B. Jalali: *Serial time-encoded amplified imaging for real-time observation of fast dynamic phenomena.* Nature **458**, 1145-1149 (2009).

40. D. Wildanger, E. Rittweger, L. Kastrup and S. W. Hell: *STED microscopy with a supercontinuum laser source.* Opt. Express **16**, 9614-9621 (2008).

41. A. Wirth, et al.: *Synthesized light transients.* Science **334**, 195-200 (2011).

42. S. A. Diddams, et al.: *Direct link between microwave and optical frequencies with a 300 THz femtosecond laser comb.* Phys. Rev. Lett. **84**, 5102-5105 (2000).

43. D. J. Jones, et al.: *Carrier-envelope phase control of femtosecond mode-locked lasers and direct optical frequency synthesis.* Science **288**, 635-639 (2000).

44. R. Holzwarth, et al.: *Optical frequency synthesizer for precision spectroscopy.* Phys. Rev. Lett. **85**, 2264-2267 (2000).

45. N. R. Newbury: *Searching for applications with a fine-tooth comb.* Nat. Photonic **5**, 186-188 (2011).

46. S. L. Chin, et al.: *The propagation of powerful femtosecond laser pulses in optical media: physics, applications, and new challenges.* Can. J. Phys. **83**, 863-905 (2005).

47. M. Kolesik, G. Katona, J. V. Moloney and E.M. Wright: *Physical factors limiting the spectral extent and band gap dependence of supercontinuum generation.* Phys. Rev. Lett. **91**, 043905 (2003).

48. L. Berge, et al.: *Ultrashort filaments of light in weakly ionized, optically transparent media.* Rep. Prog. Phys. **70**, 1633-1713 (2007).

49. V. P. Kandidov, S. A. Shlenov and O. G. Kosareva: *Filamentation of high-power femtosecond laser radiation.* Quantum Electron. **39**, 205-228 (2009).

50. M. Bradler, P. Baum and E. Riedle: *Femtosecond continuum generation in bulk laser host materials with sub-μJ pump pulses.* Appl. Phys. B **97**, 561-574 (2009).

51. E. Riedle, et al.: *Generation of 10 to 50 fs pulses tunable through all of the visible and the NIR.* Appl. Phys. B **71**, 457-465 (2000).

52. E. T. J. Nibbering, et al.: *Conical emission from self-guided femtosecond pulses in air.* Opt. Lett. **21**, 62-64 (1996).

53. J. Yang and G. Mu: *Multi-dimensional observation of white-light filaments generated by femtosecond laser pulses in condensed medium.* Opt. Express **15**, 4943-4952 (2007).

54. J. C. Diels and W. Rudolph: *Ultrashort Laser Pulse Phenomena (2nd*

ed.). Academic Press (2006).

55.   G. L. Squires: *Practical Physics (4 ed.).* Cambridge University Press (2001).

56.   E. W. Weisstein: *Fourier Transform-Gaussian.* MathWorld (2013).

57.   F. Träger: *Handbook of Lasers and Optics.* Springer (2007).

58.   R. Paschotta: *Encyclopedia of Laser Physics and Technology-group velocity dispersion.* www.rp-photonics.com (2016).

59.   Y. R. Shen: *The Principles of Nonlinear Optics.* Wiley-Interscience (2002).

60.   P. Franken, A. Hill, C. Peters and G. Weinreich: *Generation of Optical Harmonics.* Phys. Rev. Lett. **7**, 118-119 (1961).

61.   A. Morita: *Theory of Sum Frequency Generation Spectroscopy.* Springer Singapore (2018).

62.   F. Vidal and A. Tadjeddine: *Sum-frequency generation spectroscopy of interfaces.* Rep. Prog. Phys. **68**, 1095-1127 (2005).

63.   A. Weiner: *Ultrafast Optics.* Wiley Series in Pure and Applied Optics (2011).

64.   R. L. Fork, B. I. Greene and C. V. Shank: *Generation of optical pulses shorter than 0.1 psec by colliding pulse mode locking.* Appl. Phys. Lett. **38**, 671-672 (1981).

65.   S. Backus, C. G. Durfee, M. M. Murnane, M. Margaret and H. C. Kapteyn: *High power ultrafast lasers.* Rev. Sci. Instrum. **69**, 1207-1223 (1998).

66.   T. Eidam, et al.: *Femtosecond fiber CPA system emitting 830 W average output power.* Opt. Lett. **35**, 94-96 (2010).

67.   P. Russbueldt, T. Mans, J. Weitenberg, H. D. Hoffmann and R. Poprawe: *Compact diode-pumped 1.1 kW Yb:YAG Innoslab femtosecond amplifier.* Opt. Lett. **35**, 4169–4171 (2010).

68.   C. J. Saraceno, et al.: *275 W average output power from a femtosecond thin disk oscillator operated in a vacuum environment.*

Opt. Express **20**, 23535–23541 (2012).

69. I. A. Walmsley and C. Dorrer: *Characterization of ultrashort electromagnetic pulses.* Adv. Opt. Photon. **1**, 308-437 (2009).

70. J. M. Dudley, I. A. Walmsley and R. Trebino: *Measurement of ultrashort electromagnetic pulses.* J. Opt. Soc. Am. B **25**, MU1-2 (2008).

71. K. Sala, G. Kenney-Wallace and G. Hall: *Cw autocorrelation measurements of picosecond laser pulses.* IEEE J. Quantum Electron. **16**, 990-996 (1980).

72. J. M. Diels, J. J. Fontaine, I. C. McMichael and F. Simoni: *Control and measurement of ultrashort pulse shapes (in amplitude and phase) with femtosecond accuracy.* Appl. Opt. **24**, 1270-1282 (1985).

73. A. Monmayrant, B. Chatel and B. Girard: *Real time quantum state holography using coherent transients.* Opt. Commun. **264**, 256-263 (2006).

74. R. Trebino: *Frequency-Resolved Optical Gating: The Measurement of Ultrashort Laser Pulses.* Springer (2000).

75. D. J. Kane and R. Trebino: *Characterization of arbitrary femtosecond pulses using frequency-resolved optical gating.* IEEE J. Quantum Electron. **29**, 571-579 (1993).

76. D. T. Reid, P. Loza-Alvarez, C. T. A. Brown, T. Beddard and W. Sibbett: *Amplitude and phase measurement of mid-infrared femtosecond pulses by using cross-correlation frequency-resolved optical gating.* Opt. Lett. **25**, 1478-1480 (2000).

77. P. O'Shea, M. Kimmel, X. Gu and R. Trebino: *Highly simplified device for ultrashort-pulse measurement.* Opt. Lett. **26**, 932-934 (2001).

78. D. J. Kane and R. Trebino: *Single-shot measurement of the intensity and phase of an arbitrary ultrashort pulse by using frequency-resolved optical gating.* Opt. Lett. **18**, 823-825 (1993).

79. J. Paye, M. Ramaswamy, J. G. Fujimoto and E. P. Ippen: *Measurement of the amplitude and phase of ultrashort light pulses from spectrally resolved autocorrelation.* Opt. Lett. **18**, 1946-1948

(1993).

80.   J. Dudley, et al.: *Cross-correlation frequency resolved optical gating analysis of broadband continuum generation in photonic crystal fiber: simulations and experiments.* Opt. Express **10**, 1215-1221 (2002).

81.   T. Y. F. Tsang, M. A. Krumbugel, K. W. DeLong, D. N. Fittinghoff and R. Trebino: *Frequencyresolved optical-gating measurements of ultrashort pulses using surface third-harmonic generation.* Opt. Lett. **21**, 1381-1383 (1996).

82.   M. Maier, W. Kaiser and J. A. Giordmaine: *Intense Light Bursts in the Stimulated Raman Effect.* Phys. Rev. Lett. **17**, 1275-1277 (1966).

83.   A. Monmayrant and B. Chatel: *A new phase and amplitude high resolution pulse shaper.* Rev. Sci. Instrum. **75**, 2668-2671 (2004).

84.   K. W. DeLong, R. Trebino, J. Hunter and W. E. White: *Frequency-resolved optical gating with the use of second-harmonic generation.* J. Opt. Soc. Am. B **11**, 2206-2215 (1994).

85.   R. Trebino and D. J. Kane: *Using phase retrieval to measure the intensity and phase of ultrashort pulses: frequency-resolved optical gating.* J. Opt. Soc. Am. A **10**, 1101-1111 (1993).

86.   K. W. DeLong, R. Trebino and D. J. Kane: *Comparison of ultrashort-pulse frequency-resolved-optical-gating traces for three common beam geometries.* J. Opt. Soc. Am. B **11**, 1595-1608 (1994).

87.   G. Taft, et al.: *Ultrashort optical waveform measurements using frequency-resolved optical gating.* Opt. Lett. **20**, 743-745 (1995).

88.   S. Akturk, et al.: *Measuring several-cycle 1.5-m pulses using frequency-resolved optical gating.* Opt. Express **11**, 3461-3466 (2003).

89.   B. A. Richman, M. A. Krumbugel and R. Trebino: *Temporal characterization of mid IR free-electron-laser pulses by frequency-resolved optical gating.* Opt. Lett. **22**, 721-723 (1997).

90.   K. W. DeLong and R. Trebino: *Improved ultrashort pulse-retrieval algorithm for frequency-resolved optical gating.* J. Opt. Soc. Am. A **11**, 2429-2437 (1994).

91. K. W. DeLong, D. N. Fittinghoff, R. Trebino, B. Kohler and K. Wilson: *Pulse retrieval in frequency-resolved optical gating based on the method of generalized projections.* Opt. Lett. **19**, 2152-2154 (1994).

92. D. J. Kane: *Recent progress toward real-time measurement of ultrashort laser pulses.* IEEE J. Quantum Electron. **35**, 421-431 (1999).

93. J. A. Giordmaine and R. C. Miller: *Tunable coherent parametric oscillation in LiNO3 at optical frequencies.* Phys. Rev. Lett. **14**, 973-976 (1965).

94. R. A. Baumgartner and R. Byer: *Optical parametric amplification.* IEEE J. Quantum Electron. **15**, 432-444 (1979).

95. D. Brida, et al.: *Few-optical cycle pulses tunable from the visible to the mid-infrared by optical parametric amplifiers.* J. Opt. **12**, 013001 (2010).

96. D. Strickland and G. Mourou: *Compression of amplified chirped optical pulses.* Opt. Commun. **56**, 219-221 (1985).

97. A. Dubietis, G. Jonušauskas and A. Piskarskas: *Powerful femtosecond pulse generation by chirped and stretched pulse parametric amplification in {BBO} crystal.* Opt. Commun. **88**, 437-440 (1992).

98. H. Fattahi, et al.: *Third-generation femtosecond technology.* Optica **1**, 45-63 (2014).

99. S. Witte and K. S. E. Eikema: *Ultrafast optical parametric chirped-pulse amplification.* IEEE J. Sel. Top. Quantum Electron. **18**, 296-307 (2012).

100. D. Herrmann, et al.: *Generation of sub-three cycle, 16 TW light pulses by using noncollinear optical parametric chirped-pulse amplification.* Opt. Lett. **34**, 2459-2461 (2009).

101. C. Manzoni and G. Cerullo: *Design criteria for ultrafast optical parametric amplifiers.* J. Opt. **18**, 103501 (2016).

102. P. Weinberger: *John Kerr and his Effects Found in 1877 and 1878.* Philos. Mag. Lett. **88**, 897-907 (2008).

103.   M. Melnichuk and L. T. Wood: *Direct Kerr electro-optic effect in noncentrosymmetric materials.* Phys. Rev. A. **82**, 013821. (2010).

104.   J. H. Marburger: *Self-focusing: theory.* Prog. Quantum Electron. **4**, 35-110 (1975).

105.   R. Y. Chiao, E. Garmire and C. H. Townes: *Self-trapping of optical beams.* Phys. Rev. Lett. **13**, 479-482 (1964).

106.   M. A. Porras, A. Parola, D. Faccio, A. Couairon and P. Di Trapani: *Light-filament dynamics and the spatiotemporal instability of the townes profile.* Phys. Rev. A **76**, 011803(R) (2007).

107.   E. L. Dawes and J. H. Marburger: *Computer studies in self-focusing.* Phys. Rev. **179**, 862-868 (1969).

108.   M. D. Feit and J. A. Fleck: *Effect of refraction on spot-size dependence of laser-induced breakdown.* Appl. Phys. Lett. **24**, 169-172 (1974).

109.   A. Couairon and A. Mysyrowicz: *Femtosecond filamentation in transparent media.* Phys. Rep. **441**, 47-189 (2007).

110.   A. Braun, et al.: *Self-channeling of high-peak-power femtosecond laser pulses in air.* Opt. Lett. **20**, 73-75 (1995).

111.   E. T. J. Nibbering, et al.: *Conical emission from self-guided femtosecond pulses in air.* Opt. Lett. **2**, 62-64 (1996).

112.   B. La Fontaine, et al.: *Filamentation of ultrashort pulse laser beams resulting from their propagation over long distances in air.* Phys. Plasmas **6**, 1615-1621 (1999).

113.   G. Méchain, et al.: *Long range self-channeling of infrared laser pulses in air: a new propagation regime without ionization.* Appl. Phys. B **79**, 379-382 (2004).

114.   G. Méchain, et al.: *Length of plasma filaments created in air by a multiterawatt femtosecond laser.* Opt. Commun. **247**, 171-180 (2005).

115.   L. Wöste, et al.: *Femtosecond atmospheric lamp.* Laser und Optoelektronik **29**, 51-53 (1997).

116.   M. Rodriguez, et al.: *Kilometric-range nonlinear propagation of femtosecond laser pulses.* Phys. Rev. E **69**, 036607 (2004).

117.   Y. Silberberg: *Collapse of optical pulses.* Opt. Lett. **15**, 1282-1284 (1990).

118.   N. Bloembergen and P. Lallemand: *Complex intensity-dependent index of refraction, frequency broadening of stimulated Raman lines, and stimulated Rayleigh scattering.* Phys. Rev. Lett. **16**, 81-84 (1966).

119.   R. G. Brewer: *Frequency shifts in self-focusing light.* Phys. Rev. Lett. **19**, 8-10 (1967).

120.   A. C. Cheung, D. M. Rank, R. Y. Chiao and C. H. Townes: *Phase modulation of Q-switched laser beams in small-scale filaments.* Phys. Rev. Lett. **20**, 786-789 (1968).

121.   P. Lallemand: *Temperature variation of the width of stimulated Raman lines in liquids.* Appl. Phys. Lett. **8**, 276-277 (1996).

122.   W. J. Jones and B.P. Stoicheff: *Inverse Raman Spectra: Induced absorption at optical frequencies.* Phys. Rev. Lett. **13**, 657-659 (1964).

123.   F. Shimizu: *Frequency broadening in liquids by a short light pulse.* Phys. Rev. Lett. **19**, 1097-1100 (1967).

124.   B. P. Stoicheff: *Characteristics of stimulated Raman radiation generated by coherent light.* Phys. Lett. **7**, 186-188 (1963).

125.   F. DeMartini, C. H. Townes, T. K. Gustafson and P. L. Kelley: *Self-steepening of light pulses.* Phys. Rev. **164**, 312-323 (1967).

126.   J. E. Rothenberg: *Space–time focusing: breakdown of the slowly varying envelope approximation in the self-focusing of femtosecond pulses.* Opt. Lett. **17**, 1340-1342 (1992).

127.   G. Fibich and G. C. Papanicolaou: *Self-focusing in the presence of small time dispersion and nonparaxiality.* Opt. Lett. **22**, 1379-1381 (1997).

128.   J. K. Ranka and A. L. Gaeta: *Breakdown of the slowly varying envelope approximation in the self-focusing of ultrashort pulses.* Opt.

Lett. **23**, 534-536 (1998).

129.   M. Wittmann and A. Penzkofer: *Spectral superbroadening of femtosecond laser pulses.* Opt. Commun. **126**, 308-317 (1996).

130.   C. Nagura, A. Suda, H. Kawano, M. Obara and K. Midorikawa: *Generation and characterization of ultrafast white-light continuum in condensed media.* Appl. Opt. **41**, 3735-3742 (2002).

131.   S. Tzortzakis, D. G. Papazoglou and I. Zergioti: *Long-range filamentary propagation of subpicosecond ultraviolet laser pulses in fused silica.* Opt. Lett. **31**, 796-798 (2006).

132.   A. L. Calendron, H. Çankaya, G. Cirmi and F. X. Kärtner: *White-light generation with sub-ps pulses.* Opt. Express **23**, 13866-13879 (2015).

133.   H. Cankaya, et al.: *40-µJ passively CEP-stable seed source for ytterbium-based high-energy optical waveform synthesizers.* Opt. Express **24**, 25169-25180 (2016).

134.   M. Schulz, et al.: *Yb:YAG Innoslab amplifier: efficient high repetition rate subpicosecond pumping system for optical parametric chirped pulse amplification.* Opt. Lett. **36**, 2456-2458 (2011).

135.   A. Dubietis, et al.: *Axial emission and spectral broadening in self-focusing of femtosecond Bessel beams.* Opt. Express **15**, 4168-4175 (2007).

136.   D. N. Neshev, A. Dreischuh, G. Maleshkov, M. Samoc and Y. S. Kivshar: *Supercontinuum generation with optical vortices.* Opt. Express **18**, 18368-18373 (2010).

137.   G. Maleshkov, D. N. Neshev, E. Petrova and A. Dreischuh: *Filamentation and supercontinuum generation by singular beams in self-focusing nonlinear media.* J. Opt. **13**, 064015 (2011).

138.   A. Jarnac, et al.: *Whole life cycle of femtosecond ultraviolet filaments in water.* Phys. Rev. A **89**, 033809 (2014).

139.   M. Bradler, P. Baum and E. Riedle: *Femtosecond continuum generation in bulk laser host materials with sub-µJ pump pulses.* Appl. Phys. B **97**, 561-574 (2009).

140.   D. Majus, V. Jukna, E. Pileckis, G. Valiulis and A. Dubietis: *Rogue-wave-like statistics in ultrafast white-light continuum generation in sapphire.* Opt. Express **19**, 16317-16323 (2011).

141.   A. A. Zozulya, S. A. Diddams, A. G. Van Engen and T. S. Clement: *Propagation dynamics of intense femtosecond pulses: multiple splittings, Coalescence, and Continuum Generation.* Phys. Rev. Lett. **82**, 1430-1433 (1999).

142.   K. D. Moll and A. L. Gaeta: *Role of dispersion in multiple-collapse dynamics.* Opt. Lett. **29**, 995-997 (2004).

143.   J. Liu, R. Li and Z. Xu: *Few-cycle spatiotemporal soliton wave excited by filamentation of a femtosecond laser pulse in materials with anomalous dispersion.* Phys. Rev. A **74**, 043801 (2006).

144.   Light Conversion, Lithuania, http://www.lightcon.com/Product/PHAROS.html.

145.   P. J. Campagnola, et al.: *Three-dimensional high resolution second-harmonic generation imaging of endogenous structural proteins in biological tissues.* Biophys. J. **81**, 493-508 (2002).

146.   W. R. Zipfel, et al.: *Live tissue intrinsic emission microscopy using multiphoton-excited native fluorescence and second harmonic generation.* PNAS **100**, 7075-7080 (2003).

147.   W. Mohler, A. C. Millard and P. J. Campagnola: *Second harmonic generation imaging of endogenous structural proteins.* Science Direct - Methods **29**, 97-109 (2003).

148.   T. Ehmke, et al.: *Spectral behavior of second harmonic signals from organic and non-organic materials in multiphoton microscopy.* AIP Adv. **5**, 084903 (2015).

149.   J. Zhang, J. Y. Huang, H. Wang, K. S. Wong and G. K. Wong: *Second-harmonic generation from regeneratively amplified femtosecond laser pulses in BBO and LBO crystals.* J. Opt. Soc. Am. B **15**, 200-209 (1998).

150.   J. P. Farrell, et al.: *Influence of phase matching on the cooper minimum in Ar high-order harmonic spectra.* Phys. Rev. A **83**, 023420 (2011).

151.   R. LaComb, O. Nadiarnykh, S. S. Townsend and P. J. Campagnola: *Phase matching considerations in second harmonic generation from tissues: Effects on emission directionality, conversion efficiency and observed morphology*. Opt. Commun. **281**, 1823-1832 (2008).

152.   C Froehly, B. Colombeau and M. Vampouille: *Shaping and analysis of picosecond light pulses*. Progress in Optics (1983).

153.   N. Dudovich, D. Oron and Y. Silberberg: *Quantum control of the angular momentum distribution in multiphoton absorption processes*. Phys. Rev. Lett. **92**, 103003 (2004).

154.   A. Efimov, C. Schaffer and D. H. Reitze: *Programmable shaping of ultrabroad-bandwidth pulses from a Ti:sapphire laser*. J. Opt. Soc. Am. **12**, 1968-1980 (1995).

155.   H. Wang, et al.: *20-fs pulse shaping with a 512-element phase-only liquid crystal modulator*. IEEE J. Sel. Top. Quantum Electron. **7**, 718-727 (2001).

156.   A. Brodeur and S. L. Chin: *Ultrafast white-light continuum generation and self-focusing in transparent condensed media.* J. Opt. Soc. Am. B **16**, 637-650 (1999).

157.   V. P. Kandidov, et al.: *Self-transformation of a powerful femtosecond laser pulse into a white-light laser pulse in bulk optical media (or supercontinuum generation).* Appl. Phys. B: Lasers Opt. **77**, 149-165 (2003).

158.   I. Walmsley, L. Waxer and C. Dorrer: *The role of dispersion in ultrafast optics.* Rev. Sci. Instrum. **72**, 1-29 (2001).

159.   E. B. Treacy: *Optical pulse compression with diffraction gratings.* IEEE J. Quantum Electron. **5**, 454-458 (1969).

160.   O. E. Martinez: *3000 times grating compressor with positive group velocity dispersion: application to fiber compensation in 1.3–1.6 µm region.* IEEE J. Quantum Electron. **23**, 59-64 (1987).

161.   T. Tanigawa, Y. Sakakibara, S. Fang, T. Sekikawa and M. Yamashita: *Spatial light modulator of 648 pixels with liquid crystal transparent from ultraviolet to near-infrared and its chirp compensation application.* Opt. Lett. **34**, 1696-1698 (2009).

162.   D. Zeidler, T. Hornung, D. Proch and M. Motzkus: *Adaptive compression of tunable pulses from a non-collinear-type OPA to below 16 fs by feedback-controlled pulse shaping.* Appl. Phys. B **70**, S125 (2000).

163.   A. Monmayrant and B. Chatel: *A new phase and amplitude high resolution pulse shaper.* Rev. Sci. Instrum. **75**, 2668-2671 (2004).

164.   B. Pearson B and T. C. Weinacht: *Shaped ultrafast laser pulses in the deep ultraviolet.* Opt. Express **17**, 4385-4388 (2007).

165.   H. S. Tan, W. S. Warren and E. Schreiber: *Generation and amplification of ultrashort shaped pulses in the visible by a two-stage noncollinear optical parametric process.* Opt. Lett. **26**, 1812-1814 (2001).

166.   M. Roth, M. Mehendale, A. Bartelt and H. Rabitz: *Acousto-optical shaping of ultraviolet femtosecond pulses.* Appl. Phys. B **80**, 441-444 (2005).

167.   M. A. Dugan, J. X. Tull and W. S. Warren: *High resolution acousto-optic shaping of unamplified and amplified femtosecond laser pulses.* J. Opt. Soc. Am. **14**, 2348-2358 (1997).

168.   S. H. Shim, D. B. Strasfeld, E. C. Fulmer and M. T. Zanni: *Femtosecond pulse shaping directly in the mid IR using acousto-optic modulation.* Opt. Lett. **31**, 838-840 (2006).

169.   E. Zeek, et al.: *Pulse compression by use of deformable mirrors.* Opt. Lett. **24**, 493-495 (1999).

170.   M. Hacker, et al.: *Micromirror SLM for femtosecond pulse shaping in the ultraviolet.* Appl. Phys. B **76**, 711-714 (2003).

171.   A. Rondi, J. Extermann, L. Bonacina, S. Weber and J. P. Wolf: *Characterization of a MEMS-based pulse-shaping device in the deep ultraviolet.* Appl. Phys. B **96**, 757-761 (2009).

172.   J. C. Vaughan, T. Hornung, T. Feurer and K. A. Nelson: *Diffraction-based femtosecond pulse shaping with a two-dimensional spatial light modulator.* Opt. Lett. **30**, 323-325 (2005).

173.   E. Frumker and Y. Silberberg: *Phase and amplitude pulse shaping with two-dimensional phase-only spatial light modulators.* J. Opt.

Soc. Am. B **24**, 2940-2947 (2007).

174.   P. Tournois: *Acousto-optic programmable dispersive filter for adaptive compensation of group delay time dispersion in laser systems.* Opt. Commun. **140**, 245-249 (1997).

175.   F. Verluise, V. Laude, Z. Cheng, C. Spielmann and P. Tournois: *Amplitude and phase control of ultrashort pulses by use of an acousto-optic programmable dispersive filter: pulse compression and shaping.* Opt. Lett. **25**, 575-577 (2000).

176.   M. Pittman, et al.: *Design and characterization of a near-diffraction-limited femtosecond 100-TW 10-Hz high-intensity laser system.* Appl. Phys. B **74**, 529-535 (2002).

177.   A. Monmayrant, et al.: *Time-domain interferometry for direct electric-field reconstruction by use of an acousto-optic programmable filter and a two-photon detector.* Opt. Lett. **28**, 278-280 (2003).

178.   B. Chatel, J. Degert, S. Stock and B. Girard: *Competition between sequential and direct paths in a two-photon transition.* Phys. Rev. A **68**, 041402R (2003).

179.   Fastlite, France, https://www.fastlite.com/produits/dazzler/.

180.   A. Monmayrant, S. Weberand and B. Chatel: *A newcomer's guide to ultrashort pulse shaping and characterization.* J. Phys. B: At. Mol. Opt. Phys. **43**, 103001 (2010).

181.   S. K. Karthick Kumar, T. Goswami, I. Bhattacharyya and D. Goswami: *Visible 20-femtosecond pulse generation by double-pass non-collinear optical parametric amplifier.* Curr. Sci. **96**, 1496-1500 (2009).

Acknowledgements

At this point, I want to emphasize that my past five years studying in Germany has been an extremely memorable experience and make me grow up in more ways than one.

Here, I want to thank all the people who helped me in Germany. All of them supported me to overcome many difficulties and setbacks. Especially, I want to thank the members of my group for the friendly and team work atmosphere.

I would like to express my deep appreciations to my supervisor Prof. Karsten Heyne for giving me opportunity to work in our group, for his guidance, for his encouragement, and also for the financial support. He acquainted me with the supercontinuum generation and also helped me gain a deep insight into the ultrafast lasers.

I very appreciate my second supervisor Prof. Holger Dau for helpfulness and for sharing his knowledge with me, and for the willingness to evaluate my dissertation.

I would also like to thank my mentor Dr. Valeri for his comprehensive guidance that saw me through these past five years in Free University of Berlin. Without Valeri's warm help and guidance, I would not have been able to complete my experimental research and the final dissertation.

My sincere gratitude also goes to my colleague Frederik for his help about the two photons microscopy and idea about the STED microscopy.

Many thanks go to Till for letting me benefit from his expertise in Python programming.

Finally, I would like to thank my parents for their unconditional support and patience over all these five years. Last but not least, a great deal of credit goes to my wife Yuqing Su and my baby Beiyan who are my life motivation. I definitely do not envision myself here today if it were not for them.

Selbstständigkeitserklärung

Name: Zhang
Vorname: Xingwen

Ich erkläre gegenüber der Freien Universität Berlin, dass ich die vorliegende Dissertation selbstständig und ohne Benutzung anderer als der angegebenen Quellen und Hilfsmittel angefertigt habe. Die vorliegende Arbeit ist frei von Plagiaten. Alle Ausführungen, die wörtlich oder inhaltlich aus anderen Schriften entnommen sind, habe ich als solche kenntlich gemacht. Diese Dissertation wurde in gleicher oder ähnlicher Form noch in keinem früheren Promotionsverfahren eingereicht.

Mit einer Prüfung meiner Arbeit durch ein Plagiatsprüfungsprogramm erkläre ich mich einverstanden.

Datum: den 26. 01. 2021   Unterschrift: Xingwen Zhang

Declaration of authorship

Name: Zhang
First name: Xingwen

I declare to the Freie Universität Berlin that I have completed the submitted dissertation independently and without the use of sources and aids other than those indicated. The present thesis is free of plagiarism. I have marked as such all statements that are taken literally or in content from other writings. This dissertation has not been submitted in the same or similar form in any previous doctoral procedure.

I agree to have my thesis examined by a plagiarism examination software.

Date: January 26, 2021   Signature: Xingwen Zhang